AWARD NUMBER: W81XWH-14-1-0228

TITLE: Biomechanical Modeling and Measurement of Blast Injury and Hearing Protection Mechanisms

PRINCIPAL INVESTIGATOR: Rong Gan, Ph.D.

CONTRACTING ORGANIZATION: University of Oklahoma
Norman

REPORT DATE: October 2015

TYPE OF REPORT: Annual

PREPARED FOR: U.S. Army Medical Research and Materiel Command
Fort Detrick, Maryland 21702-5012

DISTRIBUTION STATEMENT: Approved for Public Release;
Distribution Unlimited

REPORT DOCUMENTATION PAGE

Form Approved
OMB No. 0704-0188

1. REPORT DATE
October 2015

2. REPORT TYPE
Annual

3. DATES COVERED
30 Sep 2014 – 29 Sep 2015

4. TITLE AND SUBTITLE
Biomechanical Modeling and Measurement of Blast Injury and Hearing Protection Mechanisms

5a. CONTRACT NUMBER

5b. GRANT NUMBER
W81XWH-14-1-0228

5c. PROGRAM ELEMENT NUMBER

6. AUTHOR(S)
Rong Gan, Ph.D.

E-Mail: rgan@ou.edu

5d. PROJECT NUMBER

5e. TASK NUMBER

5f. WORK UNIT NUMBER

7. PERFORMING ORGANIZATION NAME(S) AND ADDRESS(ES)
University of Oklahoma, Norman, Oklahoma, 73019

8. PERFORMING ORGANIZATION REPORT NUMBER

9. SPONSORING / MONITORING AGENCY NAME(S) AND ADDRESS(ES)

U.S. Army Medical Research and Materiel Command
Fort Detrick, Maryland 21702-5012

10. SPONSOR/MONITOR'S ACRONYM(S)

11. SPONSOR/MONITOR'S REPORT NUMBER(S)

12. DISTRIBUTION / AVAILABILITY STATEMENT

Approved for Public Release; Distribution Unlimited

13. SUPPLEMENTARY NOTES

14. ABSTRACT
Objectives of the project are to determine middle ear protective mechanisms and develop the finite element (FE) model of the human ear for simulating blast injury and assisting design/evaluation of HPDs. There are three aims: quantify middle ear injury in relation to overpressure level and wave direction using cadaver ears; identify middle ear protection mechanisms by detecting middle ear muscle reflex in animals and measuring mechanical properties of ear tissues after exposure; develop FE model of human ear to predict middle ear responses to blast and prevention mechanisms of acoustic injury for HPDs. Major findings include: 1) overpressure waveforms recorded at the ear canal entrance, near the eardrum, and inside middle ear with the eardrum rupture thresholds; 2) EMG measurements of stapedius muscle of chinchillas in response to blast exposure; 3) mechanical properties of human and chinchilla ear tissues (eardrum, incus-stapes joint) pre- and post-blast exposure; 4) 3D FE modeling of blast overpressure transduction from the ear canal to middle ear and the eardrum movement. Results demonstrate biomechanical responses of the ear and changes of its structure and function following blast exposure. Our understanding of blast wave transmission through the ear has been improved significantly through this research project.

15. SUBJECT TERMS
Blast overpressure transmission, ear biomechanics, tympanic membrane perforation, middle ear muscle reflex, finite element modeling of human ear

16. SECURITY CLASSIFICATION OF:			17. LIMITATION OF ABSTRACT	18. NUMBER OF PAGES	19a. NAME OF RESPONSIBLE PERSON
a. REPORT	**b. ABSTRACT**	**c. THIS PAGE**			USAMRMC
Unclassified	Unclassified	Unclassified	Unclassified	107	**19b. TELEPHONE NUMBER** *(include area code)*

Table of Contents

Page

1. INTRODUCTION

The objectives of this research project are to determine middle ear protective mechanisms in the conductive path of impulse noise/blast into cochlea and to develop the finite element model of the human ear for simulating blast injury and assisting the design and evaluation of personal hearing protection devices (HPDs). To our knowledge this state-of-the-art approach has not been experimentally applied to evaluating the mechanical basis for middle and inner ear damage relevant to high intensity sound/blast exposure. Our **long-term goal** is to understand middle ear biomechanics in response to high intensity sound and impulse noise and to provide the prevention mechanism of acoustic injury for development of effective personal HPDs. To reach the objectives and long-term goal, we have a series of tasks under three specific aims to test our **general hypothesis**: the biomechanical response of the middle ear and inner ear (or cochlea) to impulse noise or blast exposure can be characterized in our 3D comprehensive finite element model of the human ear.

2. KEYWORDS

Blast overpressure transmission, ear biomechanics, tympanic membrane perforation, middle ear muscle reflex, finite element modeling of human ear

3. ACCOMPLISHMENTS

- **What were the major goals of the project?**

The project has three specific aims with 7 tasks over 4 years of funding period.
Aim 1: To quantify middle ear injury in relation to blast overpressure level and impulse wave direction using human cadaver ears or temporal bones (Years 1-3).
Task 1-1. To identify blast-induced damage of the eardrum and middle ear ossicles when the ear is exposed to different blast overpressure levels at several incident wave directions (Year 1).
Task 1-2. To characterize the transfer functions of the ear canal and middle ear in response to impulse sound or blast overpressure applied at the ear canal entrance (Years 1-3).

Aim 2: To identify middle ear protection mechanisms using the chinchilla model and the dynamic properties of ear tissues (Years 1-4).
Task 2-1. To detect the middle ear muscle reflex in awake chinchillas during the blast exposure (Years 1-3).
Task 2-2. To identify changes of mechanical properties of middle ear tissues after high impulse noise/blast exposure in human temporal bones (Years 1-4).

Aim 3: To continue the development of our 3-dimensional (3D) finite element (FE) model of the human ear with militarily relevant applications (Years 1-4).
Task 3-1. To improve the current 3D FE model of the human ear by including middle ear nonlinearities (Years 1-3).

Task 3-2. To develop the active FE model of the ear associated with middle ear muscle functions (Years 2-4).
Task 3-3. To provide prevention mechanisms of acoustic injury for personal hearing protection devices (HPDs, passive and active) by using our 3D FE model of the human ear (Years 3-4).

● **What was accomplished under these goals?**

(1) In the first year of the project, the major activities under Aim 1 include: 1) developing the "head block" with the cadaver ear or temporal bone attached to measure blast pressure transmission from the ear canal into the middle ear and cochlea; 2) conducting blast tests at two incident wave directions: from the top of the head - the vertical setup and from lateral to the ear – horizontal setup inside the blast test chamber and monitoring the blast pressure at the entrance of the ear canal (P0), near the tympanic membrane (TM) in the ear canal (P1), and behind the TM in the middle ear cavity (P2); 3) conducting blast tests to determine the threshold of TM perforation or rupture, which is defined as the maximum P0 peak pressure before the TM is damaged; 4) performing multiple blast tests at the pressure level below the TM rupture threshold. The specific objectives are to investigate overpressure wave transduction from the environment through the ear canal into the middle ear and measure the TM rupture threshold in vertical and horizontal setups to blast exposures in cadaver ears or temporal bones.

Figure 1A shows the experimental setup with a cadaver ear or temporal bone in vertical direction inside the blast test camber and Fig. 1B displays the experimental setup with a cadaver ear or temporal bone in horizontal direction inside the blast test camber. The P0 sensor was placed at the ear canal entrance and two other pressure sensors were inserted near the TM in the canal (P1), and behind the TM in the middle ear (P2) as shown in the schematic of Fig. 2A. Figure 2B displays the recorded typical waveforms by three sensors.

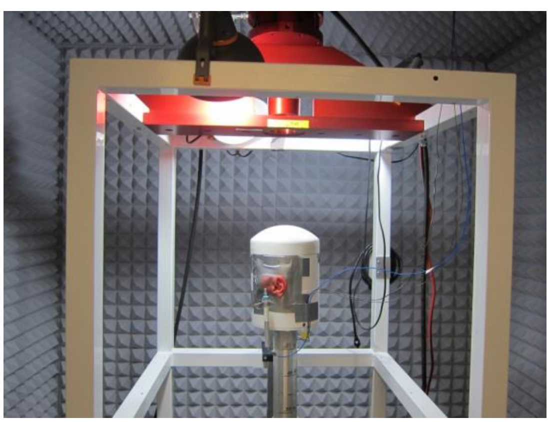

Fig. 1A. Vertical setup of experiment with a cadaver ear nside the blast chamber.

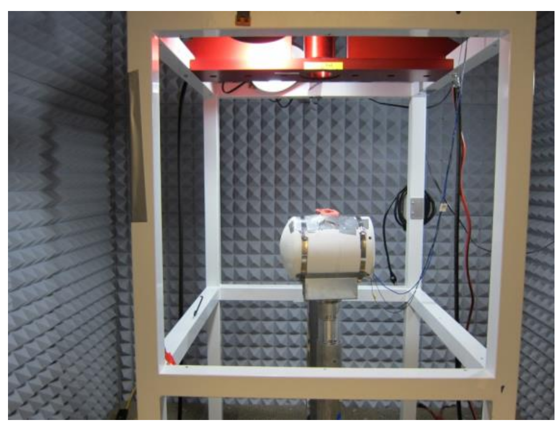

(B) Horizontal setup of experiment with a cadaver ear inside the blast chamber.

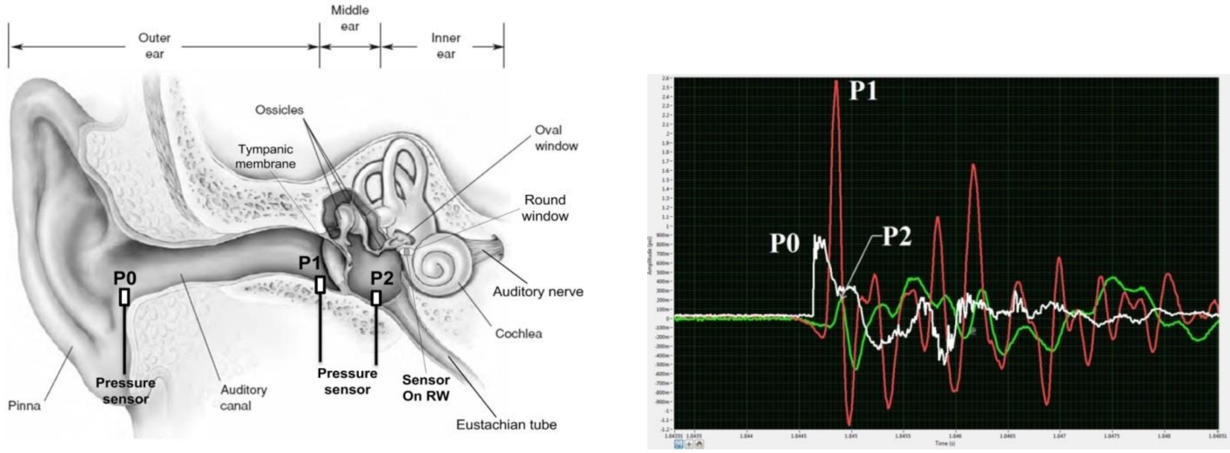

(A) (B)

Fig. 2A. Schematic of simultaneously measuring blast overpressure transduction through the ear with 3 pressure transducers. (B) Recorded typical P0, P1, and P2 waveforms from a cadaver ear.

Figure 3A shows the overpressure waveforms of P0 (black line), P1 (red), and P2 (green) recorded from a cadaver ear during vertical testing. The impulse signals are within 1 ms. Positive overpressure is followed by negative pressure. Figure 3B displays the pressure waveforms recorded from another cadaver ear in vertical test. Figures 4A and 4B show the overpressure waveforms of P0, P1, and P2 recorded from two cadaver ears during horizontal testing. There is no significant difference of waveforms between these two incident wave directions. P1 is much greater than P0 and P2 is the smallest in both vertical and horizontal tests.

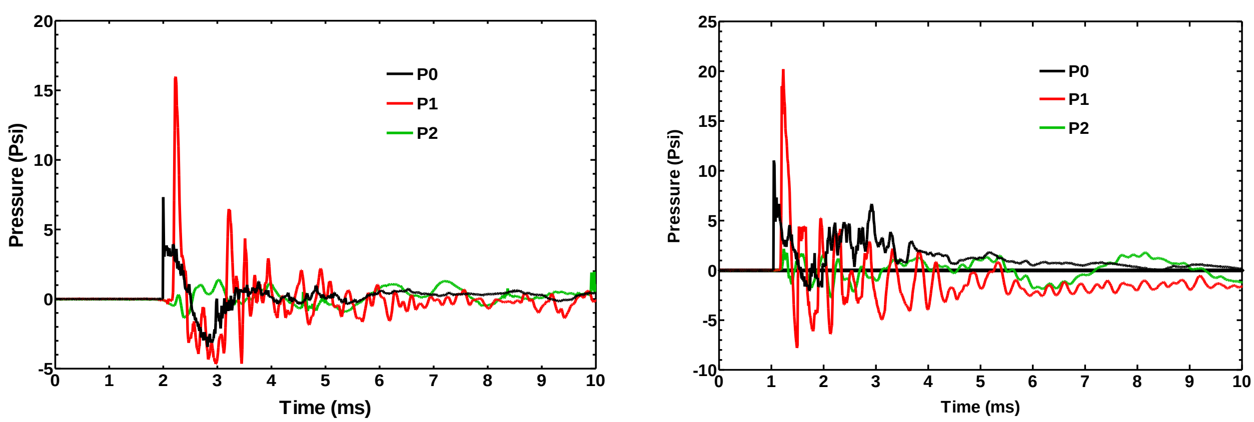

Fig. 3A. Waveforms recorded from a cadaver ear during vertical test inside the blast chamber.

(B) Waveforms recorded from another cadaver ear during vertical test inside the blast chamber.

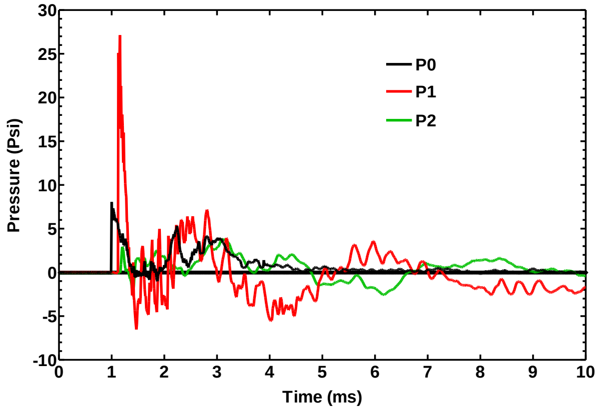

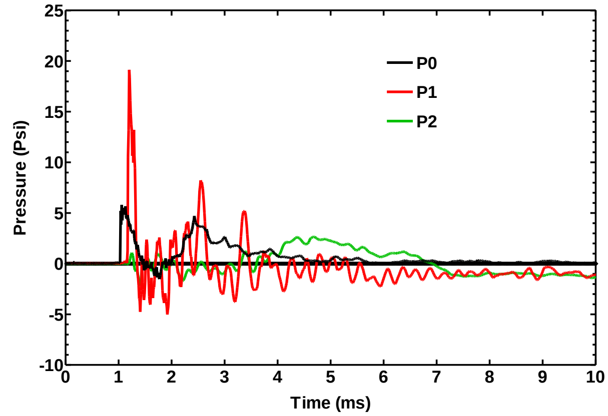

Fig. 4A. Waveforms recorded from a cadaver ear during horizontal test inside the blast chamber.

(B) Waveforms recorded from another cadaver ear during horizontal test inside the blast chamber.

We have adopted the signal energy calculation method for impulse energy spectra analysis in the time domain as **Impulse Energy Flux** (energy per unit area) in unit J/m^2. Octave band filters were designed to calculate the signal energy in 10 frequency bands from the below 125 Hz to over 16 kHz. Figure 5A displays the normalized energy flux distribution over 10 octave bands in vertical test from one ear and Fig. 5B shows the normalized energy flux over 10 octave bands in horizontal test from one ear. Note that data in the figures were normalized w.r.t. P0, P1, and P2 total signal energy, respectively. As can be seen in these two figures, the energy flux values of P0, P1, and P2 in vertical test are all at frequencies of 500 Hz – 8 kHz, particularly for P1; while in horizontal test, the energy flux of P0, P1, and P2 are all at frequencies below 2 kHz.

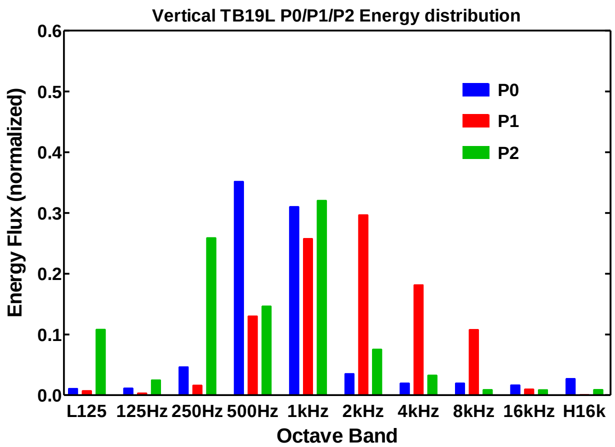

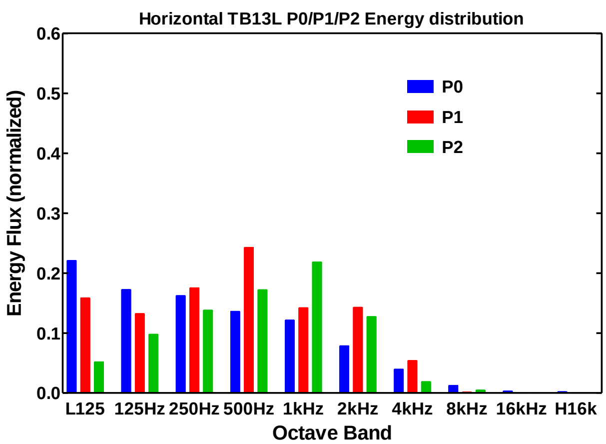

Fig. 5A.Distribution of normalized energy flux over 10 octave bands during vertical test of one cadaver ear.

(B) Distribution of normalized energy flux over 10 octave bands during horizontal test of one cadaver ear.

Figure 6 shows the TM rupture patterns obtained from two temporal bones in vertical tests. There is no consistent TM damage pattern from the tests we conducted. However, the damage severity is usually related to blast overpressure level. Table 1 lists the recorded peak pressure values of P0, P1, and P2 from 13 cadaver ears or temporal bones with the thresholds from vertical tests. The mean threshold is 9.2 psi from 13 temporal bones tested in vertical setup. The ratio of P1/P0 and the ratio of P2/P0 are also listed in the table with a mean value of 2.2 and 0.3, respectively.

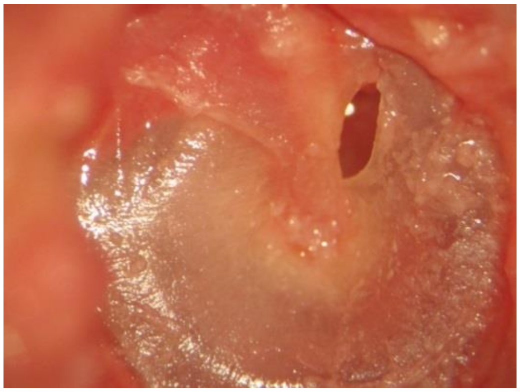

Fig. 6A. Sample TB 14-19L, left ear, TM ruptured in superior-posterior region.

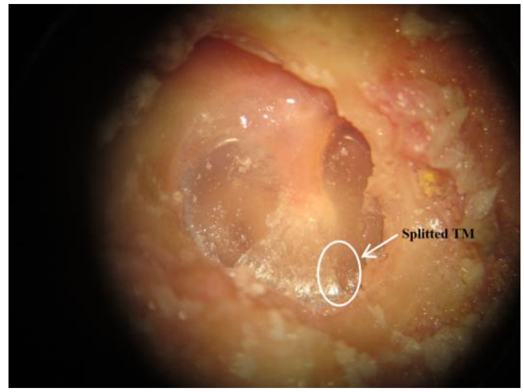

(B) Sample 15-4R, left ear, TM ruptured in inferior side.

Table 1. Vertical setup testing results of peak pressure values P0, P1, P2, and the TM rupture threshold of P0.

TB Sample	P0 (psi)	P1 (psi)	P2 (psi)	P1/P0	P2/P0	Threshold P0 (psi)
14-19L	**7.5**	**14.6**	**0.42**	**1.95**	**0.06**	**8.5**
14-23L	**7.9**	**11.4**	**1.64**	**1.44**	**0.21**	**8.0**
14-24R	**7.1**	**17.4**	**0.8**	**2.45**	**0.11**	**8.0**
15-2R	**10**	**18.8**	**6.7**	**1.88**	**0.67**	**10.0**
15-3L	**9.4**	**20.4**	**4.1**	**2.17**	**0.43**	**9.4**
15-4R	**8.4**	**17.4**	**1.2**	**2.07**	**0.14**	**9.0**
15-5L	**10**	**21.5**	**1.3**	**2.15**	**0.13**	**10.0**
15-6R	**11**	**20**	**2.2**	**1.82**	**0.2**	**11.0**
15-11L	**8.6**	**19**	**2.0**	**2.21**	**0.23**	**9.0**
15-12R	**6.6**	**23.3**	**3.3**	**3.53**	**0.5**	**6.6**
15-13L	**9.8**	**23.3**	**2.5**	**2.38**	**0.26**	**10.0**
15-14R	**6.8**	**21.2**	**2.6**	**3.12**	**0.38**	**6.8**
15-15L	**13.1**	**22.4**	**1.2**	**1.71**	**0.09**	**13.0**
Mean ± SD (N=13)	**8.9±1.8**	**19.3±3.3**	**2.3±1.6**	**2.2±0.5**	**0.3±0.2**	**9.2±1.7**

Figure 7 shows the TM rupture patterns obtained from two temporal bones samples in horizontal tests. Similarly, there is no consistent TM damage pattern from the tests we conducted. However, the damage severity is usually related to blast overpressure level. Table 2 lists the recorded peak pressure values of P0, P1, and P2 from 14 cadaver ears or temporal bones with the thresholds from horizontal tests. The mean threshold is 6.7 psi from 9 temporal bones tested in horizontal setup. The ratio of P1/P0 and the ratio of P2/P0 are also listed in the table with a mean value of 3.04 and 0.37, respectively.

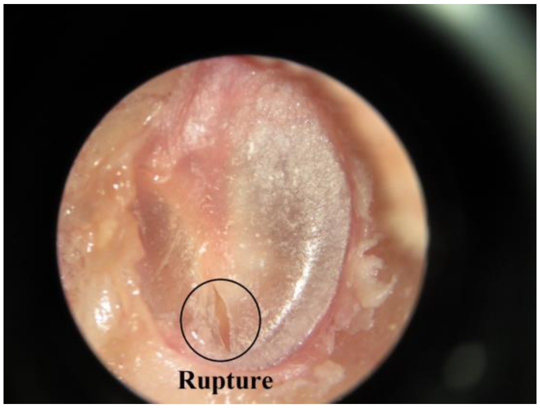

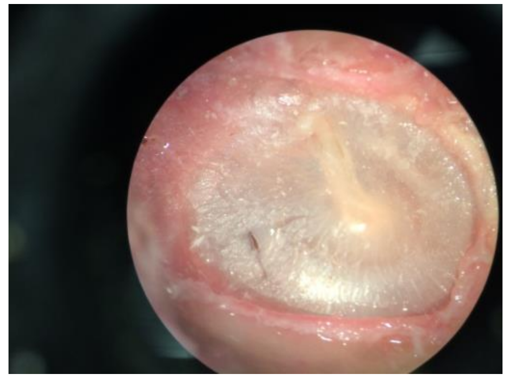

Fig. 7A. Sample TB15-25L, left ear, TM ruptured in inferior side. (B) Sample TB15-34R, right ear, TM ruptured in posterior side.

Table 2. Horizontal setup testing results of peak pressure values P0, P1, P2, and the TM rupture threshold of P0.

TB Sample	P0 (psi)	P1 (psi)	P2 (psi)	P1/P0	P2/P0	Threshold P0 (psi)
14-15L	9.0	14.3	1.8	1.58	0.20	9.0
14-17L	12.0	27.5	1.5	2.29	0.13	N/A
15-10R	5.8	17.1	0.7	2.95	0.12	N/A
15-21L	5.8	19.0	1.0	3.28	0.17	5.8
15-22R	5.8	17.5	2.0	3.02	0.34	5.8
15-25L	5.8	17.5	2.0	3.02	0.34	5.8
15-26R	5.2	13.7	6.4	2.63	1.23	5.2
15-28R	8.0	27.0	3.0	3.38	0.38	8.0
15-29L	3.93	15.45	1.0	3.93	0.25	N/A
15-30R	3.75	10.55	0.8	2.81	0.20	N/A
15-31L	6.2	29.0	3.5	4.68	0.56	6.2
15-32R	4.15	10.28	2.6	2.48	0.62	N/A
15-33L	7.2	21.1	1.5	2.93	0.21	7.2
15-34R	7.4	26.5	3.0	3.58	0.41	7.4
Mean ± SD (N=14)	6.4±2.1	19.03±6.07	2.2±1.4	3.04±0.72	0.37±0.28	6.7±1.2

Comparison of the results obtained from the vertical tests with those from the horizontal tests suggests that the mean ratio of P1 to P0 in horizontal setup is higher than that in vertical setup. In other words, the increase of peak impulse pressure through the ear canal in horizontal direction or the blast wave coming from lateral to the ear, is more severe than the vertical or blast wave from the top of the head. This conclusion is consistent with the lower TM rupture threshold measured from horizontal than the threshold from vertical test.

(2) The major activities under Aim 2 for Task 2-1 include: 1) developing surgical procedure to access the stapedius muscle, place the electrodes into the muscle, and design the animal holder used in the blast testing chamber; 2) verifying the study protocol for electromyography (EMG) measurement of the stapedius muscle reflex in response to acoustic stimulus and blast exposure; 3) conducting EMG measurements on chinchillas to determine the threshold and latency of the stapedius or middle ear muscle reflex (MEMR); 4) performing experiments on chinchillas to measure the TM rupture threshold under the open and shielded conditions. The specific objectives are to develop animal experimental protocols, prepare tools and surgical procedures for EMG measurement, complete the EMG measurement of MEMR induced by acoustic stimulation and blast overpressure, and investigate the TM damage threshold in chinchillas.

Figure 8A shows a view of the stapedius muscle through the surgical opening and Fig. 8B displays the animal holder inside the test chamber with the animal. The animal holder is secured in protection of wires/cables connections to limit the effect of noise or mechanical vibration on EMG signal. We successfully completed 7 animals on the EMG measurement of stapedius muscle induced by acoustic stimulation over frequencies at 1, 2, 4, and 6 kHz. The results were presented at the 2015 ARO Annual meeting in Baltimore. The acoustic response study has confirmed that the electrode was placed in the muscle and EMG signals were correct. Then, the EMG measurements were conducted in 11 animals when animals were exposed to blast. Figure 9 shows the waveforms recorded from the electrode inserted in the stapedius muscle of one animal under two different blast pressure levels. Figure 10 gives the comparison of EMG signals induced by blast with a peak pressure of 185 dB and that by acoustic stimulation of 100 dB at 4 kHz.

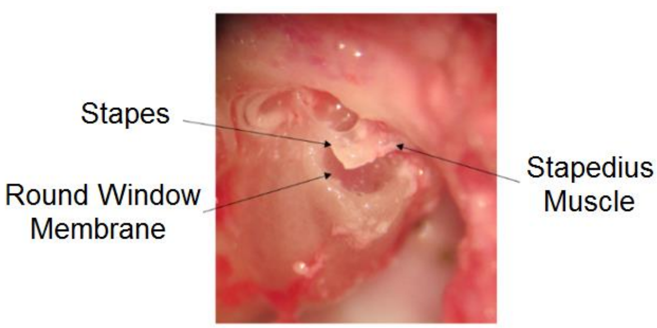

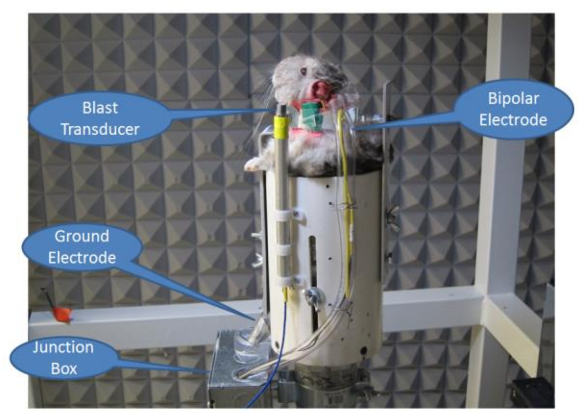

Fig. 8A. View of the stapedius muscle through the surgical opening in posterior part of the bulla, just above the midline.

(B) A picture of the animal holder with the chinchilla sited inside the blast testing chamber (left view).

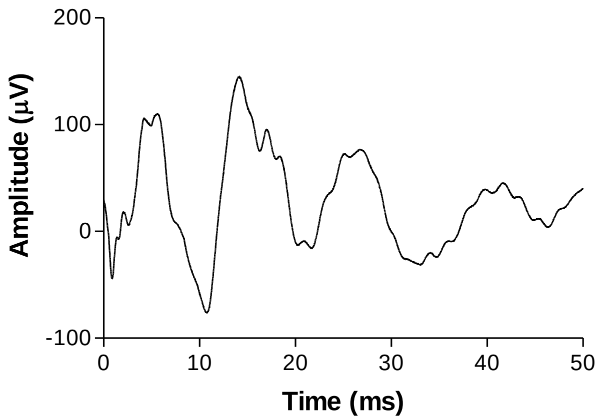

Fig. 9A. EMG signal recorded from chinchilla15-3-9 at the blast pressure level of 2.5 psi.

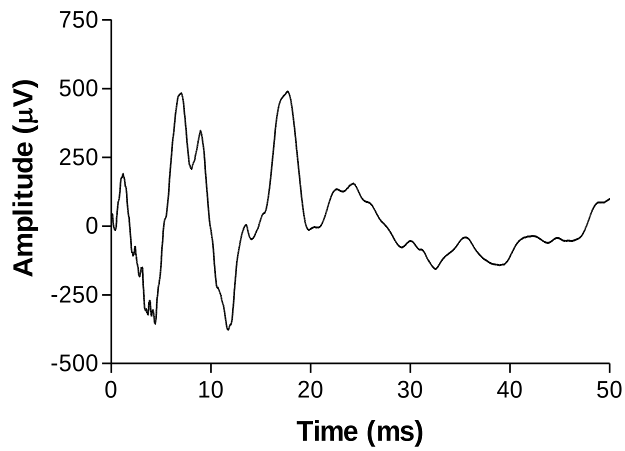

(B) EMG signal recorded from the same animal (chinchilla 15-3-9) at the blast pressure level of 8.3 psi.

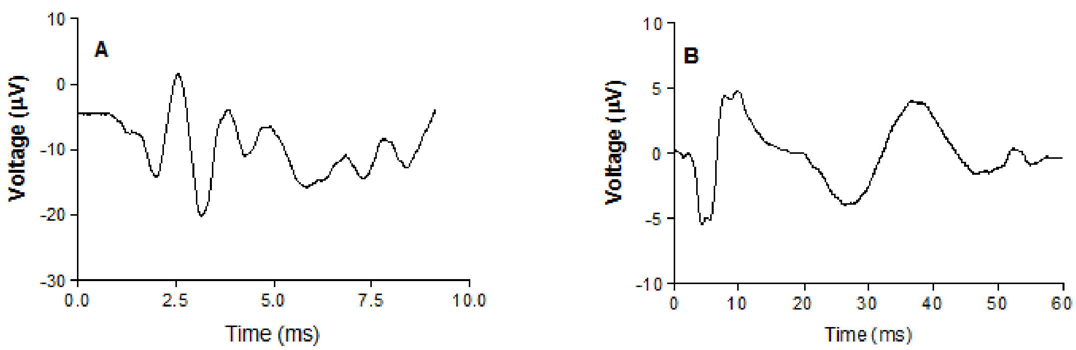

Fig. 10. Comparison of the EMG signals of MEMR recorded from blast exposure (A) and acoustic stimulation at 4 kHz (B).

As shown in Fig. 10, the muscle response to blast was doubled in amplitude with a much short duration (10 ms vs. 50 ms).

Chinchilla TM rupture threshold was measured under two conditions: open field and shielded with a helmet covering the animal head. The preliminary results show that waveforms recorded in shielded case were different from that in open field and the TM rupture threshold in shielded case was lower than that in open field (3.4 vs. 9.1 psi or 181 vs. 190 dB SPL). To understand the mechanisms behind the experiment observation, we did finite element analysis. The results were presented in the 7th International Symposium on Middle Ear Mechanics in Research and Otology (MEMRO). The manuscript of this study was submitted to Hearing Research and is currently under review (see Appendices).

(3) The major activity under Aim 2 for Task 2-2 is to develop the protocol and perform dynamic test of incus-stapes joint (ISJ) with the dynamic mechanical analyzer (DMA, ElectroForce 3200,

Bose) to determine complex modulus of ISJ over the frequency range 1-80 Hz. Then, the frequency-temperature superposition (FTS) principle is applied on DMA measured data to shift the frequency range to a much higher level such as 10 kHz. The specific objectives are to determine dynamic properties of human ear tissues such as the ISJ, TM, and round window membrane before and after blast exposure.

The DMA test of ISJ sample was conducted at three temperatures: 5°, 25°, and 37°C over frequencies of 1-80 Hz. Figure 11A shows the ISJ specimen mounted in DMA and Fig. 11B displays the typical force and displacement data recorded in DMA. Experiments of 8 ISJ specimens were completed and the results are shown in Fig. 12 as the complex modulus expressed as the storage modulus E' and loss modulus or loss factor E'' over the tested frequency range of 1-80 Hz at three temperatures. Then, using the FTS principle, the shift factor for each sample was calculated based on the data measured from three temperatures. In this study, the complex modulus at different temperatures was shifted to form a smooth master curve at a reference temperature (e.g., the body temperature 37°C) and the complex modulus at the higher frequencies was obtained. Figure 13 displays the master curves of the storage modulus and loss modulus obtained from 8 individual samples as well as the mean curves.

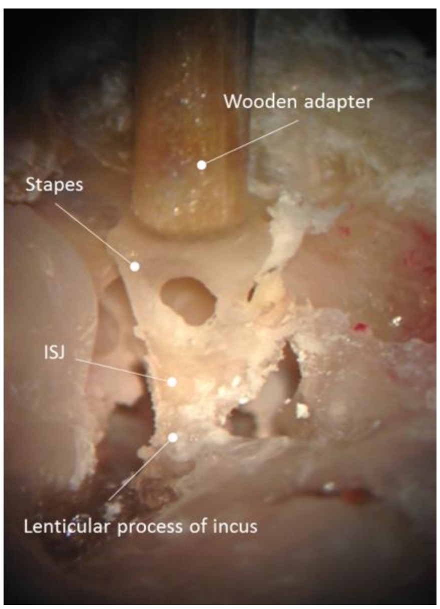

Fig. 11A. Picture of the ISJ sample setup in DMA system.

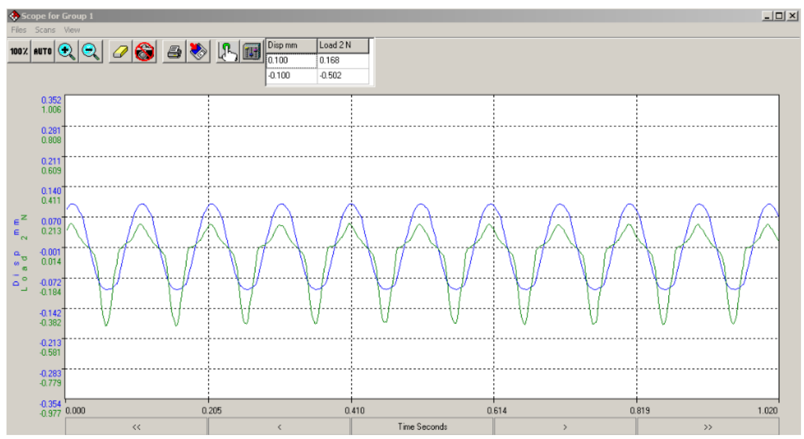

(B) Recorded displacement (blue line) and force (green line) at 10 Hz from TB15-1. The input of ISJ specimen deformation was 0.1 mm in amplitude.

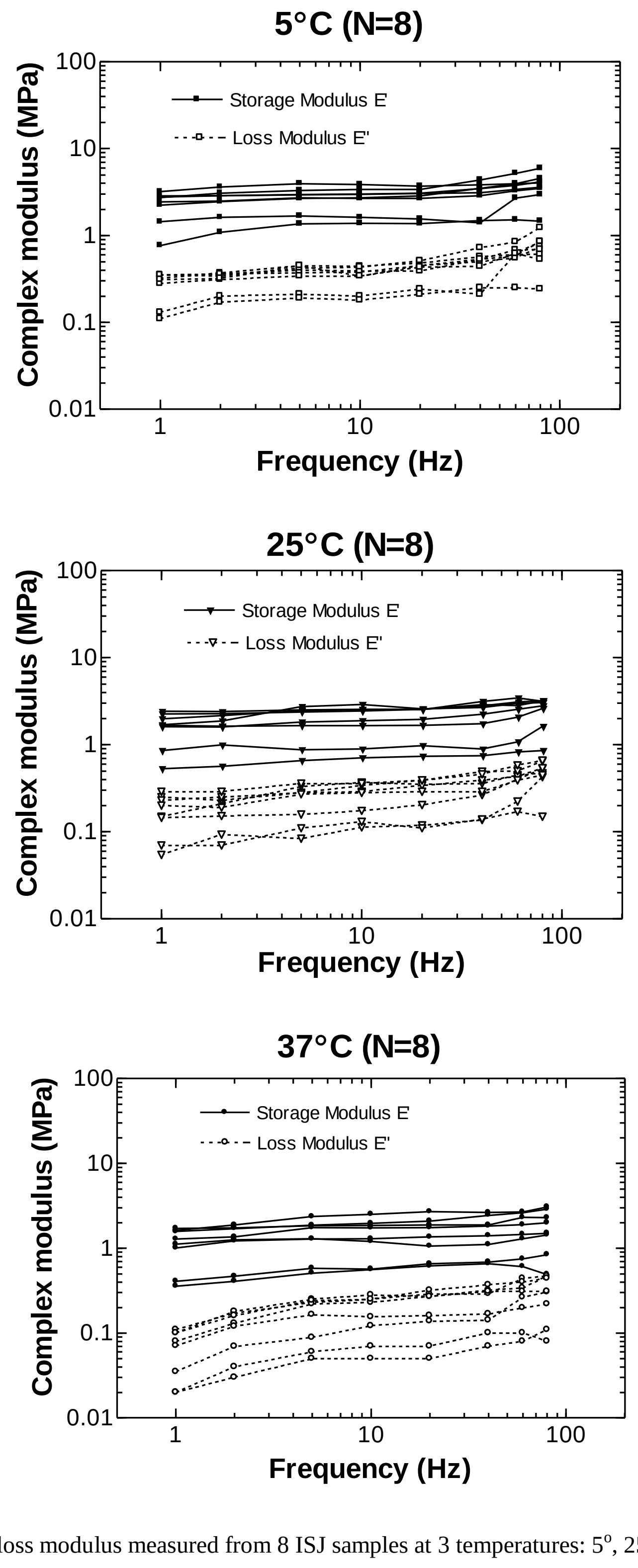

Fig. 12. The storage modulus and loss modulus measured from 8 ISJ samples at 3 temperatures: 5°, 25°, and 37°C.

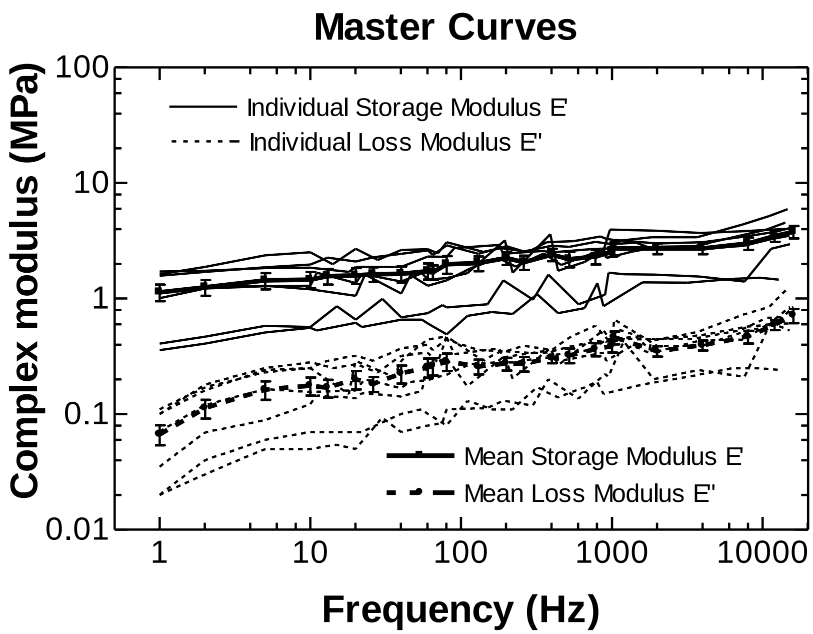

Fig. 13. The master curves of the storage modulus and loss modulus from 8 ISJ samples after using the FTS principle. The individual curves from 8 samples and the mean data with SD bars are displayed in the figure.

(4) The major activities under Aim 2 for Task 2-2 performed at the UT-Dallas (subcontract) include: 1) the micro-fringe projection system was setup to measure the surface topography of TM under a given pressure in Dr. Gan's lab. This apparatus allows the measurement of pressure as a function of volume displacement applied on the TM. 2) A miniature split Hopkinson tension bar (SHTB) system was built and setup in Dr. Gan's lab to measure dynamic properties of human TM after multiple blast exposure. Both studies were conducted in Dr. Gan's lab at the University of Oklahoma by Dr. Lu's group from the UT-Dallas. The specific objectives are to establish reliable protocols, prepare samples, conduct measurements of pre- and post-blast chinchilla and human TM samples, and investigate the failure modes and the change of ultimate strength of post-blast chinchilla TM.

10 healthy chinchilla bullas (control group) were tested using the micro-fringe projection system and the mechanical properties as presented of pressure-volume displacement vs. static pressure applied on the TM were determined. Figure 14 shows the individual pressure-volume displacement curves obtained from 10 chinchilla TM samples. The results measured from micro-fringe projection system and further analysis of TM mechanical properties using hyperelastic Ogden model were submitted to Hearing Research. The manuscript is currently under review and attached to this report in Appendices.

13 chinchilla ears or bullas were exposed to blast for 4 times at a pressure level of 1.5 psi. Bullas were then harvested and tested using the micro-fringe projection system to investigate the effect of blast wave on mechanical properties of the TM. Figure 15 shows the surface profiles obtained from one TM under different static pressure: 0, -0.75 kPa, and 0.88 kPa. Figure 16 shows the pressure as a function of volume displacement plotted in the individual curves for 13 post-exposure chinchilla TMs.

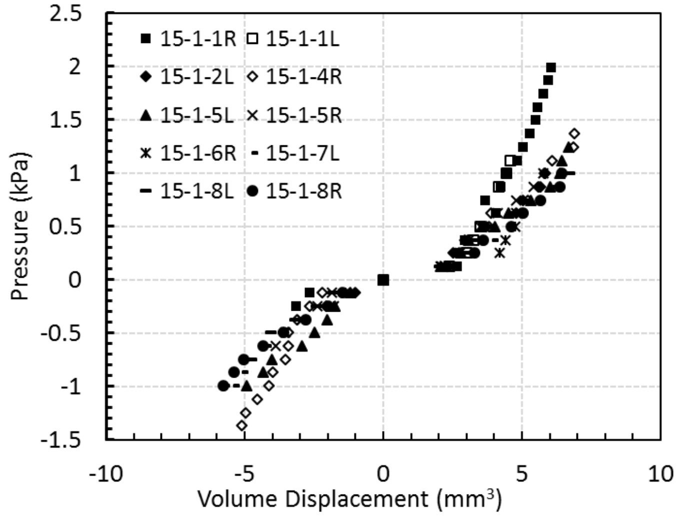

Fig. 14. Measurement results of 10 controlled chinchilla TM from micro-fringe projection system.

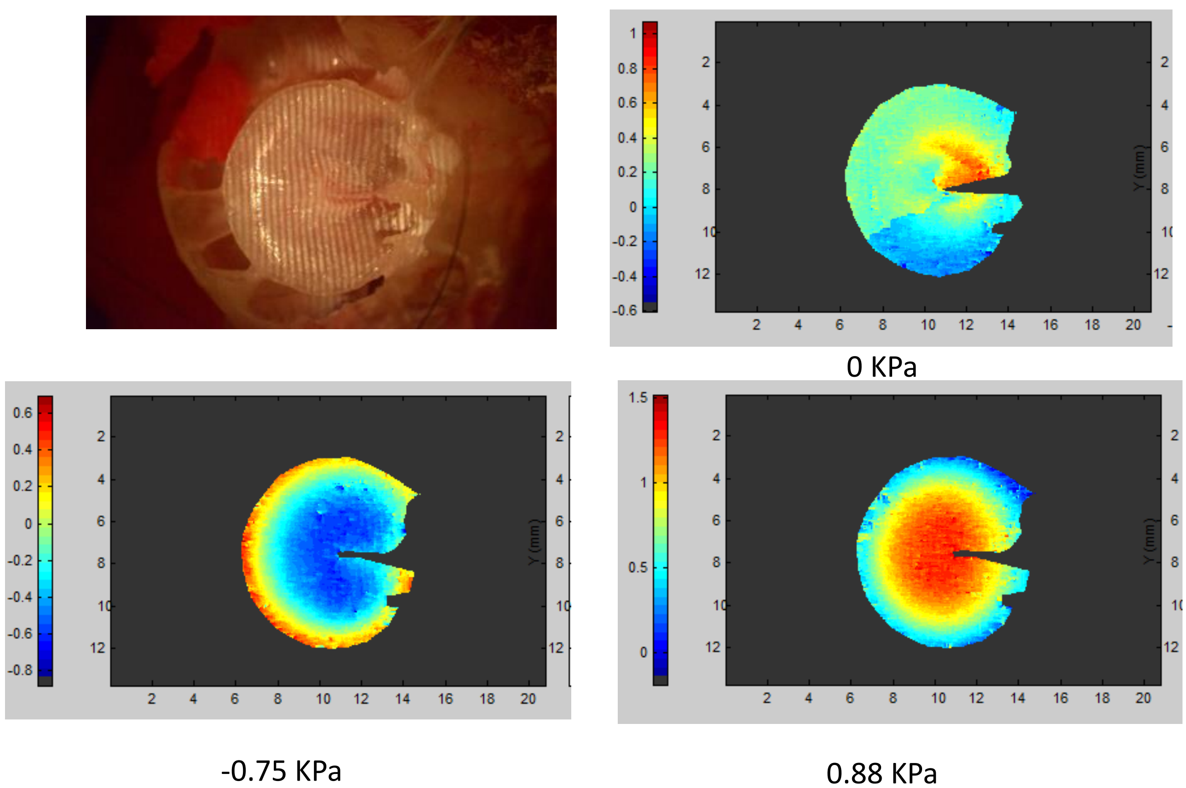

Fig. 15. TM images under micro-projected fringes for surface profilometry. The left-upper panel shows micro-projected fringes on a chinchilla TM and the rest figures show *z*-displacement under zero, -0.75 kPa, and 0.88 kPa pressure.

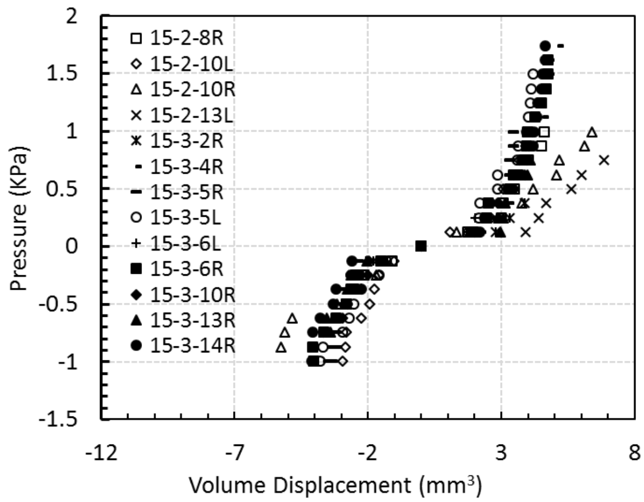

Fig. 16. Measurement results of 13 chinchilla TM after exposure to blast as measured by the micro-fringe projection system.

Comparing the pressure-volume displacement relationships or curves obtained from the pre- and post-blast exposure TMs, an obvious difference was observed as shown in Fig. 17, the mean pressure-volume displacement curves obtained from pre- and post-blast chinchillas. As can be seen in this figure, under positive pressure (pressure applied from ear canal side) the pressure-volume velocity curves are similar in a consistent pattern. However, there are some discrepancies of pressure-volume displacement curves between the pre- and post-blast under negative pressure. We may need further study and analysis to bring the conclusion on the results.

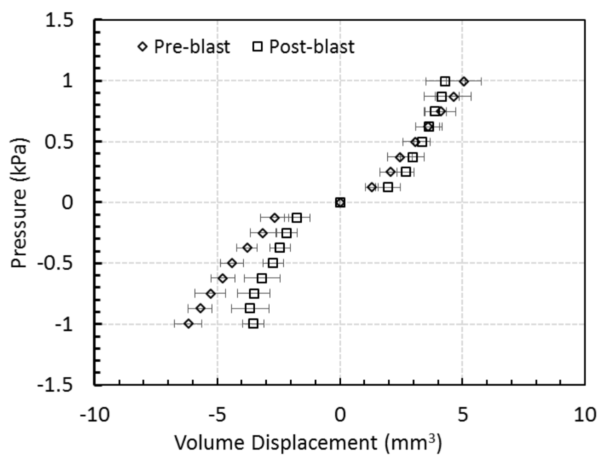

Fig. 17. Comparison of pressure-volume displacement curves obtained from pre- and post-blast chinchilla TMs.

The miniature split Hopkinson tension bar (SHTB) facility was set up in Dr. Gan's lab and used to measure mechanical properties of TMs along the radial and circumferential directions after exposure to blast wave. Figure 18A shows the SHTB setup in lab and Fig. 18B displays the typical TM sample preparation for specimens along the radial/transverse and circumferential directions. Six temporal bones were included in vertical setup test with multiple exposures (x5 times) at the P0 pressure level of 5 psi, the pressure at the ear canal entrance. Six temporal bones served as control or intact TM. After exposure, the TM was harvested from the temporal bone and the TM strips or specimens for SHTB testing were prepared along the radial and circumferential directions as shown in Fig. 18B.

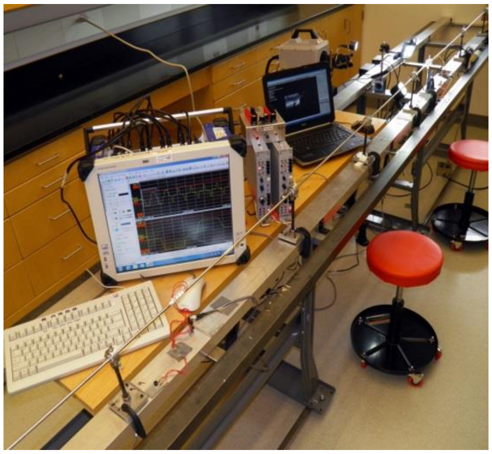

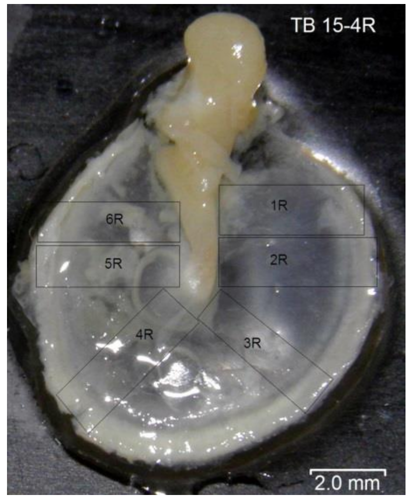

Fig. 18A. A miniature split Hopkinson tension bar setup that includes incident bar, transmission bar, and data acquisition system.

(B) TM strips were cut according to the damaged TM shape either along radial direction (R) or circumferential direction (T).

Figure 19 shows the Young's modulus-high strain rate relationships obtained from the post-blast exposure TM samples and the pre-exposure or intact normal samples along the radial and circumferential directions. The results suggest that TMs after blast wave exposure have higher Young's modulus in radial direction (24.3~96 MPa) and lower modulus in circumferential direction (11.7~78.3 Mpa) compared to the values of normal TMs.

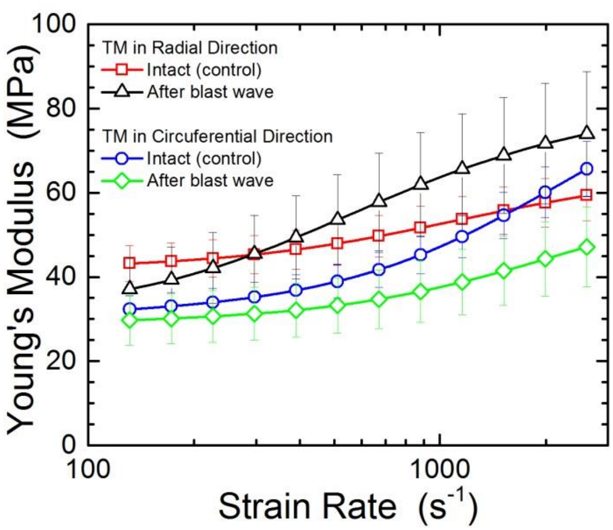

Fig. 19. Comparison of Young's modulus-strain rate curves of TM specimens obtained from the SHTB system in two groups: normal TMs and the TMs after blast exposure. The specimens were prepared along the radial and circumferential directions.

(5) The major activities under Aim 3 for Task 3-1 include: 1) establishing the method to transfer the 3D finite element (FE) model of the human ear created in traditional ANSYS V. 12 software into Workbench V. 15 in CFX/ANSYS; 2) building the geometry of the ear model with ossicular chain and cochlear load in CFX; 3) simulating the high intensity pressure wave transmission through the ear canal into the middle ear cavity based on similarity method and fluid-structure interaction (FSI) in CFX/ANSYS; 4) simulating the blast overpressure wave transmission from the ear canal to middle ear based on FSIs and the real material properties of ear soft tissues in CFX/ANSYS or Fluent/ANSYS; 5) Predicting the stress and strain distributions of the TM induced by blast wave in chinchilla ear model in two exposure conditions: open field and shielded with a helmet. The specific objectives are to develop the FE model of the human ear to predict unwarned response of the middle ear to blast overpressure and to investigate the relationship between the TM rupture and blast waveforms.

Figure 20 displays the 3D FE models of the human ear we established in CFX/ANSYS for simulation of blast wave transmission through the ear canal to middle ear. The model consists of the ear canal, TM, middle ear ossicles and suspensory ligaments, middle ear cavity, and cochlear loading. The impulse pressures at the canal entrance (P0), near the TM in the canal (P1), and behind the TM in the middle ear cavity (P2) were derived from the model. Figure 21 shows the pressure wave propagation through the ear canal when the input pressure is suddenly increased to 17 kPa or 179 dB SPL or 2.5 psi at t = 0^+ and linearly decays with $t_0 = 30\ \mu s$, where t_0 is the duration time of the input blast overpressure. In this simulation the ear is in the atmospheric condition. The results of pressure distributions show that the peak pressure ratio of P1 (34 kPa) to P0 (17 kPa) is 1.97 and the peak pressure ration of P2 (2.2 kPa) to P0 (17 kPa) is 0.13. The modeling results are comparable to the preliminary measured data from temporal bones.

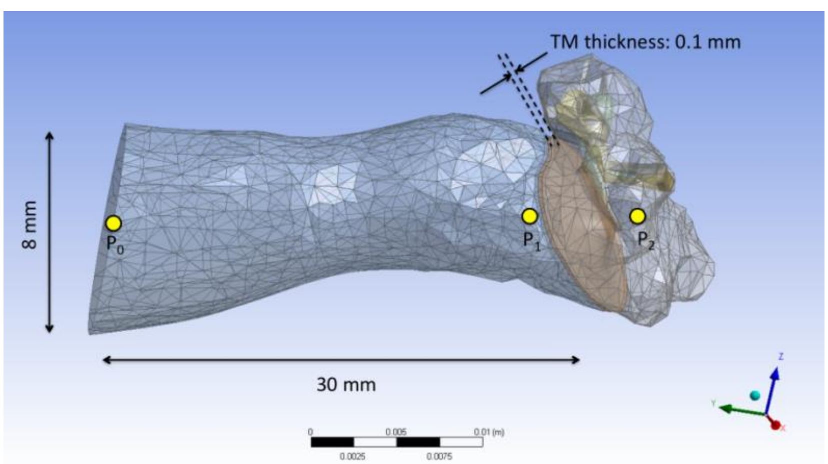

Fig. 20A. The FE model of human ear with ossicular chain inside the middle ear cavity in CFX/ANSYS. The pressure P0, P1, and P2 and the movement of the TM induced by the impulse pressure P0 at the canal entrance were calculated.

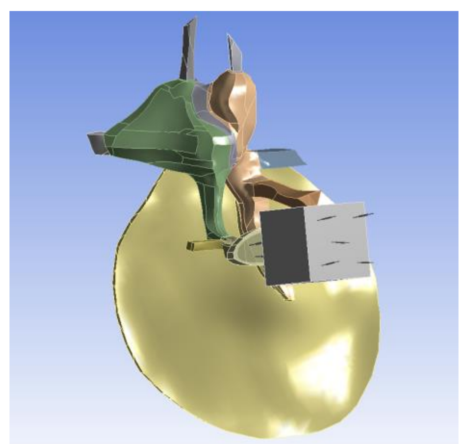

(B) The middle ear components of the TM, ossicles, and ligaments/muscle tendons with the cochlear load applied on the stapes footplate.

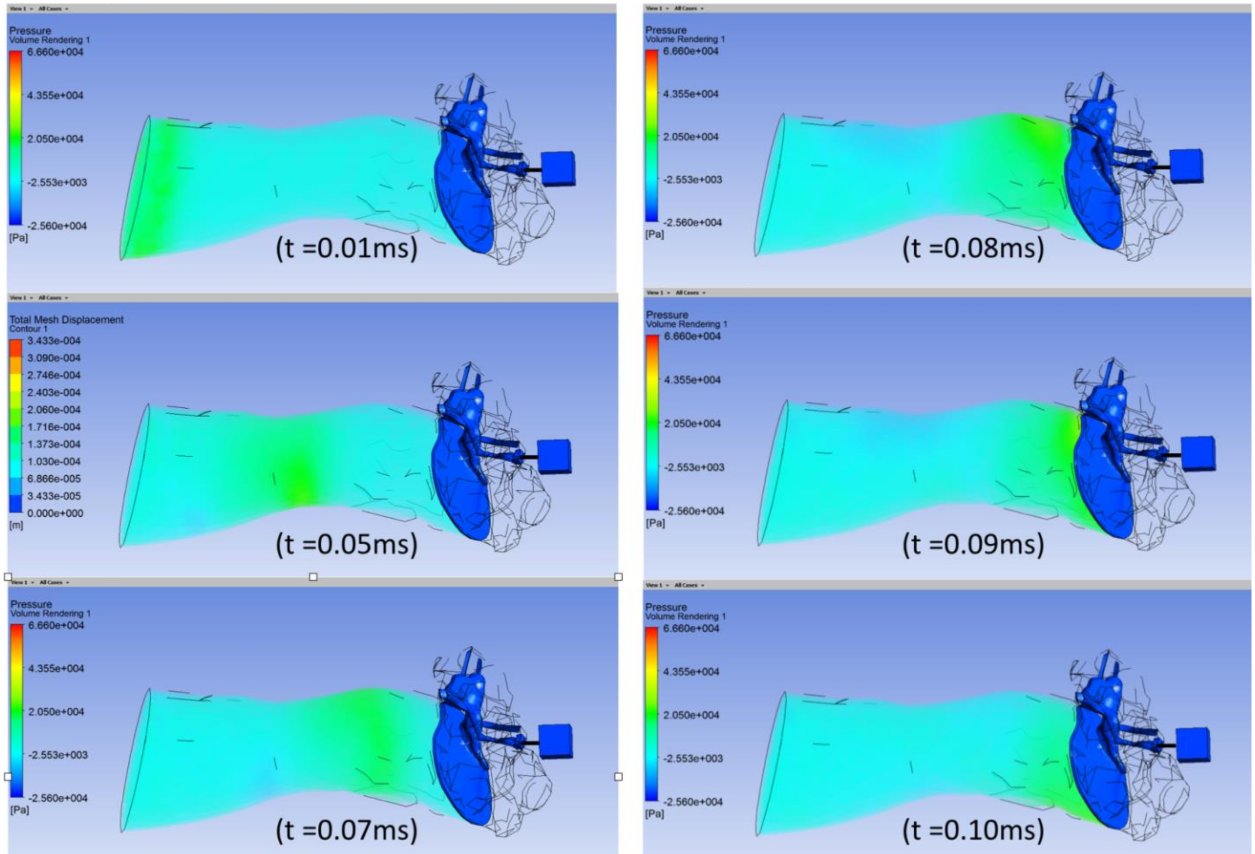

Fig. 21. Time-history plots of the pressure propagation in the human ear. The mass block (25.5 mg) attached to the stapes footplate and fixed on the bony wall through ten dash ports (0.02 Ns/m), which represents the cochlear load.

A 3D FE model of the chinchilla ear was used to predict the stress and strain distributions of the TM and the TM movement induced by blast waves in two exposure conditions: open field and shielded with a helmet. Figure 22 shows the pressure waveforms recorded in these two cases from two animals at the TM rupture threshold level. A single positive overpressure peak was observed and the peak pressure of 11.3 psi was reached within 3 ms as shown in Fig. 22A, the open field case. The waveform under the shield or helmet is obviously different from that in open field as shown in Fig. 22B. Both positive and negative peaks were reached at less than 3 ms with peak-to-peak pressure level at 3.4 psi. It suggests that under the shield or with a helmet, the TM was ruptured at a lower pressure level than that without the helmet because of the significant difference of waveforms in these two cases.

To verify this experimental finding, the pressure waveforms recorded from experiments were applied on the TM of the chinchilla FE model. The distribution of stress and strain of the TM and the displacement of the TM were calculated and the maximum stress and strain were derived. Figure 23 shows the model-derived distributions or contours of stress in the TM (Fig. 23A) and the displacement of the TM (Fig. 23B) in the open case (or under positive pressure waveform) as the time of maximum stress was reached. As shown in Fig. 23A, the stress varied from 29 to 0.13 MPa in the TM. The maximum stress of 29 MPa was at the top of the manubrium or near the flaccida above the handle of malleus.

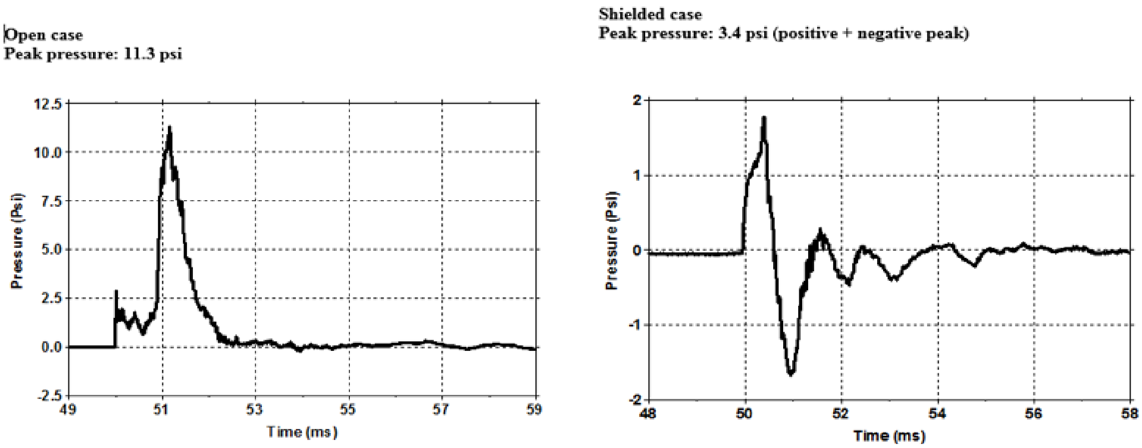

(A) (B)

Fig. 22A. Waveform recorded from a chinchilla during the open field exposure. (B) Waveform recorded from a chinchilla tested under a shield or a helmet.

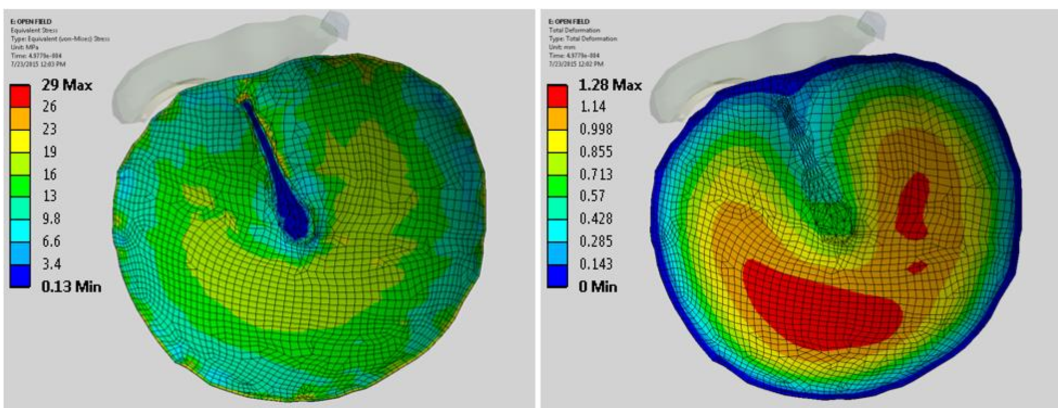

(A) (B)

Fig. 23. FE model-derived distributions of the equivalent (von Mises) stress in the TM (A) and the displacement of the TM (B) in the open case at the time when the maximum stress was reached.

Figure 24 displays the FE model-derived equivalent stress distribution in the TM (Fig. 24A) and the TM displacement (Fig. 24B) in the shielded case (or under positive-negative pressure waveform) at the time when the maximum stress was reached. The maximum stress occurred at the time 1.5 ms while the peak negative pressure was reached. As shown in Fig. 24A, in the superior region of the TM, the location of the maximum stress was the same as that of the open condition, i.e., at the top of the manubrium, and the value of maximum stress was also about 29 MPa. In the inferior side, the maximum stress of the TM was next to the umbo with a value about 15 MPa. The maximum displacement was located in the inferior portion of the TM, directly below the umbo with a value of 1.33 mm.

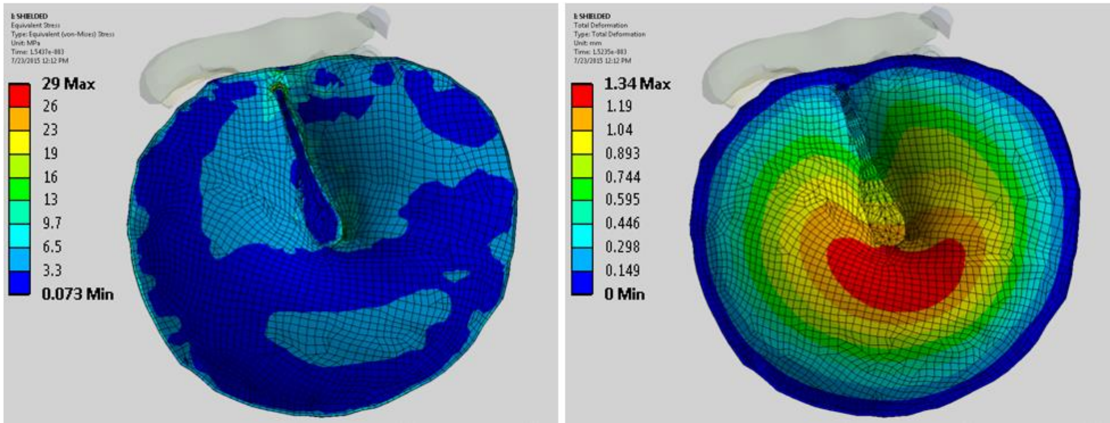

(A) (B)

Fig. 24. FE model-derived distributions of the equivalent stress in the TM (A) and the displacement of the TM (B) in the shielded case at the time when the maximum stress was reached.

The study on chinchilla TM damage or rupture during blast exposure demonstrates that the waveform pattern plays important role in TM damage. The mechanism behind this is probably due to the stress increasing rate caused by impulse pressure loading. Figure 25 shows the variation of TM stress with respect to the impulse pressure level.

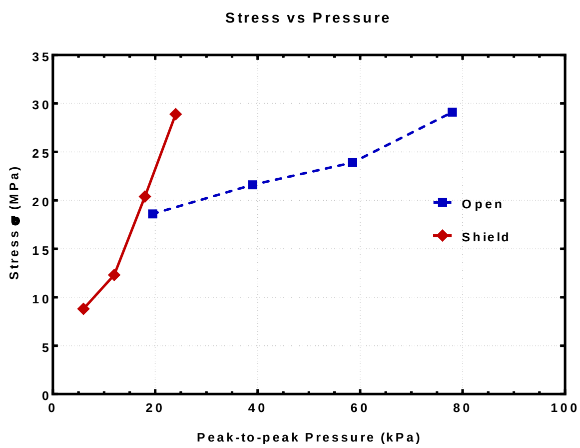

Fig. 25. Plots of FE model-derived stress increase with the peak-to-peak pressure loading in open and shielded cases. The red line with symbols was obtained from Fig. 24 in shielded case and the blue line with symbols obtained from Fig. 23 in open field.

Figure 25 indicates that the change of stress in response to pressure loading in shielded case was much higher than that in the open case. This finding reveals that the biomechanical mechanisms for blast induced TM damage in relation to overpressure waveforms may consist of the following two standard points: 1) the negative pressure component of the shielded waveform may play a crucial role for TM rupture, even though the negative peak is smaller than the positive peak; 2) the sensitivity of TM stress w. r. t. peak-to-peak pressure amplitude, $\delta\sigma/\delta p$, may characterize mechanical damage of the TM in relation to the impulse pressure waveform. This study and results were presented at the 7th International Symposium on Middle Ear Mechanics in Research and Otology (MEMRO) in July 2015 and the a manuscript was submitted to Hearing Research and is currently under review.

- **What opportunities for training and professional development has the project provided?**

Nothing to Report

- **How were the results disseminated to communities of interest?**

Nothing to Report

- **What do you plan to do during the next reporting period to accomplish the goals?**

1) We will develop a new setup with the incident wave direction from the front of face with temporal bones on the head block and measure the TM rupture threshold and damage pattern. Thus, the blast or high intensity impulse transmission through the ear along three dimensions: from the top of the head, lateral to the ear, and front of the face will all be monitored in our head block with cadaver ears. The transfer functions of the ear canal and middle ear in response to impulse sound or blast overpressure applied at the ear canal entrance will be characterized (Task 1-2).

2) The EMG measurements of middle ear muscle reflex (stapedius muscle) in response to blast exposure in chinchillas will be further investigated with more animal experiments. The data analysis will be completed with a focus on the discrepancy between stimulations, blast exposure vs. acoustic stimulus. The micro-structure of the chinchilla TM after exposed to blast (multiple blasts) will be examined using the SEM images. Using the micro-fringe projection system, the change of TM properties after blast exposure will be determined (Task 2-1).

The tissue mechanical tests on ISJ samples by using DMA system and FTS principle, on TM samples by using the acoustic loading with laser Doppler vibrometry (LDV) measurement, and on ISJ samples by using the miniature split Hopkinson tension bar (SHTB) system will be further performed after temporal bones are exposed to blast (Task 2-2).

The subcontract at UT-Dallas will use the current micro-fringe projection system to measure mechanical properties of human TM samples in pre-blast (normal TM) and post-blast exposure conditions. An automated syringe pump system for dynamic bulge test on human TM will be setup. The use of Optical Coherence Tomography (OCT) to measure the TM thickness and other techniques for measurement of the accurate geometry data to determine mechanical properties of the TM and other tissues will be explored.

3) Under Aim 3, we will solve the convergence and remeshing difficulties currently occurring in the FE model of human ear in CFX/ANSYS or Fluent/ANSYS because of the higher pressure level-induced large deformation of the TM. The realistic movement of the TM and ossicles will be determined in response to blast overpressure encountered in the experimental blast chamber (Task 3-1). We will develop the active FE model of the human ear associated with the middle ear muscle function. The EMG measurements of stapedius muscle in response to acoustic stimulation and blast exposure from chinchillas will be simulated in chinchilla FE model of the ear for modeling of the middle ear transfer function (Task 3-2).

4. IMPACT

● **What was the impact on the development of the principal discipline(s) of the project?**

The first year research findings provide the experimentally identified relationship between ear injury and the intensity or direction of the blast wave, the transfer functions of the ear canal and middle ear in response to overpressure applied at the ear canal entrance, the middle ear muscle reflex to the blast exposure, and the changes of tissue mechanical properties after blast exposure. The outcomes from the FE models predict the pressure distribution in the ear canal and middle ear cavity, distributions of stress and strain of the TM induced by blast wave, and the relationship between the TM rupture and blast waveform or the biomechanical mechanisms for blast-induced TM damage.

These new data are novel. We were unable to identify any similar, state-of-the-art studies that address the impact of blast damage to the middle ear in this way. By cataloguing the subtle as well as dramatic changes in middle ear structure and function following blast exposure at varying intensities, we have gained new insights into the susceptibility of component structures of human ear. Thus, a better understanding of prevention mechanisms of hearing loss in military operations associated with high intensity sound will be obtained upon the completion of this project.

It is expected that two products will be delivered at the end of project: 1) the standard criteria for HPDs design and evaluation based on nonlinear FE model of the human ear and biomechanics of tissue acoustic injury; and 2) the head block with cadaver ear and the FE model of human ear serving as the design, test, and evaluation platforms for passive and active HPDs.

● **What was the impact on other disciplines?**

Nothing to Report

● **What was the impact on technology transfer?**

Nothing to Report

● **What was the impact on society beyond science and technology?**

Nothing to Report

5. CHANGES/PROBLEMS

● **Changes in approach and reasons for change**

No significant changes in approach.

● **Actual or anticipated problems or delays and actions or plans to resolve them**

No significant problems and delays.

● **Changes that had a significant impact on expenditures**

No changes in expenditures.

● **Significant changes in use or care of human subjects, vertebrate animals, biohazards, and/or select agents**

The USAMRMC ACURO site visit to the University of Oklahoma (Norman, Oklahoma) was conducted on April 24, 2015. We received the report of the site visit from ACURO USAMRMC on June 10, 2015. The report provides the requirements and recommendations for our animal care and use program. We have complied with the regulations governing animal research and responded to the comments and recommendations to the satisfaction of the DOD in the report submitted to USAMRMC ACURO on August 24, 2015.

6. PRODUCTS

• publications, conference papers, and presentations;
• website(s) or other Internet site(s);
• technologies or techniques;
• inventions, patent applications, and/or licenses; and
• other products.

● **Publications, conference papers, and presentations**

Journal publications:

1. Gan, R. Z., Nakmali, D., Ji, X. D., Leckness, K., and Yokell, Z. Mechanical damage of tympanic membrane in relation to impulse pressure waveform – A study in chinchillas. *Hearing Research*, 2015 (Under Review)
2. Liang, J., Luo, H., Yokell, Z., Nakmali, D., Gan, R. Z., and Lu, H. Characterization of the nonlinear elastic behavior of chinchilla tympanic membrane using micro-fringe projection and finite element simulation, *Hearing Research*, 2015 (Under Review)
3. Hawa, T., and Gan, R. Z. Pressure distribution in a simplified human ear model for the high intensity sound transmission. *ASME J. Fluids Engineering*, Vol. 136: 111108-1 to -6, 2014.

Publications – Conference papers:

1. Gan, R. Z., Nakmali, D., Ji, X. D., and Yokell Z. Mechanical damage of tympanic membrane in relation to impulse pressure waveform – A study in chinchillas. The 7th International Symposium on Middle Ear Mechanics in Research and Otology (MEMRO), Aalborg, Denmark, July 1 – 5, 2015.
2. Luo, H., Liang, J., Nakmali, D., Gan, R. Z., and Lu, H. Mechanical Property of Human Eardrum after Exposure to Blast Wave. Technical Presentation: McMat2015-6176, *ASME 2015 Applied Mechanics and Materials Conference (McMAT2015)*, Seattle, June 29-July 1, 2015.

3. Liang, J., Luo, H., Nakmali, D., Gan, R. Z., and Lu, H. Characterization of the nonlinear elastic behavior of Chinchilla tympanic membrane using micro-fringe projection. *Society for Experimental Mechanics (SEM) 2015 Annual Conference & Exposition on Experimental & Applied Mechanics*, Costa Mesa, CA, June 8-11, 2015.
4. Hawa, T., Leckness, K., and Gan, R. Z. High Intensity Pressure Noise Transmission in Human Ear: A Three Dimensional Simulation Study. Bulletin of the American Physical Society, APS March Meeting, Vol. 60, Number 1, P1.00088, 2015.
5. Gan, R. Z**.**, Nakmali, D., and Yokell, Z. Measurement of high intensity sound pressure transmission from the ear canal to middle ear. *Association for Research in Otolaryngology (ARO) - Midwinter Meeting*, Vol. 38: PD27, Baltimore, MD, February 21-25, 2015.
6. Yokell, Z., Nakmali, D., and Gan, R. Z. Electromyography (EMG) Measurement of Chinchilla Middle Ear Muscle Reflex. *Association for Research in Otolaryngology (ARO) - Midwinter Meeting*, Vol. 38: PS142, Baltimore, MD, February 21-25, 2015.
7. Gan, R. Z., Nakmali, D., and Yokell, Z. High intensity sound wave transduction from the ear canal to middle ear. *Proceedings of the Biomedical Engineering Society 2014 Annual Meeting*, San Antonio, TX, October 22-25, 2014.
8. Hawa, T. and Gan, R. Z. Simulation of pressure wave transmission in human ear with viscoelastic tympanic membrane model. *Proceedings of the Biomedical Engineering Society 2014 Annual Meeting*, San Antonio, TX, October 22-25, 2014.
9. Yokell, Z., Nakmali, D., Jiang, S., Guan, X., and Gan, R. Z. EMG measurement of middle ear muscle reflex in chinchillas. *Proceedings of the Biomedical Engineering Society 2014 Annual Meeting*, San Antonio, TX, October 22-25, 2014.

Books or other non-periodical, one-time publications:

1. Liang, J., Luo, H., Nakmali, D., Gan, R. Z., and Lu, H. Characterization of the nonlinear elastic behavior of chinchilla tympanic membrane using micro-fringe projection. Chapter 26 in Mechanics of Composite and Multi-functional Materials, Vol. 7, Ed by K. Zimmermann, *Conference Proceedings of the Society for Experimental Mechanics Series*, (DOI: 10.1007/978-3-319-21762-8_26), Springer International Publishing Switzerland, 2015.

7. PARTICIPANTS & OTHER COLLABORATING ORGANIZATIONS

● What individuals have worked on the project?

Provide the name and identify the role the person played in the project. Indicate the nearest whole person month (Calendar, Academic, Summer) that the individual worked on the project. Show the most senior role in which the person worked on the project for any significant length of time. For example, if an undergraduate student graduated, entered graduate school, and continued to work on the project, show that person as a graduate student, preferably explaining the change in involvement.
Describe how this person contributed to the project and with what funding support. If information is unchanged from a previous submission, provide the name only and indicate “no change”.

Name: Rong Gan, Ph.D.
Project Role: PI
Researcher Identifier (OU ID): 112129499
Nearest person month worked: 3
Contribution to Project: No change

Name: Takumi Hawa, Ph.D.
Project Role: Co-PI
Researcher Identifier (OU ID): 112781159
Nearest person month worked: Dr. Hawa was terminated on May 15, 2015 and he is no longer working at the University of Oklahoma and on this project.
Contribution to Project: No change

Name: Xuelin Wang, Ph.D.
Project Role: Research Scientist
Researcher Identifier (OU ID): 112652097
Nearest person month worked: 3
Contribution to Project: No change

Name: Xiao Ji, Ph.D.
Project Role: Research Associate
Researcher Identifier (OU ID): 112902618
Nearest person month worked: 3
Contribution to Project: No change

Name: Don Nakmali, M.S.
Project Role: Research Technician
Researcher Identifier (OU ID): 112123615
Nearest person month worked: 2
Contribution to Project: No change

Name: Zachary Yokell
Project Role: Ph.D. Student
Researcher Identifier (OU ID): 112760109
Nearest person month worked: 2
Contribution to Project: No change

Name: Shangyuan Jiang
Project Role: Ph.D. Student
Researcher Identifier (OU ID): 112979369
Nearest person month worked: 2
Contribution to Project: No change

Name: Kegan Leckness
Project Role: M.S. Student
Researcher Identifier (OU ID): 113797795
Nearest person month worked: 2
Contribution to Project: No change

Name: Thomas Seale, Ph.D.
Project Role: Consultant
Researcher Identifier (OU ID): HR000774
Nearest person month worked: 0.2
Contribution to Project: Dr. Seale has worked on the project in helping animal studies in chinchillas.

Name: Mark Wood, M.D.
Project Role: Consultant
Researcher Identifier: 1624
Nearest person month worked: 0.2
Contribution to Project: Dr. Wood has regular meeting with PI on the project in helping studies in temporal bones and HPDs.

Name: Hongbing Lu, Ph.D.
Project Role: PI at UTD (subcontract)
Researcher Identifier (UTD ID): 2011733939
Nearest person month worked: 2
Contribution to Project: No change

Name: Junfeng Liang, Ph.D.
Project Role: Post-Doc
Researcher Identifier (UTD ID): N/A
Nearest person month worked: 3
Contribution to Project: No change

Name: Huiyang Luo, Ph.D.
Project Role: Research Scientist
Researcher Identifier (UTD ID): 0000-0001-7149-8609
Nearest person month worked: 2
Contribution to Project: No change

Name: Tingge Xu
Project Role: Ph.D. student
Researcher Identifier (UTD ID): N/A
Nearest person month worked: 2
Contribution to Project: No change

- **Has there been a change in the active other support of the PD/PI(s) or senior/key personnel since the last reporting period?**

Nothing to Report.

- **What other organizations were involved as partners?**

Nothing to Report.

8. SPECIAL REPORTING REQUIREMENTS

QUAD CHARTS: The Quad Chart (available on https://www.usamraa.army.mil) shall be updated and submitted as an appendix.

A Quad Chart is submitted as an appendix.

9. APPENDICES

● **Quad Chart**

● **Appendix A.** Gan, R. Z., Nakmali, D., Ji, X. D., Leckness, K., and Yokell, Z. Mechanical damage of tympanic membrane in relation to impulse pressure waveform – A study in chinchillas. *Hearing Research*, 2015 (Under Review)

● **Appendix B**. Liang, J., Luo, H., Yokell, Z., Nakmali, D., Gan, R. Z., and Lu, H. Characterization of the nonlinear elastic behavior of chinchilla tympanic membrane using micro-fringe projection and finite element simulation, *Hearing Research*, 2015 (Under Review)

● **Appendix C.** Luo, H., Liang, J., Nakmali, D., Gan, R. Z., and Lu, H. Mechanical Property of Human Eardrum after Exposure to Blast Wave. Technical Presentation: McMat2015-6176, *ASME 2015 Applied Mechanics and Materials Conference (McMAT2015),* Seattle, June 29-July 1, 2015.

● **Appendix D.** Hawa, T., and Gan, R. Z. Pressure distribution in a simplified human ear model for the high intensity sound transmission. *ASME J. Fluids Engineering*, Vol. 136: 111108-1 to -6, 2014.

Biomechanical Modeling and Measurement of Blast Injury and Hearing Protection Mechanisms

ERMS# 13063031 Task Title: Measuring and modeling of blast wave transduction through the ear canal
Award Number: W81XWH-14-1-0228
PI: Rong Z. Gan, Ph.D. **Org:** University of Oklahoma **Award Amount:** $2,521,486

Study/Product Aim(s)

- Quantify middle ear injury in relation to blast pressure level and wave direction and overpressure transduction through the ear
- Identify middle ear protection mechanisms by detecting middle ear muscle reflex and measuring mechanical changes of ear tissues
- Develop the FE model of human ear to predict unwarned and warned responses of the middle ear to blast exposure

Approach

- Identify blast-induced eardrum and middle ear damage and the blast pressure transmission through the ear with multiple sensors inserted in cadaver ears
- Detect the acoustic reflex on EMG of middle ear stapedius muscle
- Measure mechanical properties of ear tissues after blast exposure
- Conduct nonlinear FE analysis on 3D FE model of the human ear – passive and active ear models in CFX/ANSYS
- Simulate the HPDs in FE model to derive prevention mechanisms

Blast Pressure Transmission from Ear Canal to Middle Ear

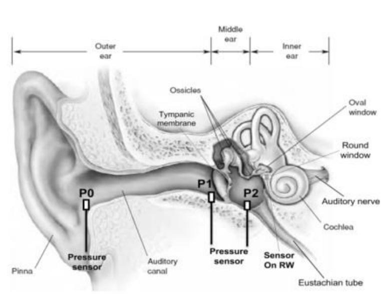

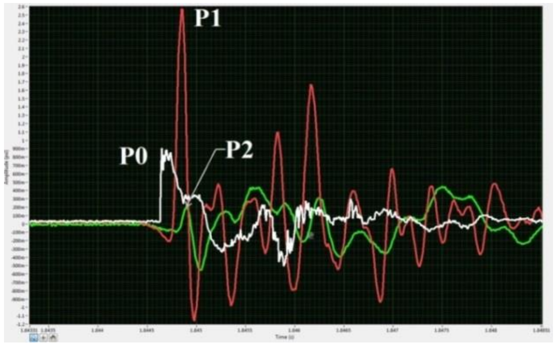

Overpressure P0 at the canal entrance, P1 near the eardrum, and P2 inside middle ear are monitored in cadaver ears during blast exposure.

Accomplishment: TM rupture threshold and pressure wave transmission were measured in blast tests at vertical and horizontal setups in human cadaveric ears; TM rupture and EMG measurement in chinchillas were conducted; dynamical test of ISJ and TM were performed; relationship between TM rupture and waveform in chinchilla was investigated in FE model.

Timeline and Cost

Activities CY	15	16	17	18
Tasks 1-1 and 1-2 (Blast injury)				
Task 2-1 (Acoustic reflex-EMG)				
Task 2-2 (Tissue mechanics)				
Tasks 3-1, 3-2, and 3-3 (FE modeling of blast injury)				
Estimated Budget ($K)	**$619**	**$623**	**$641**	**$638**

Updated: August 30, 2015

Goals/Milestones

CY15 Goals – Establish measurement and modeling of blast overpressure
☑ Identify eardrum/middle ear damage thresholds and setup EMG measurement and tissue mechanical testing
☑ Building passive FE model of the ear for analysis of blast wave
CY16 Goals – Characterization of middle ear function
☐ Investigate ear canal/middle ear transfer function and muscle function
☐ Continue tissue mechanical testing and validate the passive FE model
CY17 Goals – Middle ear protection mechanisms and active model
☐ Complete muscle function test and continue tissue mechanical tests
☐ Develop active FE model of the model for blast wave analysis
CY18 Goals – Validate active FE model with applications
☐ Complete nonlinear active model and ear tissue testing
☐ Evaluate HPDs in FE model of the ear for hearing protection

Comments/Challenges/Issues/Concerns

- EMG measurement in animals and blast test in cadaver ears began.

Budget Expenditure to Date

Projected Expenditure: $619,001.00
Actual Expenditure: $487,376.49 (approximate)

Mechanical Damage of Tympanic Membrane in Relation to Impulse Pressure Waveform – A Study in Chinchillas

Rong Z. Gan, Don Nakmali, Xiao D. Ji, Kegan Leckness, and Zachary Yokell

School of Aerospace and Mechanical Engineering and Biomedical Engineering Center

University of Oklahoma, Norman, OK

Corresponding author:

Rong Z. Gan, Ph.D.

Professor of Biomedical Engineering

School of Aerospace and Mechanical Engineering and Bioengineering Center

University of Oklahoma

865 Asp Avenue, Room 200

Norman, OK 73019

Phone: (405) 325-1099

Fax: (405) 325-1088

E-mail: rgan@ou.edu

ABSTRACT

Mechanical damage to middle ear components in blast exposure directly causes hearing loss, and the rupture of the tympanic membrane (TM) is the most frequent injury of the ear. However, it is unclear how the severity of injury graded by different patterns of TM rupture is related to the overpressure waveforms induced by blast waves. In the present study, the relationship between the TM rupture threshold and the impulse or overpressure waveform has been investigated in chinchillas. Two groups of animals were exposed to blast overpressure simulated in our lab under two conditions: open field and shielded with a helmet covering the animal head. Auditory brainstem response (ABR) and wideband tympanometry were measured before and after exposure to check the hearing threshold and middle ear function. Results show that waveforms recorded in the shielded case were different from those in the open field and the TM rupture threshold in the shielded case was lower than that in the open field (3.4 vs. 9.1 psi or 181 vs. 190 dB SPL). The impulse pressure energy spectra analysis of waveforms demonstrates that the shielded waveforms include greater energy at high frequencies than that of the open field waves. Finally, a 3D finite element (FE) model of the chinchilla ear was used to compute the distributions of stress in the TM and the TM displacement with impulse pressure waves. The FE model-derived change of stress in response to pressure loading in the shielded case was substantially higher than that in the open case. This finding provides the biomechanical mechanisms for blast induced TM damage in relation to overpressure waveforms. The TM rupture threshold difference between the open and shielded cases suggests that an acoustic role of helmets may exist, intensifying ear injury during blast exposure.

Keywords: Tympanic membrane, blast overpressure, ear injury biomechanics, helmet, finite element modeling

1 INTRODUCTION

Exposure to high intensity sound or blast overpressure waves is considered to be an intrinsic situation faced by military personnel involved in most operational activities. The direct consequences of high-intensity noise and blast injuries to the auditory system are acute hearing loss, which immediately affects the normal functioning of soldiers in combat operations, and the resultant long-term hearing disabilities that occur in a significant fraction of veterans (Patterson and Hamernik, 1997; Garth, 1994; Karmy-Jones et al., 1994; Gondusky and Reiter, 2005; Fausti et al., 2009).

Blast overpressure is a high intensity disturbance in the ambient air pressure that creates high intensity sound (impulse) over 170 dB SPL. When exposed to a blast, the human auditory system is vulnerable to both peripheral and central damage from the overpressure (Patterson and Hamernik, 1997; Mayorga, 1997). Rupture of the eardrum or tympanic membrane (TM) is the most frequent injury of the ear and has been investigated in animals and humans with wide variability (Hirsch, 1966; Patterson and Hamernik, 1997; Richmond et al., 1989). The literature indicates that mechanical damage to components of the auditory system is the major cause for hearing loss after blast exposure. However, it is not clear how the severity of injury graded by different patterns of TM rupture is related to the overpressure waveforms induced by blast exposure. Particularly, no quantitative study on biomechanical changes of the TM in response to different pressure waveforms has been reported in the literature.

In this paper, we report our currently completed study on relationships between the TM rupture threshold, the TM damage pattern, and the overpressure waveforms using a chinchilla animal model. The chinchilla is a commonly used animal model for auditory research with large TMs, ossicular dimensions, and middle ear spaces for an animal of its size. The chinchilla's range of hearing is similar to that of humans (Heffner R. and Heffner, H. 1991; Richmond et al., 1989; Hedegaard and Bonding, 1993). In the present study, two groups of animals were exposed to high intensity sound pressure under two conditions: the open field without a shield and the shielded case with a helmet covering the animal head. By increasing the blast peak pressure level, the TM was finally ruptured and the pressure waveforms at the entrance of the ear canal were recorded simultaneously. The goal of this study was to determine whether there is a change of overpressure waveform under the helmet and how the waveform change affects the TM rupture threshold.

In addition to experimental testing in animals, impulse pressure energy spectra analysis of the waveforms recorded under open and shielded conditions was performed to determine signal energy flux over 10 frequency bands. The 3D finite element (FE) model of the chinchilla middle ear recently developed in our lab was employed to calculate the distributions of the stress and strain in the TM with impulse pressure profiles recorded in open and shielded conditions. The FE modeling results reveal that a waveform pattern consisting of both positive and negative pressures in the shield case (under a helmet) contributes more greatly to TM damage than the positive overpressure in the open case. This finding provides the biomechanical mechanisms for blast induced TM damage in relation to overpressure waveforms. The TM rupture threshold difference between the open and shielded cases suggests that an acoustic role of helmets may exist, intensifying ear injury during blast exposure.

2 METHODS

2.1 Animal study protocol

Eighteen chinchillas (*Chinchilla laniger*) weighing between 600-800 g were included in this study. The study protocol was approved by the Institutional Animal Care and Use Committee of the University of Oklahoma and met the guidelines of the National Institutes of Health and the United States Department of Agriculture (USDA). All animals were established to be free from middle ear disease, as evaluated by otoscopic examination, at the beginning of the study.

A well-controlled compressed air (nitrogen)-driven blast apparatus located inside an anechoic chamber in the Biomedical Engineering Laboratory at the University of Oklahoma was used to simulate blast exposure in this study (Hawa and Gan, 2014). Polycarbonate film (McMaster-Carr, Atlanta, GA) of varying thickness (130 μm and 260 μm) was employed to generate blast overpressure of at least 30 psi (200 dB SPL). The overpressure level was controlled by varying the distance from the blast reference plate. Figure 1A shows a schematic of the blast apparatus with the animal holder placed at the center.

The animals were divided into two groups: one group of 9 animals was exposed to blast in an “open field” (Fig. 1A) and another group of 9 animals was exposed to blast with a shield or helmet covering the animal head as shown in the schematic of Fig. 1B and the picture of Fig. 1C. The animals in both groups were first tested with the pre-exposure measurements, including middle ear energy absorbance (EA) using wideband tympanometry (Model AT235h, Interacoustic, MN) and auditory brainstem response (ABR) using TDT system III (Tucker-Davis Technology, Alachua, FL). A tone burst stimulus at frequencies of 0.5, 1, 2, 4, and 8 kHz was applied in the ear canal (Guan and Gan, 2011; Jeselsohn et al., 2005; Petrova et al., 2006; Qin et al., 2010). The EA measurement was used as a check of the TM intagrity and normal function of the middle ear. The ABR measurements provided the change of hearing threshold of the ear after blast exposure. The animal was anesthetized with mixed ketamine (10 mg/kg) and xylazine (2 mg/kg). To maintain consistent measurement of ABR, tympanometry, and blast pressure level, the pinna was removed.

After pre-exposure testing, the animal was placed into a specially designed animal holder. A pressure sensor (Model 102B16, PCB Piezotronics, Depew, NY) was placed at the entrance of the ear canal (1 cm lateral to the ear canal opening) with the sensing surface facing the blast in both open and shielded cases. During the shielded test, the animal head was covered by a helmet (stainless steel, Fig. 1C) and the edge of the helmet was flushed with the sensor. The animal within the holder was moved to the testing chamber for blast exposure.

The pressure sensor signal was measured by cDAQ 7194 and A/D converter 9215 (National Instruments Inc., Austin, TX) with the sampling rate of 100k/s (10 μs). The LabVIEW software package (NI Inc.) was used for data acquisition and analysis. The waveform of each blast test was saved in a PC for further analysis. Note that the chinchilla shield was adjustable with relative position from the animal head. The shield edge was flush with the pressure sensor surface and there was a distance of about 3 cm from the animal head to the internal top surface of the shield.

It usually took 2-3 interactions of blast tests to reach the TM rupture threshold which was defined as the peak pressure before the TM rupture. The initial blast pressure level was selected based on the system calibration using different films and changing the distance between the sensor surface and the blast reference plane. The number of blast tests also varied with individual chinchillas due to the variation among the animals and setups. To confirm the TM damage, an otoscopic examination of both ears was performed first and further verification using wideband tympanometry was done to determine whether the TM was ruptured. When the TM was found without rupture, the next blast test was conducted with an increase of overpressure level. The testing stopped when one ear was ruptured.

Post-exposure measurements included wideband tympanometry to verify whether the TM was ruptured or damaged in both ears and ABR measurement in the ears with intact TMs to determine the hearing threshold shift after exposure. The TM damage pattern was recorded by taking pictures after the animal was euthanized and the bulla was dissected.

2.2 Waveform analysis

Impulse pressure energy spectra analysis on recorded waveforms in the time domain was conducted in MATLAB to determine the signal energy distribution over the frequencies under open and shielded conditions. First, the recorded pressure waveforms were converted to pressure distributions over the frequencies of 20–5000 Hz by using FFT spectral analysis. Next, following the methods of impulse signal energy distribution theory reported by Hamernik et al. (1991a, 1991b, 2001) and Young (1970), the total sound exposure was divided by the standard characteristic impedance of the air ρc as impulse energy flux (energy per unit area) and expressed as:

$$E^* = \frac{1}{\rho c}\int_0^T p^2(t)dt \quad , \qquad [\mathrm{J/m^2}] \qquad (1)$$

where $p(t)$ is the instantaneous value of acoustic pressure in Pa or N/m^2, dt is the time increment for scanning of acoustic pressure in seconds, and ρc = 406 mks rayls to produce a quantity with units of energy flux (i.e., J/m^2). Both and c are pressure-dependent in the shock front. The duration of T = 50 ms was used for calculation in the present study.

Eight octave band passing filters with center frequencies at 125 Hz, 250 Hz, 500 Hz, 1 kHz, 2 kHz, 4 kHz, 8 kHz, and 16 kHz were designed. A low pass filter L125 and a high pass filter H16k were also designed to catch signals at frequency lower than 125 Hz and higher than 16 kHz. The filtered signals were then generated and the sound energy in each band was calculated as the distribution of pressure energy flux over 10 bands. Instead of directly comparing the energy flux values in the open field and shielded case, the energy in each band was normalized with respect to the total sound energy in that band.

2.3 Finite element modeling prediction

A 3D finite element model of the chinchilla ear has been developed in our lab and is currently under review for publication (Wang and Gan, 2015). The model was built based on X-ray micro-CT images of an entire chinchilla bulla, consisting of the ear canal, TM, middle ear ossicles and suspensory ligaments, and middle ear cavity. In this study, the FE model was used to calculate the distribution of the stress and strain in the TM with impulse pressure waveforms measured under open and shielded conditions. To simplify the modeling process, the ear canal and middle ear cavity were not included in the model as shown in Fig. 2. Figure 2A shows the lateral view of the model with a TM diameter of 8.83 mm along the manubrium or malleus long process and 9.72 mm perpendicular to the manubrium. Surface area of the TM was 74.71 mm^2 and the thickness was 15 μm. Figure 2B shows the posterior view of the model with a height of cone at 1.65 mm. The TM and ossicles were suspended by the TM annulus (TMA), anterior malleal ligament (AML), posterior incudal ligament (PIL), posterior stapedial tendon (PST), tensor tympani tendon (TTT), and stapedial annual ligament (SAL). In the chinchilla ear, the malleus and incus are fused as the malleus-incus complex and the incus-stapes joint still exists. The mechanical properties of the TM and middle ear tissues are provided by Wang and Gan (2015) and enclosed in this paper as Table A1 in the Appendix.

The effect of cochlear fluid on acoustic-mechanical transmission through the ossicular chain or cochlear load was modeled as a mass block and 10 dashpots attached between the stapes footplate and fixed boundary. The average cochlear impedance was about 100 GΩ as reported by Slama et al. (2010). The impedance value of 100 GΩ was applied on 2.45 mm^2 of the stapes footplate to determine the dashpot damping, which resulted in a damping coefficient of 0.06 Nm/s for each dashpot.

The representative pressure waveforms recorded in the open and shielded cases (pressure vs. time plots) were applied on the TM surface and the calculation was performed in CFX-ANSYS (ANSYS Inc., Canonsburg, PA). FE modeling of the TM and other soft tissue responses to impulse pressure waves used the fluid-structure interaction (FSI) analysis with geometry nonlinearity of the tissues. The output from modeling included the stress and strain distributions in the TM and the TM displacement distribution. The FE modeling results characterized mechanical damage of the TM in relation to impulse pressure waveforms.

3 RESULTS

3.1 Experimental results

The damage of the TM observed from chinchilla ears after exposure in both open and shielded conditions showed certain patterns that were related to the blast pressure level. Figure 3 displays otoscopic photographs of chinchilla TMs in a normal or intact ear (Fig. 3A) and injured ears (Figs. 3B-3D). The severity of TM rupture increased from Figs. 3B to 3D. A small split along the radial direction of the TM was shown in Fig. 3B and a large split along the radial direction was shown in Fig. 3C. The damage patterns show that the TM tissue strength varies in radial and circumferential directions and the collagen fibrous structure of the TM results in relatively weak mechanical properties along the circumferential direction. Under high intensity sound or blast overpressure, the TM damage pattern is closely related to variation of mechanical properties across the TM membrane. When blast pressure level further increased, a large perforation about the half of the TM surface in the inferior side was observed as shown in Fig. 3D.

Figures 4A and 4B show the typical waveforms of pressure amplitude (rupture threshold level) in units of psi over a time of 10 ms recorded from two chinchillas in open field testing. A single positive overpressure peak was observed and peak pressures of 9.8 psi (Fig. 4A) and 11.3 psi (Fig. 4B) were reached within 3 ms as shown in these two figures. The spectral behavior of the waveforms in Figs. 4A and 4B at frequencies of 20-5000 Hz by FFT analysis is displayed in Figs. 4C and 4D, respectively. There was a plateau of 50-55 dB at low frequencies (<200 Hz), and then the pressure level monotonically decreased to around zero as frequency increased to 5000 Hz.

Table 1 lists the measured TM rupture thresholds for animals tested in open field. The mean value of the TM rupture threshold measured from 9 animals in open field was 9.1 psi or 190 dB SPL or 62.7 kPa with a standard deviation (S.D.) of ±1.7 psi (N=9).

Figures 5A and 5B show the waveforms of pressure (rupture threshold level) recorded from two animals in shielded testing. The waveform under the shield or helmet is obviously different from that in open field. Both positive and negative peaks were reached at less than 3 ms. The peak-to-peak pressure levels were 3.5 psi and 3.4 psi for Figs. 5A and 5B, respectively. This suggests that under the shield or with a helmet, the TM was ruptured at a lower pressure level than that without the helmet. The spectral behavior of the waveforms in Figs. 5A and 5B is displayed in Figs. 5C and 5D, respectively. It can be seen that under the shielded test there was no perfect plateau like that observed in open field at lower frequencies (Figs. 4C and 4D) and the peak pressure around 50 dB was reached at about 1000 Hz and decreased to zero as frequency increased to 5000 Hz.

Table 2 lists the measured TM rupture thresholds for animals tested in the shielded case. The mean value of the TM rupture thresholds measured from 9 animals with helmet was 3.4 ±0.68 psi (N=9) or 181 dB SPL. Comparing the results listed in Tables 1 and 2, a significant difference in the TM rupture thresholds between the open and shielded cases was revealed. With a helmet, the TM rupture occurred at a much lower impulse pressure than that in the open field.

Wideband tympanometry was used as an effective tool to detect TM damage in this study. The pre- and post-exposure tympanometry measurements were focused on the change of energy absorbance of the middle ear. The peak EA happens when the pressure of the middle ear equals that of the external ear in a normal ear with intact TM. When there is a perforation, the EA is low and flat. However, if the TM was not ruptured after blast, the EA measured at the pre- and post-blast exposure from 8 ears did not show significant difference between the pre- and post-exposure by paired t-test (detailed results not included here). This indicates that a TM rupture, even a small split, affects the EA measurement substantially.

Hearing threshold shift data were obtained by taking the difference of ABR measurements obtained pre- and post-blast exposure for ears without rupture. The threshold shift indicates the hearing loss induced by blast exposure, which may involve outer ear and middle ear disorder. Figure 6 shows the ABR hearing threshold shift obtained from 13 ears. The hearing threshold was measured at 5 frequencies: 0.5, 1, 2, 4 and 8 kHz. It can be seen that the blast exposure caused ABR hearing threshold shift, particularly at high frequencies. A 10-20 dB threshold increase was measured at frequencies of 2-8 kHz, which means the high frequency hearing loss is greater than the low frequency hearing loss induced by blast exposure. While there was no mechanical damage observed visibly in the middle ear, neuronal damage had already occurred.

3.2 Impulse energy spectra analysis

The sound pressure signal in the open field (Figs. 4A and 4B) is a shock wave-like impulse and the pressure signal in the shielded case (Figs. 5A and 5B) is a complex wave-like waveform as observed in our experiments. The impulse wave is completely changed under the shield or helmet. However, both waveforms are impulse pressure profiles (short duration and non-periodic) and the signal energy flux calculation was performed for all recorded waveforms in open and shielded groups over 10 octave frequency bands. Table 3 lists the calculated normalized energy flux for the open and shielded groups (N=9 for each group) over 10 bands with mean and S.D. Note that the data were normalized with respect to the total signal energy in each group and the total value was 1.0 as shown in the table.

Figure 7 displays the distribution of energy flux (normalized) based on the data in Table 3. It clearly shows the different energy flux over frequencies in the open and shielded cases. Under open field condition, the majority of energy flux are presented at lower frequencies below 500 Hz. However, under shielded condition, the energy flux is mainly involved at 500 and 1000 Hz. The results demonstrate that the different pressure waveforms in open and shielded cases implicate the different energy distribution characteristics involved in these two exposures.

3.3 FE modeling results

The pressure waveforms recorded from the open field test (Fig. 4B) and the shielded test

(Fig. 5B) were selected as blast pressure loading on the TM in the FE model of the chinchilla ear shown in Fig. 2. Two simulations were created: open case with positive peak pressure of 11.3 psi over 1 ms duration and the shielded case with peak pressure of positive 1.7 psi and negative 1.7 psi, or peak-to-peak pressure of 3.4 psi, over 1.5 ms duration.

Figure 8 shows the model-derived distributions or contours of stress in the TM (Fig. 8A) and the displacement of the TM (Fig. 8B) in the open case (or under positive pressure waveform) as the time of maximum stress was reached. In this study, the equivalent (von Mises) stress was used as a measure of the stress state of the TM. As shown in Fig. 8A, the stress varied from 29 to 0.13 MPa in the TM. The maximum stress of 29 MPa was at the top of the manubrium or near the flaccida above the handle of malleus. The second high stress region of the TM was located in the inferior side along the middle region between the annulus and umbo with the stress ranging from 16 to 19 MPa. Figure 8B displays the FE model-predicted TM displacement distribution. The maximum displacement of 1.28 mm was located in the inferior-posterior quadrant, approximately midway between the annulus and umbo. The displacement in the region of the manubrium was the smallest.

Figure 9 displays the FE model-derived equivalent stress distribution in the TM (Fig. 9A) and the TM displacement (Fig. 9B) in the shielded case (or under positive-negative pressure waveform) at the time when the maximum stress was reached. The maximum stress occurred at the time 1.5 ms while the peak negative pressure was reached. As shown in Fig. 9A, in the superior region of the TM, the location of the maximum stress was the same as that of the open condition, i.e., at the top of the manubrium, and the value of maximum stress was also about 29 MPa. In the inferior side, the maximum stress of the TM was next to the umbo with a value about 15 MPa. The maximum displacement was located in the inferior portion of the TM, directly below the umbo with a value of 1.33 mm.

A comparison of the results obtained in shielded case (Fig. 9) with those obtained in open field (Fig. 8) indicates that the same maximum stress was arrived at in both open and shielded cases with two different pressure waveform loadings. It is also found that for both open and shielded conditions, the maximum TM displacements were similar, but the location of maximum displacement in shielded condition was closer to the umbo than that of the open condition. This result verifies that the model-predicted stress relationships induced by impulse pressure waves recorded in blast tests were consistent with the observed phenomena in TM rupture because the maximum stress levels resulted in the TM rupture should be identical for two pressure waveforms or two animals with the same TM material properties.

Luo et al. (2009) measured the TM failure stress using a miniature split Hopkinson tension bar, and their results showed that the ultimate tensile stress of the TM increased with increasing strain rate, and the orientation of TM sample had a strong influence on the ultimate tensile stress. The mean ultimate stress of TM in the circumferential direction was 7.7 MPa with a strain rate of 772/s, and 13.7 MPa with a strain rate 1353/s. Since the strain rate was not derived from the two waveforms in the present study, the TM strain rate associated with the two waveforms and its effect on the rupture threshold need further investigation.

4 DISCUSSION

4.1 What we found from the chinchilla study?

In this study, mechanical damage of the TM in chinchilla ears after exposure to high intensity sound or blast has been investigated in two groups of animals under two exposure conditions: open field and shielded with a helmet. The results show that the TM rupture threshold in the shielded case was lower than that in the open field with the mean values obtained from 9 animals. The waveforms recorded during the tests from these two groups are different: a single positive impulse pressure wave obtained from the open test and the almost equal positive-negative waves obtained from the shielded test. These experimental results provide the evidence that the TM damage induced by blast overpressure is closely related to impulse pressure waveforms at the entrance of the ear canal which determine the energy level and frequency components of the sound signal to be transmitted into to the ear.

4.2 How to explain the results?

Two methods have been used for analysis of the TM damage results in this study with a focus on relationship between the TM rupture threshold and impulse pressure waveform.

(1) The impulse pressure energy spectra for waveforms recorded from each animal was analyzed over 10 octave frequency bands. The normalized energy flux at each band was then calculated from each animal and the mean values with S.D. were derived and displayed in Fig. 7 for both open and shielded groups. The spectra difference between these two groups suggests that the positive-negative pressure waveform in the shielded case carried more energy at high frequencies than that of the open case. This finding verifies that the spectra behavior of impulse signal energy distribution over frequency bands is different in these two waveforms for the open and shielded conditions. However, the direct analysis of TM mechanical damage in relation to impulse pressure waveform needs further clarification.

(2) The 3D finite element model of the chinchilla middle ear (Fig. 2) was used to derive the stress/strain distribution in the TM and the TM displacement when the pressure waves were applied on the TM over a very short time duration (<3 ms, Figs. 4B and 5B). The FE modeling

results shown in Figs. 8 and 9 provide the contour distributions of the stress and displacement at the time when the maximum stress was reached, which reflected the stress and movement of the TM at the rupture threshold level. To examine the change of stress in the TM in response to rapid pressure loading, we applied the pressure waves on the TM at four levels: 25%, 50%, 75%, and 100% of the rupture pressure level. The results are shown in Fig. 10 as the variation of TM stress with respect to the impulse pressure level.

As can be seen in Fig. 10, the change of stress in response to pressure loading in shielded case was much higher than that in the open case. This finding reveals that the biomechanical mechanisms for blast induced TM damage in relation to overpressure waveforms may consist of the following two standard points: 1) the negative pressure component of the shielded waveform may play a crucial role for TM rupture, even though the negative peak is smaller than the positive peak; 2) the sensitivity of TM stress w. r. t. peak-to-peak pressure amplitude, / p, may characterize mechanical damage of the TM in relation to the impulse pressure waveform.

4.3 Future studies

This is the first time the TM damage in relation to blast pressure waveforms has been investigated by using the 3D FE model of the chinchilla ear. This approach is based on experimental measurements in animals and the FE mechanical analysis of the TM or middle ear structure response to blast overpressure waves. The results and findings from this study, though limited to two cases, may have general contributions for understanding the mechanisms of TM damage during the blast exposure. In our future studies, we will continue the investigation along this direction on mechanisms of the TM and other ear tissue damages in relation to blast overpressure waveforms. We will also face challenges for development of the failure criteria for

TM, a multiple layer membrane tissue, in response to high intensity sound and blast overpressure.

It is also worth noting that the present study has demonstrated that the TM rupture threshold in the shielded case with a helmet covering the animal head was lower than that in the open field, when the animal was exposed to blast overpressure. This suggests that an acoustic role of helmets may exist which intensifies ear injury during blast exposure. However, more studies on a helmet's effect on possible TM damage are needed in addition to its protection function to traumatic brain injury.

5 CONCLUSIONS

The relationship between the TM rupture threshold and the impulse or overpressure waveform has been investigated in chinchillas. Two groups of animals were exposed to blast overpressure under two conditions: open field and shielded with a helmet covering the animal head. The waveforms recorded in the shielded case had almost equal positive-negative pressure phases while the waveforms recorded in the open field had the positive pressure only. The average TM rupture threshold measured in shielded case was lower than that in the open field (3.4 vs. 9.1 psi or 181 vs. 190 dB SPL). The positive-negative pressure waveform in the shielded case delivered more energy at high frequencies to the ear canal while the positive pressure only waveform in the open case carried energy limited at lower frequencies. The FE modeling results further revealed that the biomechanical mechanisms for blast induced TM damage in relation to the overpressure waveform may consist of two standard points: the role of the negative pressure component and the rate of stress change w.r.t. impulse pressure loading increasing. The TM rupture threshold difference between the open and shielded cases may suggest that an acoustic role of the helmet may exist which intensifies ear injury during blast exposure.

ACKNOWLEDGEMENTS

We thank Prof. Ning Xiang, Ph.D., Architectural Acoustics at Rensselaer Polytechnic Institute for his valuable discussions on acoustics analysis. This work was supported by DOD W81XWH-14-1-0228 and NIH R01DC011585 grants.

FIGURE LEGENDS

Figure 1. (color online) (A) Schematic of animal experimental setup with blast apparatus in the open field testing. (B) Schematic of animal experimental setup in the shielded test with a shield. (C) Picture of the animal inside the holder covering the head by a helmet in the testing chamber.

Figure 2. (color online) Finite element (FE) model of chinchilla middle ear. (A) Lateral view of the FE model with the tympanic membrane (TM), malleus-incus (M-I) complex, anterior malleal ligament (AML), posterior incudal ligament (PIL), and TM annulus (TMA). (B) Posterior view of the FE model with manubrium, PIL, tensor tympani tendon (TTT), stapes, stapedial annual ligament (SAL), and cochlear load.

Figure 3. (color online) Otoscopic pictures of the chinchilla TMs. (A) Normal chinchilla TM. (B-D) TM ruptured after blast exposure with different severity: (B) a small split along the radial direction; (C) a large split along the radial direction; and (D) severe rupture of the TM.

Figure 4. (color online) (A) The overpressure waveform recorded in one chinchilla in open field testing and (C) the impulse pressure spectra obtained from this animal’s waveform. (B) The overpressure waveform recorded in another chinchilla in open field testing and (D) the impulse pressure spectra obtained from this animal’s waveform.

Figure 5. (color online) (A) The overpressure waveform recorded in one chinchilla in shielded testing and (C) the impulse pressure spectra obtained from this animal’s waveform. (B) The overpressure waveform recorded in another chinchilla in shielded testing and (D) the impulse pressure spectra obtained from this animal’s waveform.

Figure 6. (color online) ABR hearing threshold shift at frequencies of 0.5, 1, 2, 4, and 8 kHz obtained from 13 animal ears after exposures to blast waves.

Figure 7. (color online) Comparison of normalized energy flux over 10 frequency bands from

below 125 Hz to above 16 kHz between the waveforms recorded in the open and shielded groups of chinchillas.

Figure 8. (color online) FE model-derived distributions of the equivalent (von Mises) stress in the TM (A) and the displacement of the TM (B) in the open case at the time when the maximum stress was reached. The recorded pressure waveform is listed in Fig. 4B. The stress and displacement levels are shown by color cord.

Figure 9. (color online) FE model-derived distributions of the equivalent stress in the TM (A) and the displacement of the TM (B) in the shielded case at the time when the maximum stress was reached. The recorded pressure waveform is listed in Fig. 5B. The stress and displacement levels are shown by color cord.

Figure 10. (color online) Plots of FE model-derived stress increase with the peak-to-peak pressure loading in open and shielded cases. The red line with symbols was obtained from Fig. 8 in open case and the blue line with symbols obtained from Fig. 9.

REFERENCES

Fausti, S.A., Wilmington, D.J., Gallun, F.J., Myers, P.J., Henry, J.A, 2009. Auditory and vestibular dysfunction associated with blast-related traumatic brain injury. J Rehabil Res Dev, 46(6): 797-810.

Garth, R.J. Blast injury of the auditory system: a review of the mechanisms and pathology, 1994. The Journal of laryngology and otology, 108(11): 925-929.

Gondusky, J.S., Reiter, M.P, 2005. Protecting military convoys in Iraq: an examination of battle injuries sustained by a mechanized battalion during Operation Iraqi Freedom II. Military Medicine, 170(6): 546-549.

Guan X, Gan RZ**.** Effect of middle ear fluid on sound transmission and auditory brainstem response in guinea pigs. Hear Res, Vol. 277: 96-106, 2011.

Hamernik, R.P., Keng, D., 1991a. Impulse noise: Some definitions, physical acoustics and other considerations. J. Acoust. Soc. Am. 90: 189-196.

Hamernik, R.P., Ahroon, W. A., Hsueh, K.D., 1991b. The energy spectrum of an impulse: Its relation to hearing loss. J. Acoust. Soc. Am. 90: 197-204.

Hamernik, R.P., Qiu, W., 2001. Energy-independent factors influencing noise-induced hearing loss in the chinchilla model, J. Acoust. Soc. Am. 110: 3163-3168.

Hawa, T., Gan, R.Z., 2014. Pressure distribution in a simplified human ear model for the high intensity sound transmission. J. Fluids Engineering, 136: 111108-1 to -6.

Heffner, R.S., Heffner, H.E., 1991. Behavioral hearing range of the chinchilla. Hearing Research, 52: 13-16.

Hirsch, F.G., 1966. Effects of overpressure on the air - a review. Technical progress report on contract DA-49-146-XZ-372 (Department of Defense).

Jensen, J.H., Bonding, P., 1993. Experimental Pressure Induced Rupture of the Tympanic Membrane in Man. Acta Otolaryngol (Stockh). 113: 62-67.

Jeselsohn, Y., Freeman, S., Segal, N., Sohmer, H, 2005. Quantitative experimental assessment of the factors contributing to hearing loss in serous otitis media. Otol Neurotol, 26: 1011-1015.

Karmy-Jones, R., Kissinger, D., Golocovsky, M., Jordan, M., Champion, H.R., 1994. Bomb-related injuries. Military Medicine, 159(7): 536-539.

Luo, H., Dai, C., Gan, R.Z., Lu, H., 2009. Measurement of Young's modulus of human tympanic membrane at high strain rates. J. Biomechanical Engineering, 131: 064501-1 to -8.

Mayorga, M.A., 1997. The pathology of primary blast overpressure injury. Toxicology 121(1):17-28.

Patterson, J.H., Jr., Hamernik, R.P., 1997. Blast overpressure induced structural and functional changes in the auditory system. Toxicology, 121(1): 29-40.

Petrova, P., Freeman, S., Sohmer, H., 2006. The effects of positive and negative middle ear pressures on auditory threshold. Otol Neurotol, 27: 734-738.

Qin, Z., Wood, M., Rosowski, J.J., 2010. Measurement of conductive hearing loss in mice. Hear Res, 263: 93-103.

Richmond, D.R., Yelverton, J.T., Fletcher, E.R., Phillips, Y.Y., 1989. Physical correlates of eardrum rupture. Ann Otol Rhinol Laryngol, 98: 35-41.

Wang, X., Gan, R.Z., 2015. 3D finite element model of the chinchilla ear for characterizing middle ear functions. Biomechanics and Modeling in Mechanobiology (Under Review).

Young, R.W., 1970. On the energy transported with a sound pulse. J. Acoust. Soc. Am. 47: 441-442.

List of Abbreviation

ABR	Auditory Brainstem Response
AML	Anterior Malleal Ligament
EA	Energy Absorbance
FE	Finite Element
FSI	Fluid-Structure Interaction
PIL	Posterior Incudal Ligament
PST	Posterior Stapedial Tendon
SAL	Stapedial Annual Ligament
S.D.	Standard Deviation
TM	Tympanic Membrane
TMA	Tympanic Membrane Annulus
TTT	Tensor Tympani Tendon

Appendix

Table A1. Mechanical properties of middle ear soft tissues of chinchilla ear (Wang and Gan, 2015)

Structure	Parameters
Tympanic membrane	
Elastic modulus (MPa):	
Pars tensa	200
Pars flaccida	15
Density (kg/m^3)	1100
Damping coefficient	1.00×10^{-4}
Manubrium	
Elastic modulus (MPa)	800
Density (kg/m^3)	1200
Damping coefficient	7.5×10^{-5}
Incudomalleolar (IS) joint	
Elastic modulus (MPa)	6
Density (kg/m^3)	1000
Damping coefficient	7.5×10^{-5}
Stapedial annular ligament (SAL)	
Elastic modulus (MPa)	0.1
Density (kg/m^3)	1000
Damping coefficient	7.5×10^{-5}
Anterior malleal ligament (AML)	
Elastic modulus (MPa)	3.2
Density (kg/m^3)	1000
Damping coefficient	1.0×10^{-4}
Posterior incudal ligament (PIL)	
Elastic modulus (MPa)	2.5
Density (kg/m^3)	1000
Damping coefficient	7.5×10^{-4}
Posterior stapedial tendon (PST)	
Elastic modulus (MPa)	2.0
Density (kg/m^3)	1000
Damping coefficient	7.5×10^{-5}
Tensor tympani tendon (TTT)	
Elastic modulus (MPa)	2.0
Density (kg/m^3)	1000
Damping coefficient	7.5×10^{-5}
Malleus-incus complex	
Elastic modulus (GPa)	14.1
Density (kg/m^3)	2000
Mass (mg)	12.05
Damping coefficient	1.5×10^{-4}
Stapes	
Elastic modulus (GPa)	14.1
Density (kg/m^3)	1300
Mass (mg)	0.55
Damping coefficient	1.0×10^{-4}

24

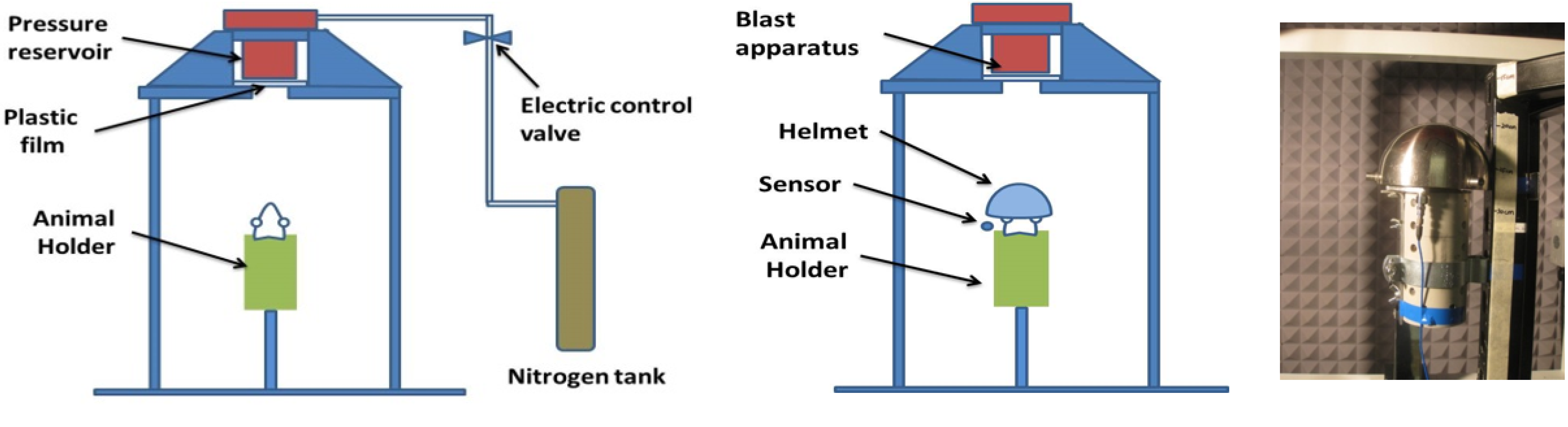
Pressure
reservoir
Plastic
film
Electric control
valve
Animal
Holder
Nitrogen tank
Blast
apparatus
Helmet
Sensor
Animal
Holder

(A) (B) (C)

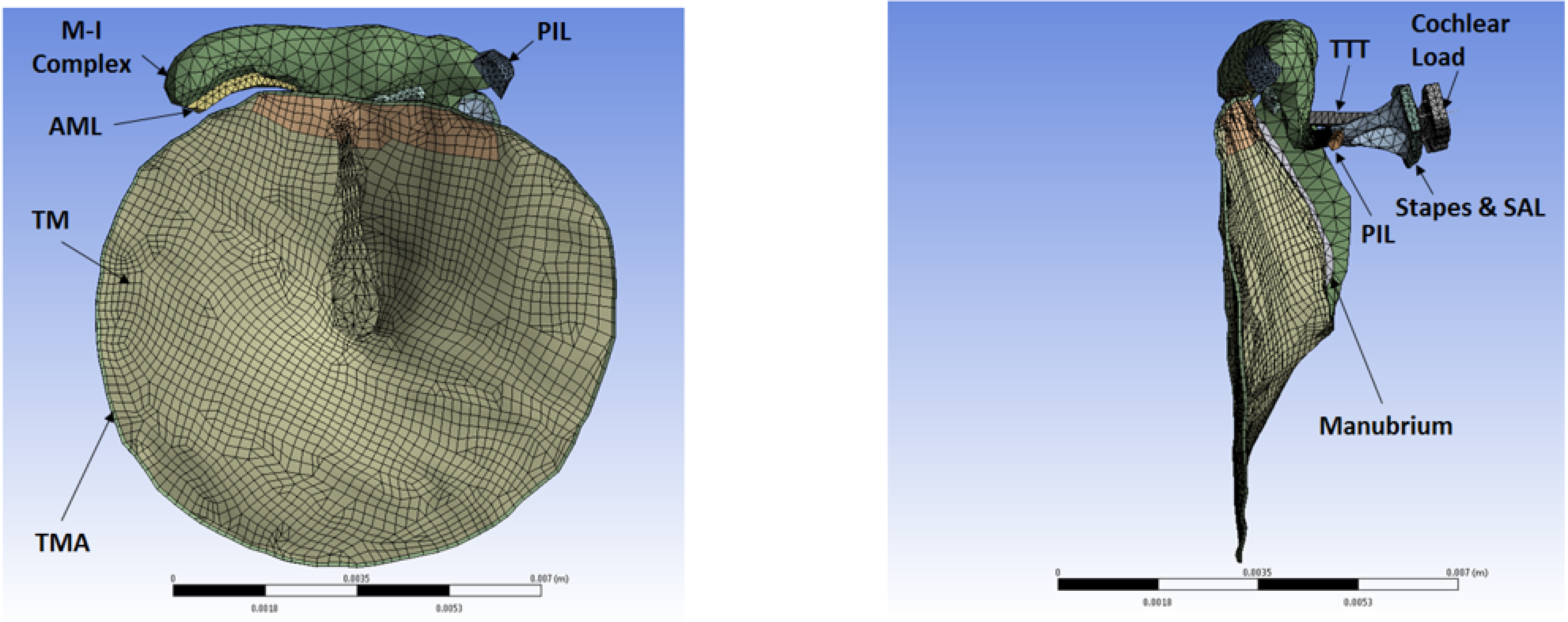
M-I Complex
PIL
AML
TM
TMA
0
0.0035
0.007 (m)
0.0018
0.0053
TTT
Cochlear Load
Stapes & SAL
PIL
Manubrium
0
0.0035
0.007 (m)
0.0018
0.0053

(A) (B)

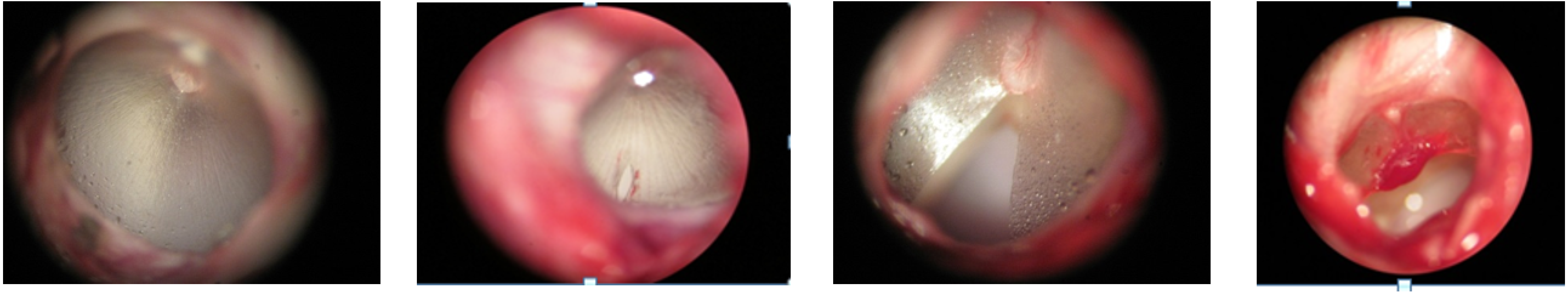

(A) (B) (C) (D)

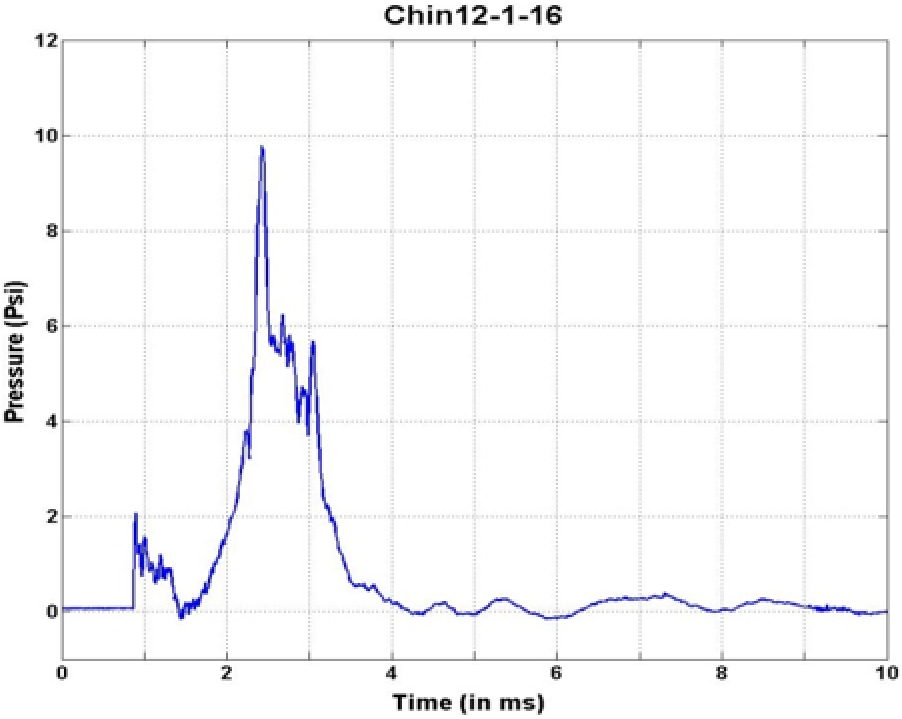
Chin12-1-16
Pressure (Psi)
Time (in ms)

(A)

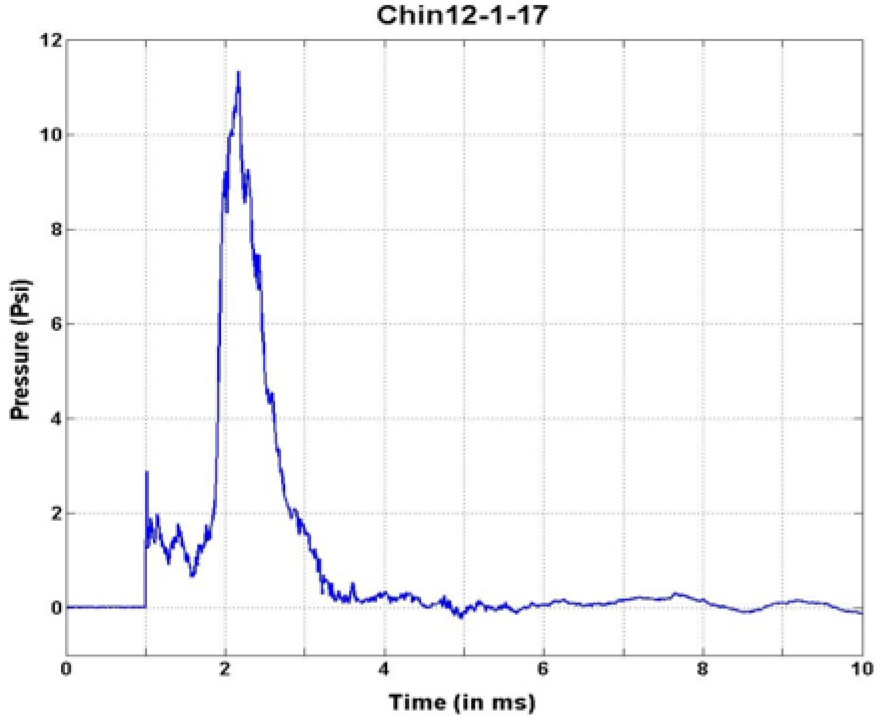
Chin12-1-17
Pressure (Psi)
Time (in ms)

(B)

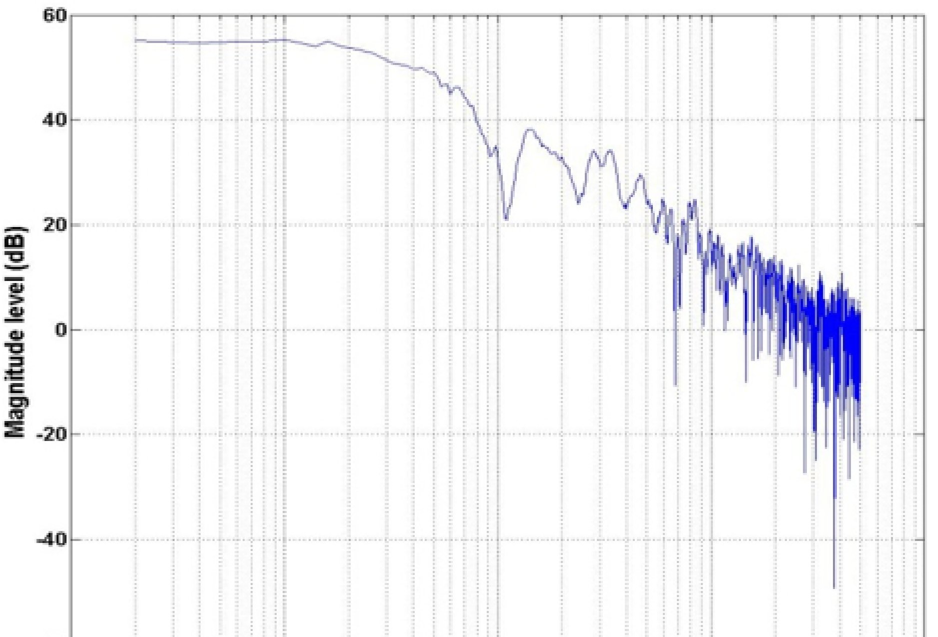
Magnitude level (dB)
Frequency in KHz

(C)

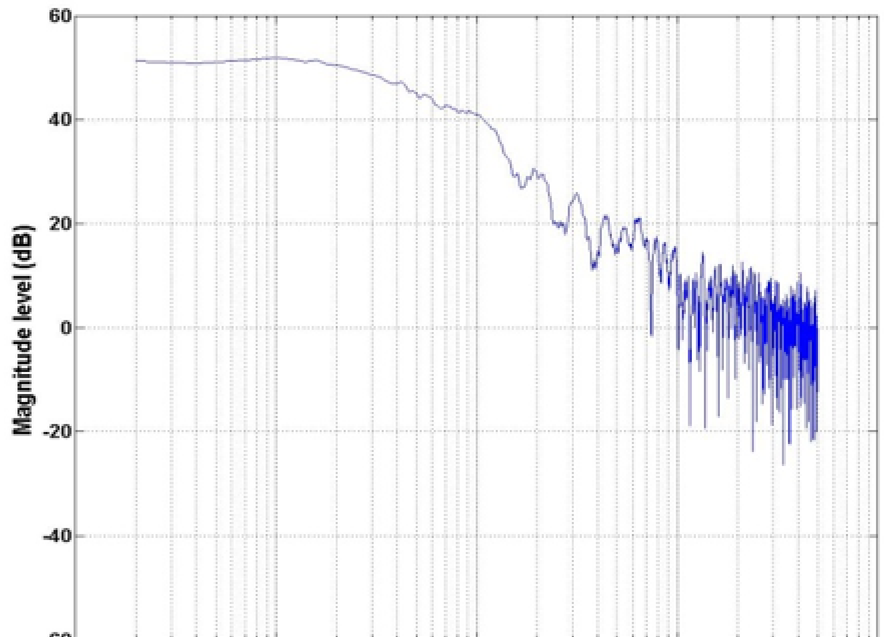
Magnitude level (dB)
Frequency in KHz

(D)

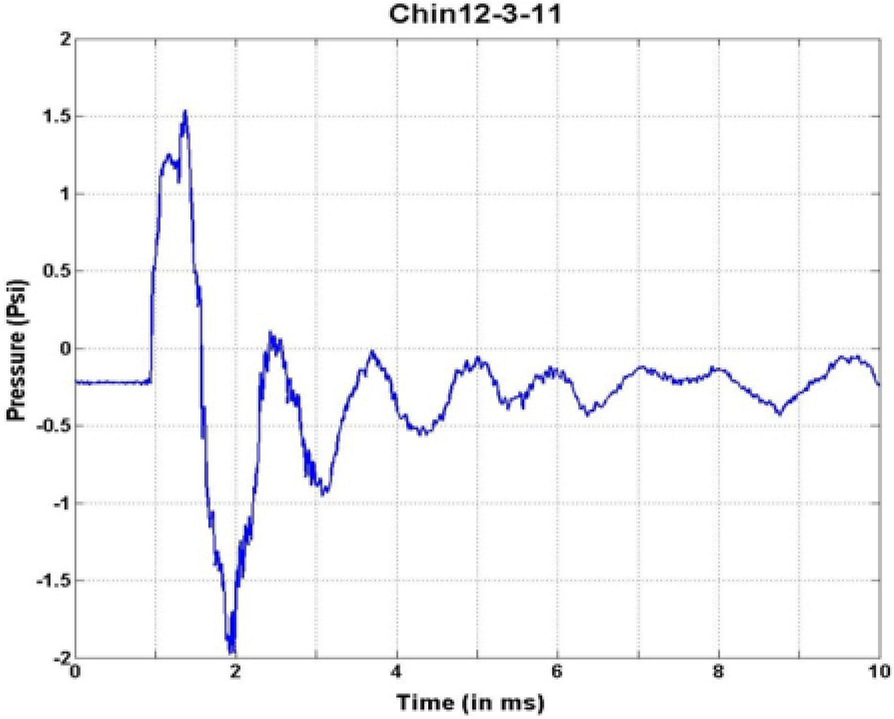
Chin12-3-11
Pressure (Psi)
Time (in ms)

(A)

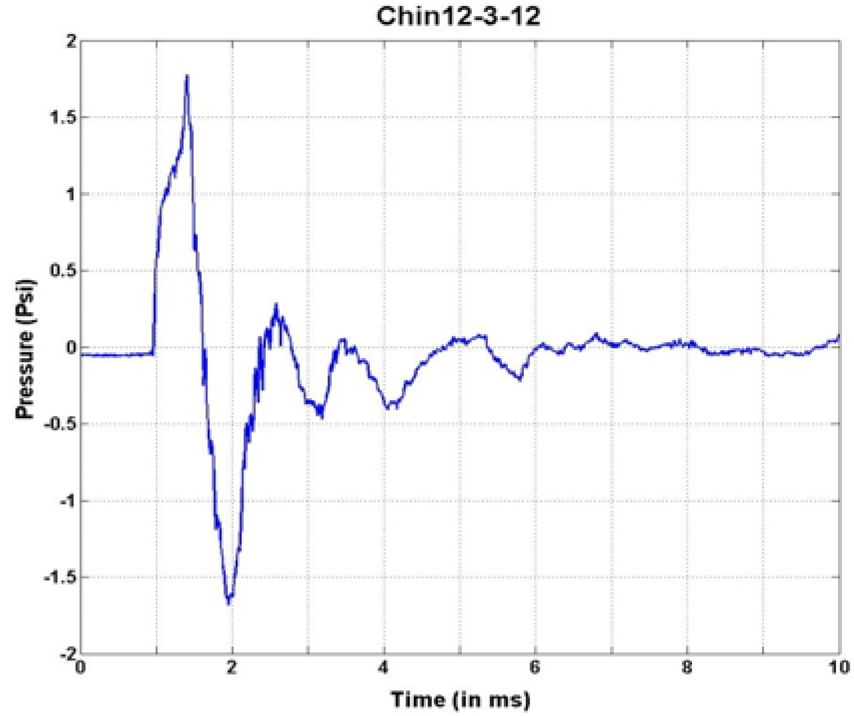
Chin12-3-12
Pressure (Psi)
Time (in ms)

(B)

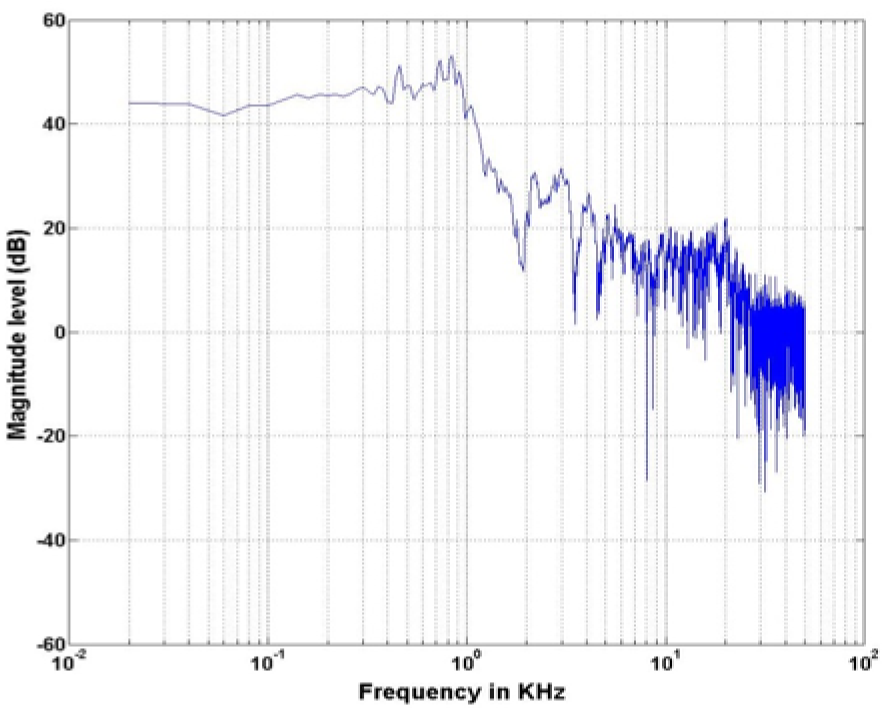
Magnitude level (dB)
Frequency in KHz

(C)

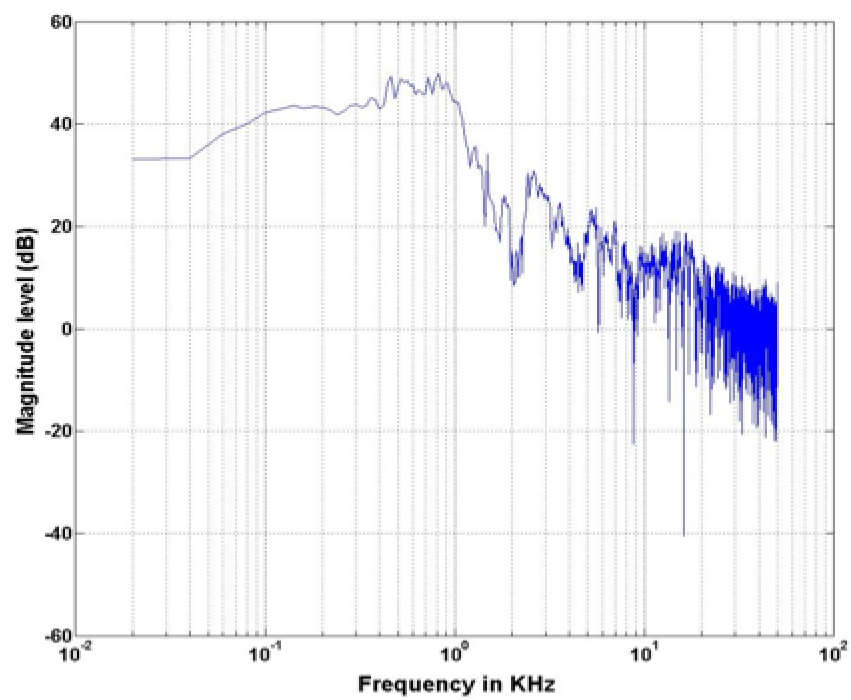
Magnitude level (dB)
Frequency in KHz

(D)

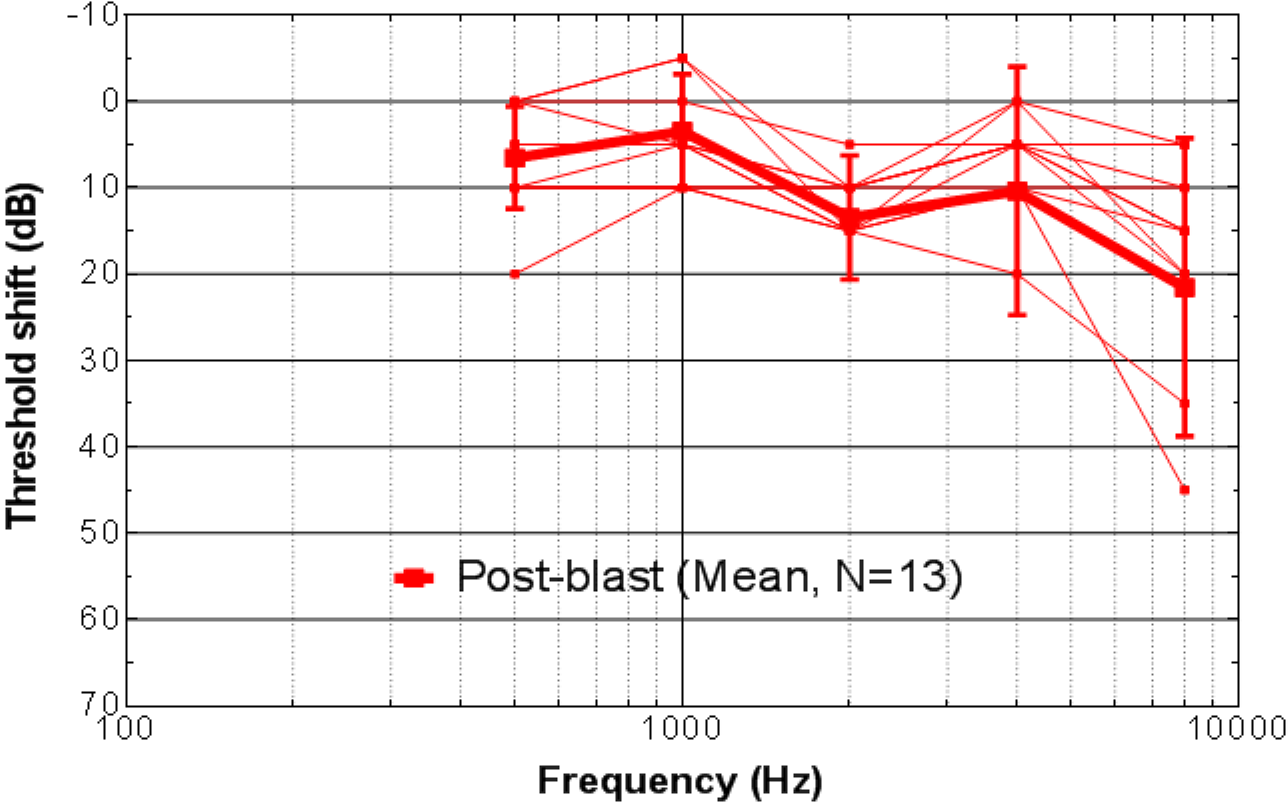
Threshold shift (dB)
-10
0
10
20
30
40
50
60
70
100
1000
10000
Frequency (Hz)
Post-blast (Mean, N=13)

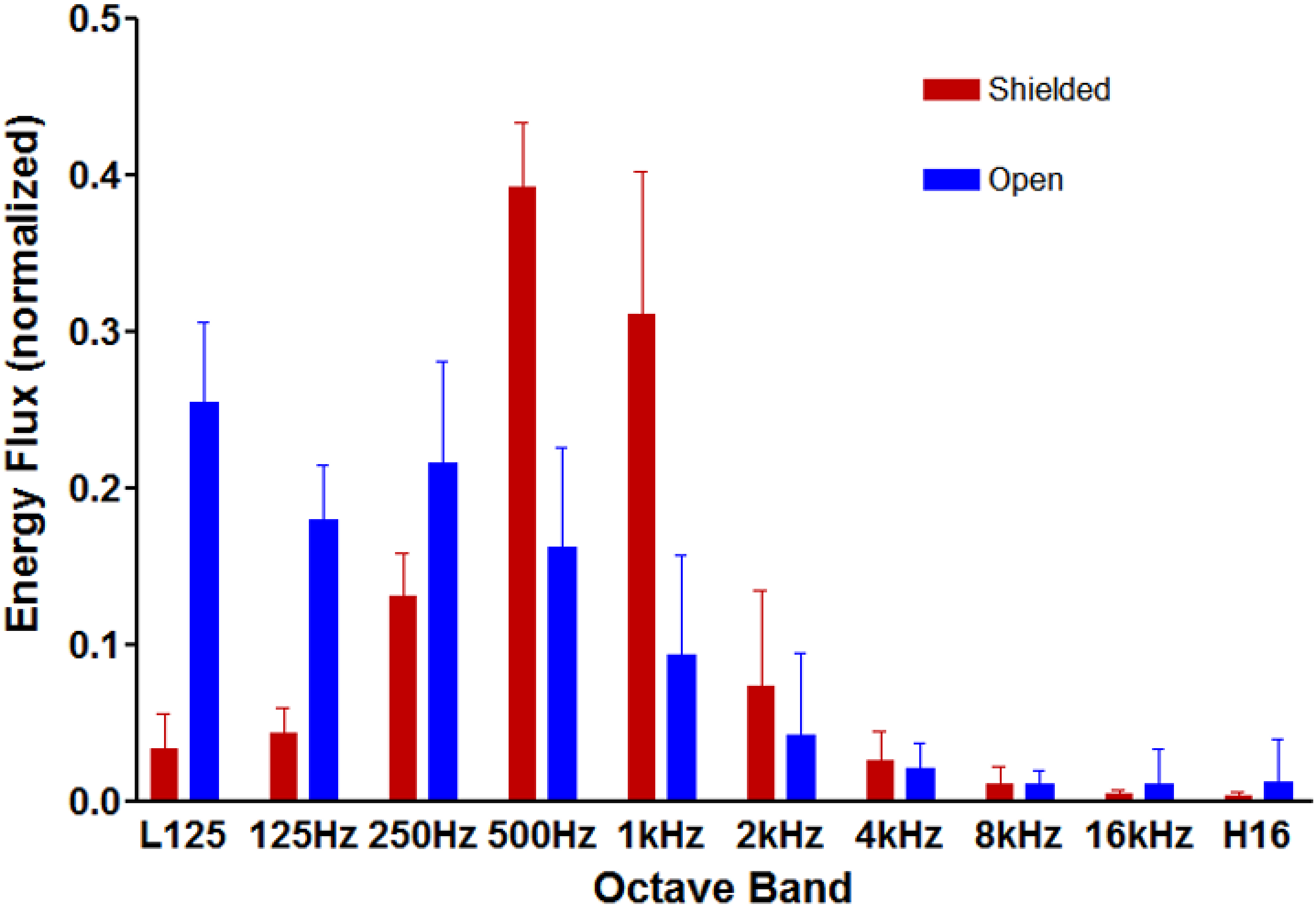

Energy Flux (normalized)
0.5
0.4
0.3
0.2
0.1
0.0
Shielded
Open
L125
125Hz
250Hz
500Hz
1kHz
2kHz
4kHz
8kHz
16kHz
H16
Octave Band

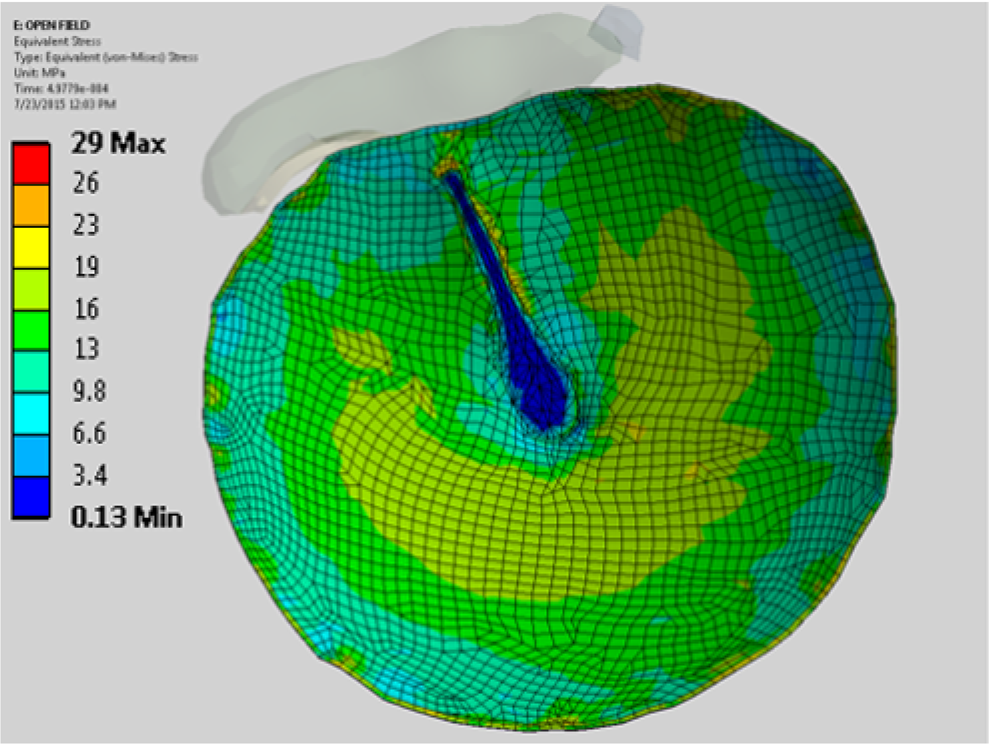
E: OPEN FIELD
Equivalent Stress
Type: Equivalent (von-Mises) Stress
Unit: MPa
29 Max
26
23
19
16
13
9.8
6.6
3.4
0.13 Min

(A)

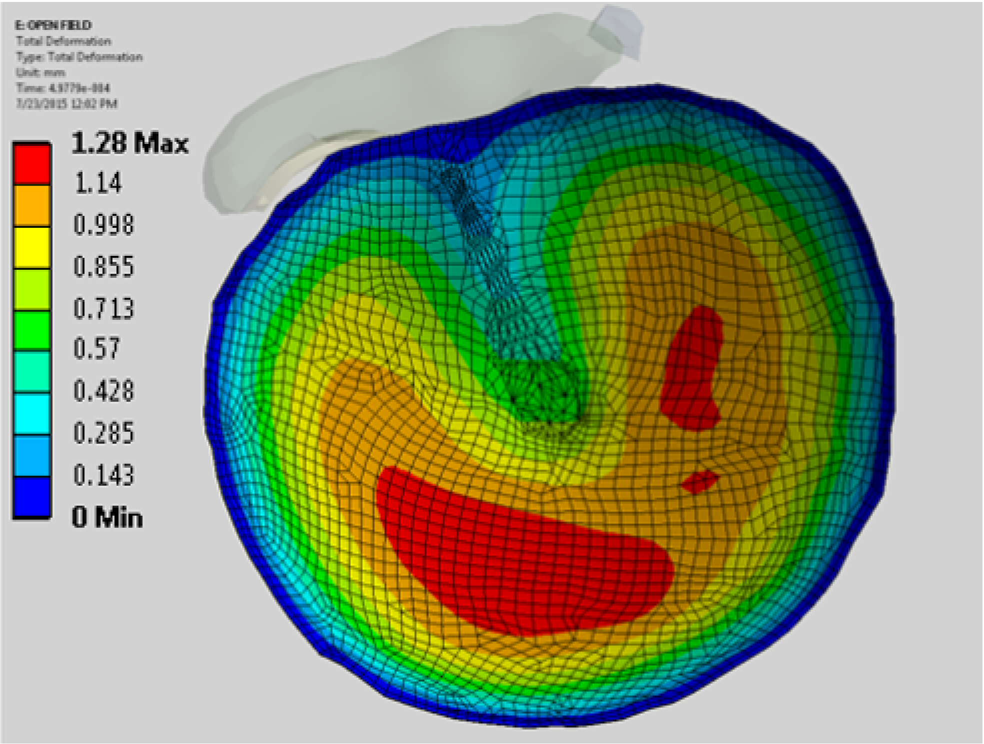
E: OPEN FIELD
Total Deformation
Type: Total Deformation
Unit: mm
1.28 Max
1.14
0.998
0.855
0.713
0.57
0.428
0.285
0.143
0 Min

(B)

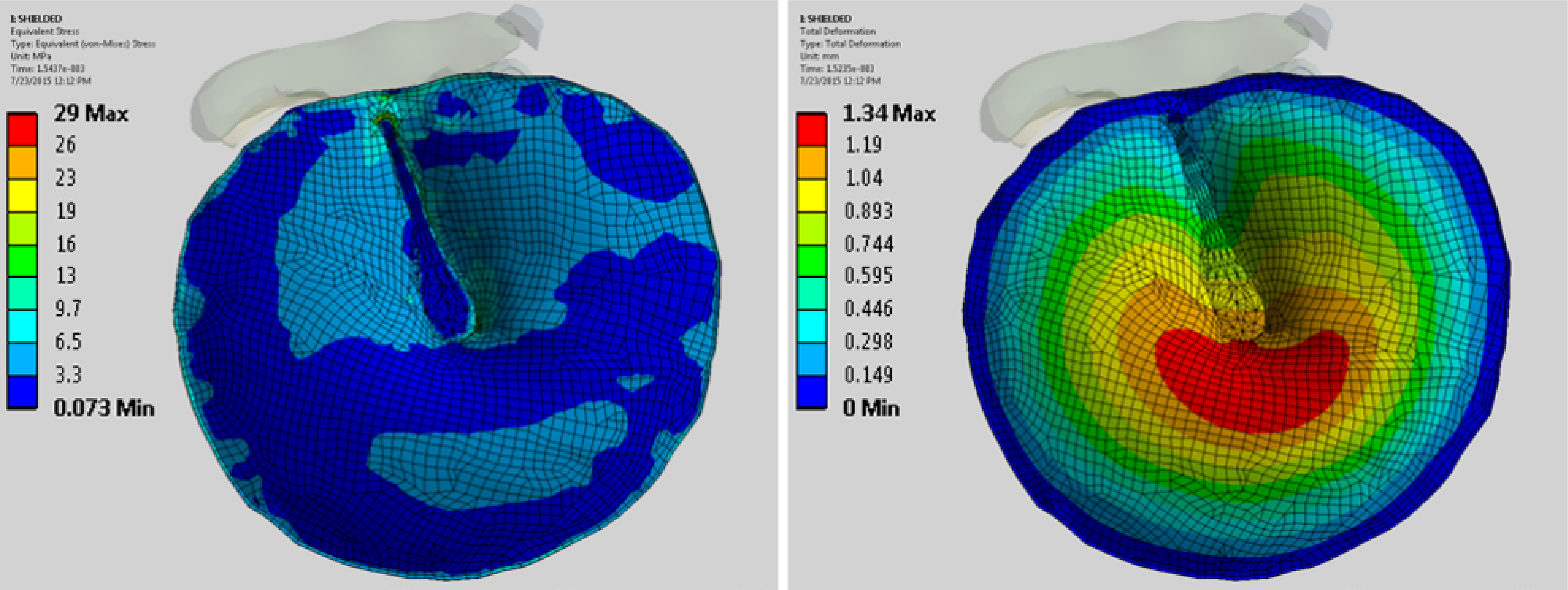
SHIELDED
Equivalent Stress
Type: Equivalent (von-Mises) Stress
Unit: MPa
29 Max
26
23
19
16
13
9.7
6.5
3.3
0.073 Min
SHIELDED
Total Deformation
Type: Total Deformation
Unit: mm
1.34 Max
1.19
1.04
0.893
0.744
0.595
0.446
0.298
0.149
0 Min

(A) (B)

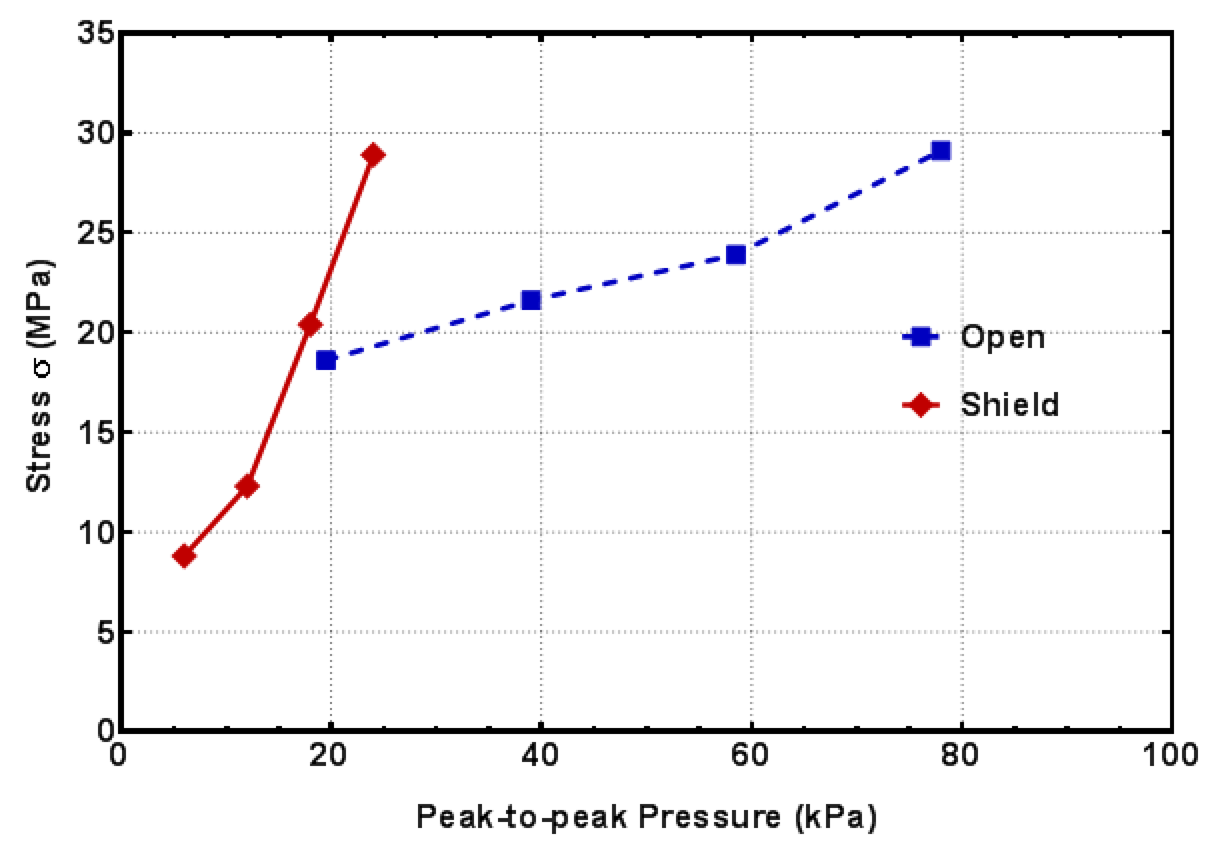

Stress σ (MPa)
Peak-to-peak Pressure (kPa)
Open
Shield
0
5
10
15
20
25
30
35
0
20
40
60
80
100

Animal	chin-1	chin-2	chin-3	chin-4	chin-5	chin-6	chin-7	chin-8	chin-9	Mean±S.D.
Threshold (Psi)	10.7	6.9	9.8	11.3	10.2	9.8	9.1	9.0	5.5	9.1±1.7

Table 1. List of TM rupture thresholds measured from a group of chinchillas tested in open field.

Table 2. List of TM rupture thresholds measured from a group of chinchillas tested with a shield or helmet.

Animal	chin-1s	chin-2s	chin-3s	chin-4s	chin-5s	chin-6s	chin-7s	chin-8s	chin-9s	Mean±S.D.
Threshold (Psi)	4.1	4.9	3.0	2.8	3.6	3.5	3.4	2.8	2.7	3.4±0.68

Table 3. Octave-band energy flux (J/m^2) (normalized) for the open and shielded groups.

Octave band CF(kHz)	Open		Shielded	
	Mean	±S.D.	Mean	±S.D.
<0.125	0.2557	0.0512	0.0343	0.0225
0.125	0.1797	0.0356	0.0444	0.0157
0.25	0.2159	0.0653	0.1310	0.0285
0.5	0.1628	0.0631	0.3922	0.0417
1.0	0.0935	0.0643	0.3118	0.0914
2.0	0.0421	0.0531	0.0737	0.0615
4.0	0.0211	0.0162	0.0270	0.0177
8.0	0.0113	0.0084	0.0114	0.0109
16.0	0.0121	0.0215	0.0051	0.0019
>16.0	0.0125	0.0278	0.0035	0.0024
Total	***1.0066***		***1.0344***	

Appendix B

Characterization of the nonlinear elastic behavior of chinchilla tympanic membrane using micro-fringe projection

Junfeng Liang[a], Huiyang Luo[a], Zachary Yokell[b], Don U. Nakmali[b], Rong Zhu Gan[b], and Hongbing Lu[a,*]

[a] Department of Mechanical Engineering, The University of Texas at Dallas, Richardson, TX 75080, USA

[b] School of Aerospace and Mechanical Engineering, University of Oklahoma, Norman, OK 73019, USA

ABSTRACT

The mechanical properties of an intact, full tympanic membrane (TM) inside bulla of a fresh chinchilla were measured under quasi-static pressure ranging from -1 kPa to 1 kPa applied on the TM lateral side. Images of the fringes projected onto the TM were captured by a digital camera connected to a surgical microscope and analyzed using a phase-shift method to reconstruct the surface topography. The relationship between the applied pressure and the resulting volume displacement was determined, and analyzed using a finite element model, considering a hyperelastic 2[nd]-order Ogden model. Through an inverse problem solving approach, the best-fit material parameters for the TM were determined to allow simulation results to agree with the experimental data. The average Young's modulus of the chinchilla TM from ten bullas was determined as 19 MPa up to a strain level of 25%.

Keywords: chinchilla; tympanic membrane; micro-fringe projection; static pressure; hyperelastic model.

List of the Abbreviations:
TM – tympanic membrane
LDV – laser Doppler vibrometery
FEM – finite element method
IACUC – Institutional Animal Care and Use Committee
PVC – polyvinyl chloride
XYZ – X-, Y- and Z-axis
CAD – computer-aid design
S – superior
P – posterior
I – inferior
A – anterior
U – umbo

1. INTRODUCTION

Eardrum or tympanic membrane (TM) separates the middle ear from the external ear, which is the key component

*Corresponding author. Tel: (972)883-4647; (972)883-4655 (Fax). Email: hongbing.lu@utdallas.edu.

to transmit sound pressure to ossicular chains in the middle ear, and finally into the cochlea. The function of the TM can be affected by ambient air pressure, which changes widely from a few Pascal (Pa) to a few kPa in daily life. In some extreme cases, for instance, under the blast wave in battlefield, the overpressure can be as high as 100 kPa, which could cause permanent damage to the TM (Ritenour et al., 2008). As TM is deformed under different ambient pressures, the transmission of sound energy across the middle ear can be significantly altered (Dirckx et al., 1991; Volandri et al., 2011; Ghadarghadar, et al., 2013; Thornton, et al., 2013; Greff, et al., 2014a, 2014b; Rosowski, et al., 2014). In order to understand the effect of pressure on sound transmission, the mechanical responses of TM have been investigated under various static pressures. The deformation of TM, induced by either negative or positive pressure in middle ear, was measured using shadow moiré technique on human temporal bones (Dirckx, et al., 1991). The TM vibration at different middle-ear pressures was measured on gerbil ears (Lee et al., 2001; Rosowski et al., 2002), where the alteration of acoustic stiffness and impedance by static pressures were observed. The stiffening of TM under the repeat pressure loading from habitual sniffing was investigated on gerbil using shadow moiré (von Unge, et al., 2009).

In addition to experimental investigations, numerical analysis using finite element methods (FEM) has been conducted to study sound transmission in middle ear under various static pressures. The effect of geometrical nonlinearity was reported on movement of cat eardrum under static pressure on TM (Ladak et al., 2006). The middle ear transfer function was also analyzed under various static pressures on human middle ear (Wang et al., 2007). It is noted that, the fidelity of the simulation results depends, to a large extent, on the accuracy of the mechanical properties of TM, as a function of pressure.

The mechanical properties of TM have been measured using numerous experimental techniques. The viscoelastic properties of human TM was measured under tension force using a dynamic mechanic analysis system (Cheng et al., 2007) and acoustic pressure using a laser Doppler vibrometery (LDV) system (Gan et al., 2010; Zhang et al., 2010). A miniature split Hopkinson tension bar was used to measure the dynamic properties of human TM under high strain rates (Luo et al., 2009a, 2009b). Another method is nanoindentation, it has been used to measure the mechanical properties of different quadrants of TM. The linear viscoelastic properties of TM were reported using nanoindentation (Huang et al., 2008). The method was also used to measure both in-plane and out-of-plane mechanical properties at diffjerent locations of TM (Daphalapurkar et al., 2009). The Young;s modulus was measured to be around 20 MPa by nano/micro-indentation (Anernour, et al , 2010, 2012a, 2012b; Hesabgar, et al., 2010; Soons, et al., 2010; Salamarti, 2012). In all these methods, strip or cut TM specimens were used. This approach causes the collagen fibers in the radial or circumferential directions in pars tensa to shrink (O'Connor et al., 2008), and alter the physiological condition of TM, leading potentially to erroneous results. To circumvent this problem, it is necessary to employ a new method to measure mechanical properties for the full, intact TM, which is the focus of this paper.

Full-field measurement methods have been used in the last several years, to measure mechanical responses of TM. Using LDV and stroboscopic holography, deformation of human TM were measured with acoustic loading, and viscoelastic properties were determined with the assistance of combing FEM simulated umbo displacement obtained in experiment (De Greef et al., 2014). Another full-field method to probe mechanical properties, was developed to measure the TM elastic properties (Aernouts et al., 2010; Buytaert et al., 2009) using geometric moiré and indentation loading. The geometric moiré was used to determine the surface topography while the indentation was applied; the mechanical response of the TM sample was simulated by finite element analysis to determine the elastic properties and the viscoelastic properties of the TM under low frequency (Aernouts et al., 2012a; Aernouts et al., 2012b; Aernouts et al., 2012c) using an inverse problem solving scheme. Both methods do not directly measure TM properties under air pressure which is a situation different from the air pressure loading applied to the entire TM under normal hearing, or blast wave condition. In addition, for the latter method, the contact nature and the localization of force applied on a small region, could impose challenges to maintain the indenter positioning under increase load. There is also the issue of convergence in the contact mechanics problem. An alternative computer-based method was developed, in which pressure was used instead of indentation (Ghadarghadar et al., 2013). In this method, the Young's modulus of TM was estimated by optimizing the difference in displacements over the entire TM calculated from model and that measured from experiment. The replacement of indentation loading with pressure loading simplified the experimental setup. However, due to the complicated structure of TM, the optimized computational displacement did not agree well with the experimental result. Meanwhile, the nonlinearity of the mechanical behavior of TM under different pressures has not been considered.

In this paper, we provide a new non-invasive full-field method on the mechanical properties of TM under static pressure. In this paper pressure was applied on TM, and micro-fringe projection was introduced to measure the resulting deformation. A combined experimental and numerical investigation is used to solve the inverse problem, to determine the mechanical properties of chinchilla TM. The TM inside a bulla is pressurized while its topography is determined by a full-field micro-fringe projection technique. Volumetric displacement is then calculated from the topography. FEM with nonlinear material model is applied to model the topography of TM under pressure, to provide the simulated relationship between pressure and volume displacement that is consistent with experiment. The nonlinear mechanical properties of TM under different static pressure are thus determined.

2. METHOD

2.1. Micro-fringe projection technique

A micro-fringe projection technique is used to determine the deformed surface topography of the TM under a prescribed static pressure. In fringe projection, a grating (or fringe) is projected onto an object and the image of the projected fringe on the surface of the object is acquired by a digital camera. Another image of fringe projected onto a reference plane under the same setup is also acquired. The image of the projected fringe on the object is subsequently digitally superimposed with the image of projected fringe on the reference plane to generate interferometry (Ortiz et al., 2003; Ortiz et al., 2005). Virtual shifting is conducted by utilizing five phase-shifted images of the original image to calculate the phase difference between reference plane and the object from the interferometry map.

The inverse tangent function outputs phase angle within the interval $[-\pi, \pi]$ with 2π discontinuity at the end of the period. In order to determine the surface profile from the direct output, phase angle has to be unwrapped. A quality bins algorithm was used to unwrap the phase map for surface profile reconstruction (Ghiglia et al., 1998). In the case where the projection is telecentric, the out-of-plane position Z is determined from the phase angle difference $\Delta\Phi$ for any point on the object surface:

$$Z = \frac{ph}{d}\frac{\Delta\Phi}{2\pi} \tag{1}$$

where h is the distance between camera and object, and d is the distance between camera and light source, shown schematically in Figure 1(a). In the actual case, it is very difficult to accurately measure these parameters directly from the apparatus. A calibration procedure is thus used to determine the ratio between h and d in Eqn () (Ortiz et al., 2003). A cone with known dimensions that approximately matches the features (radius and depth) of the interest in the specimen was used for calibration. By comparing the phase map with the known geometry, the ratio of h to d was determined.

2.1. Experimental setup

Figure 1(b) shows the schematic diagram of the experimental setup. The chinchilla bulla is placed on a gimbal holder attached to a temporal bone bowl, which allows the direction of the TM surface to be adjusted for micro-fringe projection as well as for observation by a camera. A set of X-, Y- and Z- (*XYZ*) stage was used to hold the temporal bone bowl, to position the TM within the field of the projected fringes and field of view of the camera. A micro-fringe projector, including a set of lenses, grating, and fiber optic light source was used to project fringes onto the TM in the bulla. The projector consisted of a 100 W fiber optic lamp, two condenser lenses (Edmund Optical Sci. Co. #89-038), a grating and an objective lens (Fujinon Photo Optical Co. 611374). The focal length of the objective lens was adjustable so that an in-focus pattern of equidistant pitch fringes was projected onto the reference plane and the object. The grating used had a square wave transmission profile, namely Ronchi rulings (Edmund Optical Sci. Co. #58-777) with pitch density of 20 cycle/mm. A CCD digital camera (Nikon D7000, 4928X3264 pixels) was attached to a beam splitter on a surgical microscope (Carl Zeiss OPMI-1) with an objective lens of 250 mm. The microscope head was connected to a finely adjustable arm mounted on a movable stand, which allowed optical axis of the microscope to be remained perpendicular to the sample holder plane. The projection lens of micro-fringe projector was located about 88 mm away from the microscope objective lens; an angle of ~19° was formed between the axis of the microscope-camera assembly and axis of the projector. The combination of a finer grating and a smaller angle generally produces higher sensitivity than a larger angle and a coarser grating. Meanwhile, the distance between the instrument and the object should be at least one order of magnitude larger than the height of the object (von Unge et al., 1993). In our case, the height of chinchilla TM was about 2 mm, which was much smaller than the working distance (250 mm) of the microscope. Therefore, the telecentric condition was satisfied and valid.

A pressure monitor system was used to load the specimen with either positive or negative static pressure. The system consists of two three-way stopcocks, a 20 mL syringe and a water manometer with a resolution of 2.5 mm water bar (Dwyer Instruments, Inc. Series 1235). A three-way stop-cock serves as a valve to control the pressure applied on the specimen; it allows releasing pressure for the whole system, applying pressure to the specimen, and locking up the pressure in the specimen. Another three-way stopcock, serving as pressure direction control, was utilized to switch between positive pressure and negative pressure applied on the specimen.

2.2. Sample preparation

Ten TMs of adult chinchillas weighting between 535 g to 855 g, without middle ear disease, were used in this study. Chinchilla is chosen because the diameter and the shape of their TM are close to human. The study protocol was approved by the Institutional Animal Care and Use Committee (IACUC) of the University of Oklahoma and met the guidelines of the National Institutes of Health. After the examination with otoscope, a chinchilla was sacrificed with ketamine (100 mg/kg im) and xylazine (10 mg/kg im) injected directly in the heart. Intact temporal bones or bullas were harvested from the skulls 10 minutes *post mortem*. The bulla wall was opened widely from the middle ear side and both cochlea and stapes with the tensor tympani muscle were removed until the medial side of TM was fully exposed (Figure (a)). In order to maintain the geometry of the TM and simplify the boundary condition for modeling, the malleus-incus complex was immobilized by applying a droplet of gel type superglue (Superglue, Co. Find the Right Glue, Fast™) between the incus section and the petrous wall behind. A polyvinyl chloride (PVC) tubing with 3/16 inches inner diameter, 1/4 inches outer diameter, and about 3 inches long, was inserted into the ear canal and hermetically fixed on the bulla by applying two-part epoxy (Devcon and 5 Minute, Illinois Tool Works Inc.) at the entrance of ear canal. The two-part epoxy was mixed and cured for 2 minutes before applied on the bulla to ensure that it was viscous and would not flow into the middle ear. The outer end of the tubing was then connected to the pressure monitor system for applying static pressure loading on the TM from lateral side (Figure (b)). The total sample preparation for each bulla in this section took about 45 minutes. In order to protect the TM from desiccation, during the process of opening the bulla, a droplet of saline solution was applied on the TM every 5 minutes. Also, during the curing period of the two-part epoxy, a small piece of Kimwipes paper saturated with saline solution was used to cover the TM.

Similar to shadow moiré, fringe projection requires the object to have diffusive reflecting surface. Therefore the medial side of TM was coated with a thin layer of titanium oxide in saline solution (100 mg/ml) to provide good reflection. Titanium oxide was chosen because it is a typical material used in cosmetics and the thin layer of the coating is not anticipated to affect the mechanical response of the TM (Dirckx et al., 1997).

2.3. Measurement procedure

After the bulla specimen was prepared, it was mounted on the gimbal sample holder. The bulla was first secured with molding clay to coarsely adjust the position of the bulla so that TM faced the microscope; and then fixed with screwed arms of the holder and finely adjusted the angle to give a full view of the TM without any shadow. The aforementioned PVC tubing was connected to the first three-way stopcock in the pressure monitoring system, and the stopcock was swift to change-pressure mode. Pressure was then applied to the bulla manually through the syringe in the pressure monitoring system. As TM, like other soft tissue, is a viscoelastic material (Fung, 1993; Ladak et al., 2004), preconditioning must be carried out to allow the specimen to reach a steady state. For our case, each bulla was preconditioned by applying small pressure with magnitude less than 100 Pa by five cycles prior to test. A positive pressure was induced by pumping compressed air into bulla from ear canal; as such, the pressure on the medial side of the TM was lower than the pressure applied on the lateral side of the TM. A negative pressure was induced by inducing a vacuum in the ear canal; in such a case the pressure on the medial side of the TM was higher than the pressure applied on the lateral side. For each cycle in preconditioning, a negative pressure was applied first to the bulla, and then the pressure was increased to a positive pressure, and finally the pressure was released back to zero. Both positive and negative pressures were applied to the bulla for measurement of the response of the TM to pressure to determine mechanical response of the TM. Pressure was applied with a magnitude between 0 to 1.0 kPa with a step of 0.125 kPa inside the bulla with stopcock set to lock-up mode, meanwhile a constant pressure was maintained at each step. The entire measurement takes about 2 minutes for each sample therefore no special care was needed to moisturize the TM. Since chinchilla TM is thin and fragile, some of the TMs ruptured during the process of loading. Therefore the pressure range of these samples was smaller. Meanwhile, it is difficult to collect entire loading and unloading curves for all the specimen. In this work, only loading data are recorded and used. In fact, the preconditioning has significantly reduce the hysteresis, which can be seen in figure 3. The detail of analysis will be given in the discussion section.

For each state of pressure, including the zero-pressure state, image was acquired by a digital camera attached to the microscope. For each image, reconstruction of TM surface was conducted using the method described in

Section 2.1. The reconstructed TM surface profiles were then used to calculate the volume displacement based on the surface typology under pressure and the surface typology under zero-pressure state. A FEM model was built using the surface typology of the TM determined at zero-pressure state. For each specimen, an individualized FEM model was used and the volume displacement under static pressure was calculated. Simulations were conducted by selecting hyperelastic model parameters in material constitutive law until the volume displacement of the calculation model matched well with the corresponding experimental volume displacement.

2.4. Finite element simulations

Finite element analysis software, ANSYS-15 was used for FEM simulation of chinchilla TM under quasi-static pressure. The surface topography under zero-pressure state, reconstructed from micro-fringe projection, was converted to a three-dimensional model using SolidWorks 2013. Since the TM thickness is small compared with its major or minor diameters, TM was modeled as a shell with a thickness of 10 μm. The CAD model was then converted to a shell model for simulation in ANSYS. The boundary and the location of malleus were determined by the optical image of the TM sample. Malleus was constructed using SolidWorks as a part of the TM assigned with properties of a bone (with 10 GPa Young's modulus, and 0.2 Poisson's ratio). The outer boundary (annulus tympanicus) of the TM was fixed for all degrees of freedom (no translations or rotations) and a uniform pressure in the range of 0 kPa to 1 kPa, was applied from the medial side (negative pressure) or lateral side (positive pressure), corresponding to pressures used in experiments.

Each meshed FEM model has nearly 10,000 4-node tetrahedral shell elements (shell181); the boundary determined from optical image as shown in Figure 2(a) was used in FEM simulation. Although practically, due to the continuation between epithelial layer of the TM and annulus, accurately determine the boundary location, especially for the pars flaccida, is very difficult. In our case, only volume displacement was used, the slight difference (less than 3%) in boundary location is not expected to change the volume displacement profoundly. Meanwhile, the area of pars flaccida is also very small comparing to pars tensa (Vrettakos, et al., 1988). Experimental data do not show any abruptly change of deformation in the neighborhood of pars flaccida area, therefore, only pars tensa was considered in both reconstruction and the FE modeling. The medial and posterior views of a meshed TM model are shown in Figure 3(a) and (b), respectively, without showing the boundary conditions and applied pressure. Figure 3(c) shows the medial-lateral views of TM surface topography with boundary conditions. The outer boundary (annulus tympanicus) of the TM was fixed for all degrees of freedom (no translations or rotations) and a uniform pressure in the range of -1 to 1 kp , was applied from the medial side (negative pressure) or lateral side (positive pressure), the same as the pressure used in experiments.

To simulate the pressure – volume deformation response observed in experiments, finite element analysis with the use of an appropriate constitutive model is conducted. Since TM is essentially a biomaterial in rubbery state, a hyperelastic model traditionally developed for materials in the rubbery state such as elastomers is used in this study, to describe the constitutive behavior of a chinchilla TM under pressure. The pressure-volume displacement response of TM shows behavior similar to an elastomer (Aerts et al., 2010), including stiffening after reaching a certain pressure, the Ogden model is used to describe the mechanical properties of TM for large deformation. The Ogden strain energy potential is given as:

$$U = \sum_{i=1}^{N} \frac{2\mu_i}{\alpha_i}\left(\lambda_1^{\alpha_i} + \lambda_2^{\alpha_i} + \lambda_3^{\alpha_i}\right), i = 1,2, \dots N \tag{2}$$

where N is the number of terms in the Ogden model; λ_j , (j=1, 2, 3) are the principle stretch ratio, μ_i and α_i are constants. In this study, N was taken as 2. In order to determine the model parameters μ_i and α_i, an inverse problem-solving scheme was used by allowing the FEM simulated TM volume displacement data to match the measured values under a given pressure. The procedures are described as follows.

(1) Give vector of initial values, p containing μ_i and α_i.

(2) Generate a FEM model for the TM, consistent with the geometry of the TM under zero-pressure state. The TM is assigned with hyperelastic parameters (Ogden model). The out-of-plane displacement (i.e., displacement perpendicular to the image plane of the camera), and height Z of each node was obtained.

(3) Interpolate nodal displacement obtained in Step 2 to the background grids with point density identical to the pixel density of images obtained in experiments using bilinear interpolation scheme.

(4) Calculate the volume displacement from the out-of-plane displacement of the background grid, and compare it with the experimental volume displacement data, which is calculated as:

$$\Delta V = \iint_{\Omega} [z(x,y) - z_0(x,y)]\mathrm{d}x\mathrm{d}y \tag{3}$$

where, $z(x,y)$ and $z_0(x,y)$ are the height profiles under finite pressure and zero pressure, respectively, Ω is the boundary of the annulus. Optimization of a cost function is used to estimate the Ogden parameters using ΔV at different pressure. The cost function is defined as:

$$f = \sum_{i=1}^{M} \Delta V_i^2 \tag{4}$$

where M is the number of pressure states

(5) Update p using a gradient descent algorithm, and repeat Steps (1) through (4) until $f < 0.5\ \mathrm{mm}^6$. The equation for gradient descent is given as:

$$p' = p - \gamma \nabla f(p) \tag{5}$$

Where γ is the learning rate, set to be 0.1, $\nabla f(p)$ is a vector of discrete form of gradient of f. where each element is the difference of the cost function f when one parameter in p change 0.1.

In this study, the initial parameters are set to be the parameters used for human (Chen, et al., 2007). A range of initial values in the neighborhood of this set of initial parameters has been tried and it was found that within this range, the results converges to the same answer.

3. RESULTS

3.1. Reconstruction of the TM surface under pressure

The TM surface topography under different pressures was obtained from the micro-fringe projection system. Figure 2(a) shows the TM image under projected micro-fringes before reconstruction of the surface. The four sections of TM, namely superior, posterior, inferior, anterior, and umbo, are shown and marked as "**S**", "**P**", "**I**", "**A**" and "**U**", respectively. Figure 2(b) shows the typical height color contours of TM under zero-pressure state from the reconstruction. Figure 2(c) and (d) show the *z*-displacement, U_3 contours under pressures. For illustration purpose, only the two extreme cases were shown here: TM under -1.0 kPa and 1.0 kPa pressure.

Under -1.0 kPa, the edge of TM close to inferior-posterior region has nearly zero displacement. Like other rodent, the manubrium of chinchilla is a thin bony edge, with thickness decreasing from about 1.0 mm at superior of annulus to roughly 0.1 mm at umbo. However, the region of low displacement is relatively large, which covers more than 1/3 of the TM area around the manubrium. Likewise, around the annulus ring, a ring of low displacement region with width about 1.0 mm can be also observed. The maximum displacement is found located at the ring-shape belt concentric with the annulus and about 1.5 mm from annulus ring covering posterior, inferior and anterior. This probably stems from the thickness distribution of the TM: it is thicker at location around the bony boundary and thinner at location away from the bony boundary (Gea et al., 2010). Similar displacement distribution is also seen at positive pressure of 1.0 kPa, elucidated in Figure 2(d). However, the region of low displacement in positive pressure case is small around manubrium. The displacement at location close to annulus smoothly increases to maxima at the location about 2.5 mm away from annulus and then gradually decreases to zero. Due to the complex cone-shape geometry of TM, TM under positive and negative exhibit different response.

3.2. Mechanical response of TM to various static pressures

Since uniaxial tensile test is the most commonly used test for TM measurement, it is convenient to estimating the uniaxial behavior of TM with the parameters in Ogden model. The uniaxial form of *N*-order Ogden model is given as (Aernouts et al., 2010; Wang et al., 2002)

$$T_U = \sum_{i=1}^{N} \frac{2\mu_i}{\alpha_i}\left(\lambda_U^{\alpha_i-1} - \lambda_U^{-0.5\alpha_i-1}\right), i = 1,2, \ldots N \qquad (6)$$

where T_U is the uniaxial stress; λ_U is the uniaxial stretch ratio, and $\lambda_U = 1 + \varepsilon_U$, with ε_U being the uniaxial strain.

Under uniaxial stretch, assuming incompressibility of the TM, the principal stretch ratios λ_i (i=1, 2, 3) are given as $\lambda_1 = \lambda_U, \lambda_2 = \lambda_3 = \lambda_U^{-\frac{1}{2}}$. Using Eqn (6), the pressure-volume displacement can be calculated from the z-displacement U_3 profile. Figure 4(a) shows the pressure as a function of volume displacement, plotted in terms of the curves from the testing of ten chinchilla TMs with intact immobilized malleus-incus complex attached. It is noted that, results from some TM have smaller range due to the rupture of TM in experiment. To distinguish the TM samples, markers were used at certain data points. The pressure-volume displacement curves exhibit strong nonlinearity. The increase stress with the increase of strain indicates the stiffening behavior of the chinchilla TM, and therefore the alternation of stiffness as pressure increases. This is likely due to the collagen fibers in the soft tissue. At the initial stage of the loading, collagen fibers are relaxed, showing a linear behavior. As the loading increases, the collagen fibers start to align in the load direction bear loads, to provide changing stiffness.

Due to the nearly conical geometry of TM, volume displacements are similar between negative and positive pressures but showing slightly asymmetry: deformation under positive pressure is smaller than deformation under negative pressure. The asymmetry of volume-displacement over pressures agrees with that observed from TMs of other mammals, such as gerbil (Gea et al., 2010), cat (Funnell et al., 1995), and human (Gaihede et al., 2007). Figure 4(b) shows a curve-fitting of the average pressure-volume displacement curve between FEM results and experimental data for ten TMs. Two extreme cases are also plotted, which are best case of fitting for one of the animals and worst case of fitting for another animal. The error is less than 10% between FEM and experimental data, indicating that the Ogden model is appropriate to describe the TM mechanical behavior. The model parameters are obtained with both positive and negative pressures. The dimensions of the TM and the material properties parameters for Ogden model of each TM are listed in Table 1.

3.3. Young's modulus of TM

The Young's modulus is defined as the slope in the linear region of stress-strain curve under small deformations. The slope of the stress-strain curve at any point is the tangent modulus. The Young's modulus and the tangent modulus are identical at the initial, linear portion of a stress-strain curve. In the case of hyperelastic material, the tangent modulus can be obtained by taking derivative of stress with respect to strain from Eqn (6), given as

$$\frac{dT_U}{d\varepsilon_U} = \sum_{i=1}^{2} \frac{2\mu_i}{\alpha_i} [(\alpha_i - 1)(1 + \varepsilon_U)^{\alpha_i - 2} + (0.5\alpha_i + 1)(1 + \varepsilon_U)^{-0.5\alpha_i - 2}] \tag{7}$$

With known material parameters, the Eqn (6) were plotted into Figure 5(a). The stress-strain curve of the chinchilla TM exhibits a strong non-linearity. The slope decreases when strain is smaller than 20%, and increases when strain is larger than 20%; then continues to ramps up. At 31% strain, which is the maximum strain on the TM determined by FEM model, the maximum stress reach 1.1 MPa. Figure 5(b) shows the tangent modulus as a function of strain for 10 chinchilla TMs. The average Young's modulus is plotted with results obtained from 10 bullas. At strain close to zero, the tangent modulus is 25 MPa. Then it decreases to 11 MPa at 31%. The average tangent modulus, at strains less than 25%, is chosen as the representative Young's modulus. Therefore, the average value of ~19 MPa is quoted as the Young's modulus.

4. DISSCUSSION

Mechanical properties of TM are difficult to measure due to its small size. The traditional measurement using strips cut from the intact TM induces not only damage to TM structure, but also difficulty to control the exact size and extension of the sample. For example, in tension test, the gauge length to width ratio is usually chosen as about 3 (Cheng et al., 2007), which is less than the standard value used in material tensile testing (typically 5) (ASTM standard, 2015). Meanwhile, it is challenging to clamp the soft tissue without inducing boundary effect. Aernout *et al.* proposed an indentation on the TM under the *in-situ* condition; that method avoids the cutting of the TM (Aernouts et al., 2012a; Aernouts et al., 2012b; Aernouts et al., 2010; Aernouts et al., 2012c). However, that approach is a contact method and does not yield the TM mechanical response under pressure directly. The present approach is a non-contact method, which does not induce any damage to the TM structure to testing; and air pressure is directly applied as loading. Instead of directly matching calculated deformation field with its experimental counterpart at merely a single pressure, in this work, volume displacement was used in best-fit to determine nonlinear mechanical properties of TM at a series of pressure states from negative pressure to positive pressure. Because the simulation was based on the assumption that chinchilla TM consists of a homogeneous, isotropic material, and its thickness is uniform over the entire pars tensa, the Young's modulus obtained in this study represents an overall averaged Young's modulus. In actual situation, due to the nonuniform distribution of the collagen fibers over TM, the thickness of TM varies at different locations (Kuypers et al., 2006; Kuypers et al., 2005; Van der Jeught et al., 2013). In addition, the mechanical properties can also change with locations. Therefore, even the model was developed from a 3D surface reconstruction of the specimen, there is still pronounced discrepancy between simulation and experiment locally. Shape difference of chinchilla TM between simulation and experiment is given in Figure 8. It can be seen that discrepancy is generally small at area with low deformation and high at area with high deformation, which is similar with Ghadarghadar's rat model. It is noted that the discrepancy of chinchilla TM is slightly larger than that of rat TM, which could be due to the difference of species. Despite the local displacement discrepancy, a good agreement is achieved between computational volume displacement and its experimental counterpart. The small positive errors and negative errors induced by thickness and properties nonuniformity are reduced through the summation process for the calculation of volume displacement. Therefore in order to reduce the complexity to determine mechanical properties with reverse-problem-solving scheme, it is more profitable to use volume displacement as the value function for optimization.

In the simulation, the thickness of TM was set as 10 µm. The value is averaged from the thickness of different locations of chinchilla TM according to result from histology study (Vrettakos et al., 1988). It should be noted that estimation of Young's modulus of TM from FE model is very sensitive to the TM thickness. Figure 9 shows the relation between thickness assumed for TM and the final estimation of Young's modulus. The estimated value dramatically increases as the assumed thickness of TM decreases. This could be another reason causing the large scattering of literature data of TM mechanical properties: as in most of the studies, TM thickness is assumed to be uniform. Nevertheless, the range of chinchilla TM thickness is between 8 μm and 12 μm. In this range, the variation of Young's modulus in figure 9 is about 15%, which is an acceptable fluctuation.

Fringe projection is utilized in this study due to its ability for full-field surface topography measurement, high accuracy (about 0.2% out-of-plane error (Liang, 2010)) and acceptable resolution (about 15 μm) for the relatively large deformation induced by pressure. As compared with other moiré techniques, such as shadow moiré, projection moiré and reflection moiré, it does not require precise alignment of the projective grating and objective gratings. It also does not require an accurate control system for phase-shifting, which is a benefit from a virtual phase-shifting applied on a single experimental image through the computerize processing. The aforementioned benefits show that fringe-projection technique is also potential to be used in measurement of dynamic properties with the help of high speed camera.

Data on chinchilla TM is sparse, we therefore compare Young's modulus, obtained in this study with measurement obtained for other animals. For rodent TM, using an indentation technique, Young's modulus of rat was measured as around 21 MPa, which is close to the average Young's modulus in this study. Young's moduli of TM of other animals around the size of chinchilla were also reported in a few of papers. Young's modulus of rabbit TM was reported as 30 MPa (Aernouts et al., 2010); and for cat the Young's modulus was estimated as 100~400 MPa (Fay et al., 2005). The size of chinchilla TM similar to human TM. For human, Young's moduli were reported in different situations. von Békésy reported 20 MPa under an *in-vivo* condition (von Békésy, 1960), similar values were obtained on TM samples along radial and circumferential directions by Luo *et at.* (Luo et al., 2009) under high strain rate. The Young's modulus of human TM measured by uniaxial tension of strips cut from TM was estimated at 10 MPa and 23 MPa, respectively (Decraemer et al., 1980; Kirikae, 1960). It is noted that, cutting TM breaks the collagen fibers, which subsequently shrink. This could induce variations from one specimen to another, causing a large variation of measurement results. Direct measurement of the mechanical properties from the entire pars tensa TM sample can maintain the integrity of TM and yields more reliable data. To the best of our knowledge the only full-field data on rat TM was presented (Ghadarghadar, et al., 2013). Young's modulus of intact TM can be estimated from storage modulus at frequency 0Hz, which are 40 MPa and 19 MPa, respectively for two samples (Ghadarghadar, 2013). The results from current study show that the Young's modulus of chinchilla TM is in the range of 11~ 30 MPa at strain below 25%, which is slightly higher than the reported Young's modulus of human TM. While data has been reported for elastic coefficients determined from numerous TMs, including human TM and guinea pig TM (Békéy, 1949; Gan et al., 2010; Guan et al., 2013; Zhang et al., 2013a; Zhang et al., 2013b), the stress-strain curve of chinchilla TM was not reported in literature, especially when it is measured from the intact TM. This study fills the gap by providing the nonlinear stress-strain relation, including Young’s modulus of chinchilla TM, 19.0 ±8.5 MPa, and tangent modulus at strains up to 31%.

5. CONCLUSION

The nonlinear mechanical response of chinchilla was determined using micro-fringe projection technique. Quasi-static air pressure was applied to a chinchilla TM at the lateral side through the ear canal inside the bulla. A micro-fringe projection method was used to measure the surface topography of the TM. The volume displacement of the TM was used as input to a finite element model for simulation. A 2nd-order Ogden hyperelastic model was used to describe the TM constitutive behavior of the TM in FEM for simulations. An inverse problem solving scheme was used to allow the pressure-volume displacement relationship simulated by FEM to match with the experimental results. The model parameters were then used to describe the mechanical behavior of chinchilla TM, and stress-strain curve. The Young’s moduli of the chinchilla TM were estimated as an average of about 19 MPa, up to a strain level of 25%. As strain increases from 0 to 31%, the tangent modulus decreases from 25 MPa to 11 MPa. The maximum stress experienced by the TM used in these experiments reaches 1.1 MPa.

ACKNOWLEDGMENTS

We acknowledge the support of NIH R01DC011585, DOD W81XWH-14-1-0228, DOD W81XWH-13-MOMJPC5-IPPEHA, and NSF CMMI-1031829, CMMI-1132174, and ECCS-1307997. Lu acknowledges the Louis A. Beecherl Jr. Chair for additional support.

REFERENCES

Aernouts, J., Dirckx, J.J.J. 2012a. Static versus dynamic gerbil tympanic membrane elasticity: derivation of the complex modulus. Biomech Model Mechan 11, 829-840.

Aernouts, J., Dirckx, J.J.J. 2012b. Viscoelastic properties of gerbil tympanic membrane at very low frequencies. J Biomech 45, 919-924.

Aernouts, J., Soons, J.A.M., Dirckx, J.J.J. 2010. Quantification of tympanic membrane elasticity parameters from in situ point indentation measurements: Validation and preliminary study. Hearing Res 263, 177-182.

Aernouts, J., Aerts, J.R.M., Dirckx, J.J.J. 2012c. Mechanical properties of human tympanic membrane in the quasi-static regime from in situ point indentation measurements. Hearing Res 290, 45-54.

Aerts, J.R.M., Dirckx, J.J.J. 2010. Nonlinearity in eardrum vibration as a function of frequency and sound pressure. Hearing Res 263, 26-32.

ASTM E8/E8M-13a, 2015. Standard Test Methods for TEnsion Testing of Metallic Materils. ASTM International , West Consholocken . PA.

Békéy, G.V. 1949. The structure of the middle ear and the hearing of one’s own voice by bone conduction. The Journal of the Acoustical Society of America 21, 217-232.

Buytaert, J.A.N., Dirckx, J.J.J. 2009. Tomographic imaging of macroscopic biomedical objects in high resolution and three dimensions using orthogonal-plane fluorescence optical sectioning. Appl Optics 48, 941-948.

Cheng, T., Dai, C.K., Gan, R.Z. 2007. Viscoelastic properties of human tympanic membrane. Ann Biomed Eng 35, 305-314.

Daphalapurkar, N.R., Dai, C.K., Gan, R.Z., Lu, H.B. 2009. Characterization of the linearly viscoelastlic behavior of human tympanic membrane by nanoindentation. J Mech Behav Biomed 2, 82-92.

De Greef, D., Aernouts, J., Aerts, J., Cheng, J.T., Horwitz, R., Rosowski, J.J., Dirckx, J.J.J. 2014. Viscoelastic properties of the human tympanic membrane studied with stroboscopic holography and finite element modeling. Hearing Res 312, 69-80.
Decraemer, W.F., Maes, M.A., Vanhuyse, V.J. 1980. An Elastic Stress-Strain Relation for Soft Biological Tissues Based on a Structural Model. J Biomech 13, 463-468.
Dirckx, J.J.J., Decraemer, W.F. 1991. Human Tympanic Membrane Deformation under Static Pressure. Hearing Res 51, 93-106.
Dirckx, J.J.J., Decraemer, W.F. 1997. Coating techniques in optical interferometric metrology. Appl Optics 36, 2776-2782.
Fay, J., Puria, S., Decraemer, W.F., Steele, C. 2005. Three approaches for estimating the elastic modulus of the tympanic membrane. J Biomech 38, 1807-1815.
Fung, Y.C. 1993. Biomechanics: Mechanical Properties of Living Tissues. 2nd ed. Springer, New York.
Funnell, W.R.J., Decraemer, W.F. 1995. On the incorperation of moire shape measurements in finite-element models of the cat eardrum. Journal of the Accoustic Society of America 100.
Gaihede, M., Liao, D., Gregersen, H. 2007. In vivo arealmodulus of elasticity estimation of the human tympanic membrane system: modelling of middle ear mechanical function in normal young and aged ears. Physics in Medicine and Biology 52, 803-814.
Gan, R.Z., Dai, C.K., Wang, X.L., Nakmali, D., Wood, M.W. 2010. A totally implantable hearing system - Design and function characterization in 3D computational model and temporal bones. Hearing Res 263, 138-144.
Gea, S.L.R., Decraemer, W.F., Funnell, W.R.J., Dirckx, J.J., Maier, H. 2010. Tympanic membrane boundary deformations derived from static displacements observed with computerize tomography in human and gerbil. Journal of the Association for Research in Otolaryngology 11, 1-17.
Ghadarghadar, N., Agrawal, S.K., Samani, A., Ladak, H.M. 2013. Estimation of the quasi-static Young's modulus of the eardrum using a pressurization technique. Comput Meth Prog Bio 110, 231-239.
Ghiglia, D.C., Pritt, M.D. 1998. Two-dimensional phase unwrapping, Theory, Algorithms, and Software John Wiley and Sons, New York.
Guan, X.Y., Gan, R.Z. 2013. Mechanisms of Tympanic Membrane and Incus Mobility Loss in Acute Otitis Media Model of Guinea Pig. Jaro-J Assoc Res Oto 14, 295-307.
De Greef, D., Soons, J., Dircks, J.J.J. 2014a . Digital stroboscopic holography setup for deformation mesaurenet at both quasi-static and accoustic frequencied. IInt J Optomech 8, 275-191.
De Greef,D. D., Aernout, J., Aerts, J., Cheng, J.T., Horwitz, R., Rosowski, J.J. Dirckx, J.J.J. 2014b. Viscoelastic properties of the human tympanic membrane studid with stroboscopic holography and finite element odeling. hearing Res 312, 59-80
Hesabgar, S.M., Marshall, H., Agrawal, K.K., Samani, A., Ladak, H. M 2010. Measuring the quasi-static Young's modulus of the eardrum using an indentation technique, Hearing res 263, 168-176
Huang, G., Daphalapurkar, N.P., Gan, R.Z., Lu, H.B. 2008. A method for measuring linearly viscoelastic properties of human tympanic membrane using nanoindentation. J Biomech Eng-T Asme 130.
Kirikae, I. 1960. The structure and function of middle ear University of Tokyo Press, Tokyo.
Kuypers, L.C., Decraemer, W.F., Dirckx, J.J.J. 2006. Thickness distribution of fresh and preserved human eardrums measured with confocal microscopy. Otol Neurotol 27, 256-264.
Kuypers, L.C., Decraemer, W.F., Dirckx, J.J.J., Timmermans, J.P. 2005. Thickness distribution of fresh eardrums of cat obtained with confocal microscopy. Jaro-J Assoc Res Oto 6, 223-233.
Ladak, H.M., Decraemer, W.F., Dirckx, J.J.J., Funnell, W.R.J. 2004. Response of the cat eardrum to static pressures: Mobile versus immobile malleus. J Acoust Soc Am 116, 3008-3021.
Ladak, H.M., Funnell, W.R.J., Decraemer, W.F., Dirckx, J.J.J. 2006. A geometrically nonlinear finite-element model of the cat eardrum. J Acoust Soc Am 119, 2859-2868.
Lee, C.Y., Rosowski, J.J. 2001. Effects of middle-ear static pressure on pars tensa and pars flaccida of gerbil ears. Hearing Res 153, 146-163.
Liang, J. 2010. Determination of the Mechnical Properties of Guinea Pig Typanic Membrane Using Combined Fringe Projection and Simulations, Oklahoma State University

Luo, H.Y., Dai, C.K., Gan, R.Z., Lu, H.B. 2009. Measurement of Young's Modulus of Human Tympanic Membrane at High Strain Rates. J Biomech Eng-T Asme 131.

Luo, H., Lu, H., Dai, C., Gan, R. 2009b. A comparision of Young's modulus for normal and diseased human eardrums at high strain rates. Int J Exp Comput Biomech 1, 1-22

O'Connor, K.N., Tam, M., Blevins, N.H., Puria, S. 2008. Tympanic Membrane Collagen Fibers: A Key to High-Frequency Sound Conduction. Laryngoscope 118, 483-490.

Ortiz, M., Patterson, E.A. 2003. On the industrial applications of moire and fringe projection techniques. Strain 39, 95-100.

Ortiz, M.H. 2004. Novel Development of Moire Techniques for Industrial Application, University of Sheffield.

Ortiz, M.H., Patterson, E.A. 2005. Location and shape measurement using a portable fringe projection system. Exp Mech 45, 197-204.

Ritenour, A.E., Wickley, A., Ritenour, J.S., Kriete, B.R., Blackbourne, L.H., Holcomb, J.B., Wade, C.E. 2008. Tympanic membrane perforation and hearing loss from blast overpressure in operation enduring freedom and operation Iraqui freedom wounded. The Journal of TRAUMA Injury, Infection, and Crilical Care 64, 174-178.

Rosowski, J.J., Lee, C.Y. 2002. The effect of immobilizing the gerbil's pars flaccida on the middle-ear's response to static pressure. Hearing Res 174, 183-195.

Rsowski, J.J. Nakajima, H.H., Cheng, J.T. 2014 Current topics in the study of sound conduction to the inner ear, Chapter 26 in Perspectives on Auditor Research, A.N.. Popper and R.R. Fay (eds), Springer, handbook of Auditory Research 50, 493-511.

Salamati, E., Agrawal, S.K., Smani, A., Lakak, H. 2012. Estimation of the othotropic elastic properties of the rat eardrum. J Med Biol Eng 32, 225-234

Soons, J.A.M., Aernouts, J., Dirckx, J.J.J. 2010. Elasticity modulus of rabbit middle ear ossicles determined by a novel micro-indentation technique. Hering Res 263, 33-37

Standard, A. 2015. Standard Test Methods for Tension Testing of Metallic Materials, Vol. E8/E8M − 13a. ASTM International, West Conshohocken, PA.

Tornton, J.L, Chevallier, KM, Koka, K., Gabbard, S.A., Tollin, D. 2013. Conductive hearing loss induced by experimental middle-ear effusion in a chinchilla model reveals impaired tympanic membrane-couple ossicular chain movement. J Assoc Res Otolaryngo 14 451-465.

Van der Jeught, S., Dirckx, J.J.J., Aerts, J.R.M., Bradu, A., Podoleanu, A.G., Buytaert, J.A.N. 2013. Full-Field Thickness Distribution of Human Tympanic Membrane Obtained with Optical Coherence Tomography. Jaro-J Assoc Res Oto 14, 483-494.

Volandri, G., Di Puccio, F., Forte, P., Carmignani, C. 2011. Biomechanics of the tympanic membrane. J Biomech 44, 1219-1236.

von Békésy, G. 1960. Experiments in Hearing McGraw-Hill Book Company, New York.

von Unge, M., Dircks, J.J. 2009. Functional effects of repeated pressure loads upon the tympanic membrane: mechanical stiffness measurements after simulated habitual sniffing. Eur Arch Oto-Rhino-L 266, 1219-1224.

von Unge, M., Decraemer, W.F., Baggersjoback, D., Dirckx, J.J. 1993. Displacement of the Gerbil Tympanic Membrane under Static Pressure Variations Measured with a Real-Time Differential Moire Interferometer. Hearing Res 70, 229-242.

Vrettakos, P.A., Dear, S.P., Saunders, J.C. 1988. Middle ear Structure in the Chinchilla: A Quantitative Study. AM J Otolaryngology 9, 58-67.

Wang, B., Lu, H., Kim, G. 2002. A damage model for the fatigue life of elastomeric materials. Mechanics of Materials 34, 475-483.

Wang, X.L., Cheng, T., Gan, R.Z. 2007. Finite-element analysis of middle-ear pressure effects on static and dynamic behavior of human ear. J Acoust Soc Am 122, 906-917.

Zhang, X.M., Gan, R.Z. 2010. Dynamic properties of human tympanic membrane – experimental measurement and modelling analysis Int. J. Experimental and Computational Biomechanics 1, 252-270.

Zhang, X.M., Gan, R.Z. 2013a. Finite element modeling of energy absorbance in normal and disordered human ears. Hearing Res 301, 146-155.

Zhang, X.M., Gan, R.Z. 2013b. Dynamic Properties of Human Tympanic Membrane Based on Frequency-Temperature Superposition. Ann Biomed Eng 41, 205-214.

List of Tables

Table 1 Dimensions of chinchilla TM and parameters of the 2-order Ogden hyperelastic model.

Sample Number	Superior-inferior Diameter (mm)	Anterior-posterior Diameter (mm)	μ_1	α_1	μ_2	α_2
15-1-1L	7.66	8.89	1.4	4.3	7.8	-3.6
15-1-1R	7.71	8.08	1.6	3.7	8.7	-4.1
15-1-2L	8.68	8.59	1.0	4.3	5.7	-4.0
15-1-4R	7.37	7.93	1.2	4.5	7.8	-4.4
15-1-5L	7.57	8.53	1.3	4.1	7.2	-4.9
15-1-5R	6.84	7.97	1.2	3.4	7.9	-4.0
15-1-6R	7.99	9.15	1.0	3.1	6.9	-5.0
15-1-7L	7.65	8.42	1.1	3.3	6.6	-5.0
15-1-8L	7.56	8.76	1.1	4.2	6.7	-4.7
15-1-8R	7.49	9.08	1.0	3.9	6.2	-3.8
Average	7.65	8.54	1.2	3.9	7.1	-4.3

List of Figures:

Figure 1 The experimental setup of micro-fringe projection system and the pressure loading and monitoring system.(a) Schematic diagram;(b) Actual setup. The component in (b): monometer (MA), camera (CA), surgical microscope (SM), sample holder (SH), XYZ-translation stage (TS), object lens (OL), grating (RR), condenser lenses (CL), fiber optics (FO) and pressure control (PC).

Figure 2 Chinchilla bulla prepared for measurements: (a) The medial side of TM with intact malleus-incus immobilized; (b) Typical sample with TM exposed and PVC tube inserted.

Figure 3 Typical precondition curve of chinchilla TM.

Figure 4 TM images under projected micro-fringes for surface topography. (a). Micro-projected fringes on a guinea pig TM; (b). Height profile $z(x,y)$ under zero pressure; (c). Z-displacement U_3 under 0.5 kPa pressure; (d). Z-displacement U_3 under 1.0 kPa pressure.

Figure 5 Finite element model of TM in different views. (a). Medial-view of meshed TM; (b). Posterior view of meshed TM; (c). Boundary conditions and applied pressure.

Figure 6 (a) Pressure-volume displacement relationships for ten chinchilla TMs under different pressures (b). A comparison of finite element simulation results with experimental data. The error bar represents the standard deviation from the tests.

Figure 7 Mechanical response and mechanical properties of all 10 chinchilla TMs: (a) Tensile stress-strain curves; (b) Tangent modulus of guinea pig TM determined from the Ogden model.

Figure 8 (a) Error map calculated as z coordination between measured pressurized shape and simulated pressurized shape. (b). A plot of a line crossing posterior- umbo and anterior shown as black dash line in figure 8(a). (c). A plot of a line crossing posterior shown as red dash line in figure 8(a).

Figure 9 Relation between thickness assumed for TM in simulation and the final Young's Modulus evaluated for one typical specimen.

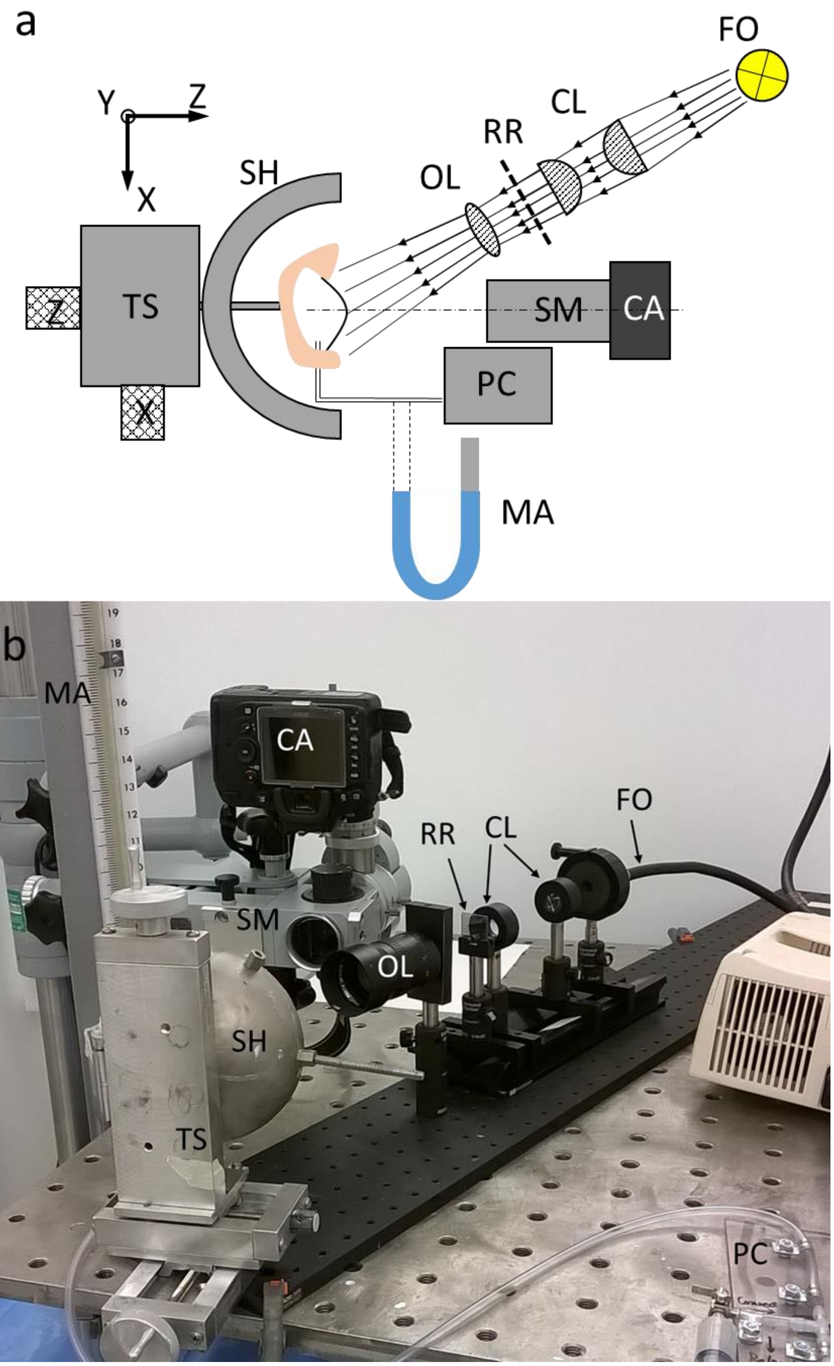

Figure 1 The experimental setup of micro-fringe projection system and the pressure loading and monitoring system.(a) Schematic diagram;(b) Actual setup. The component in (b): manometer (MA), camera (CA), surgical microscope (SM), sample holder (SH), XYZ-translation stage (TS), object lens (OL), grating (RR), condenser lenses (CL), fiber optics (FO) and pressure control (PC).

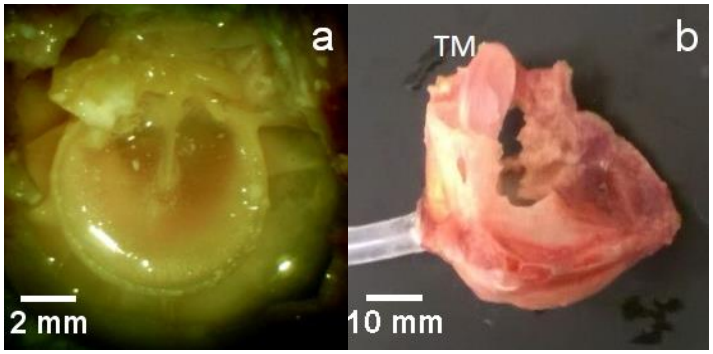

Figure 2 Chinchilla bulla prepared for measurements: (a) The medial side of TM with intact malleus-incus immobilized; (b) Typical sample with TM exposed and PVC tube inserted.

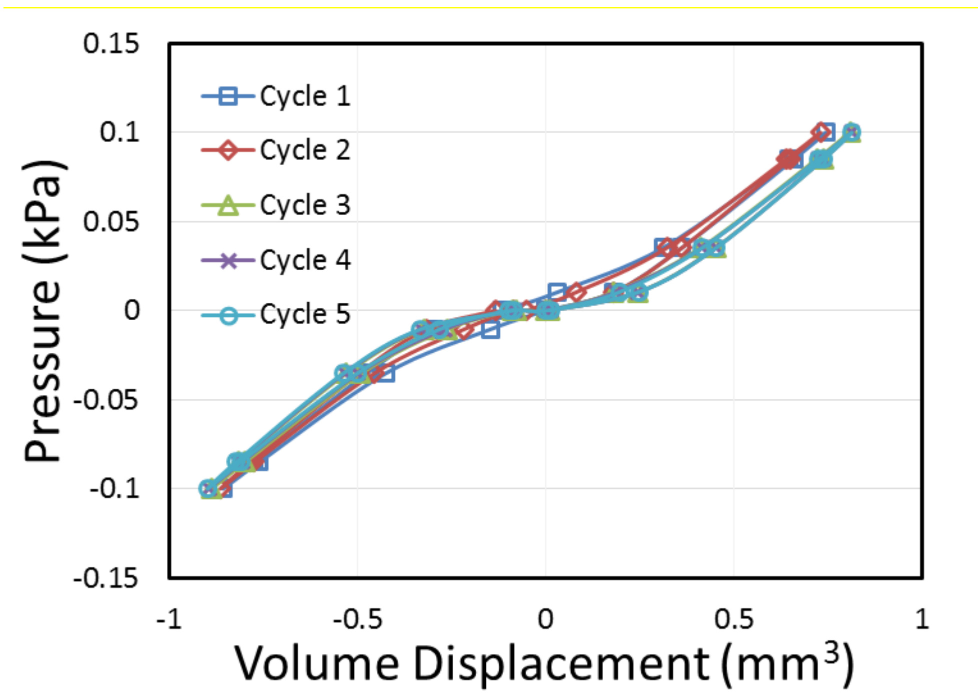

Figure 3 Typical precondition curve of chinchilla TM.

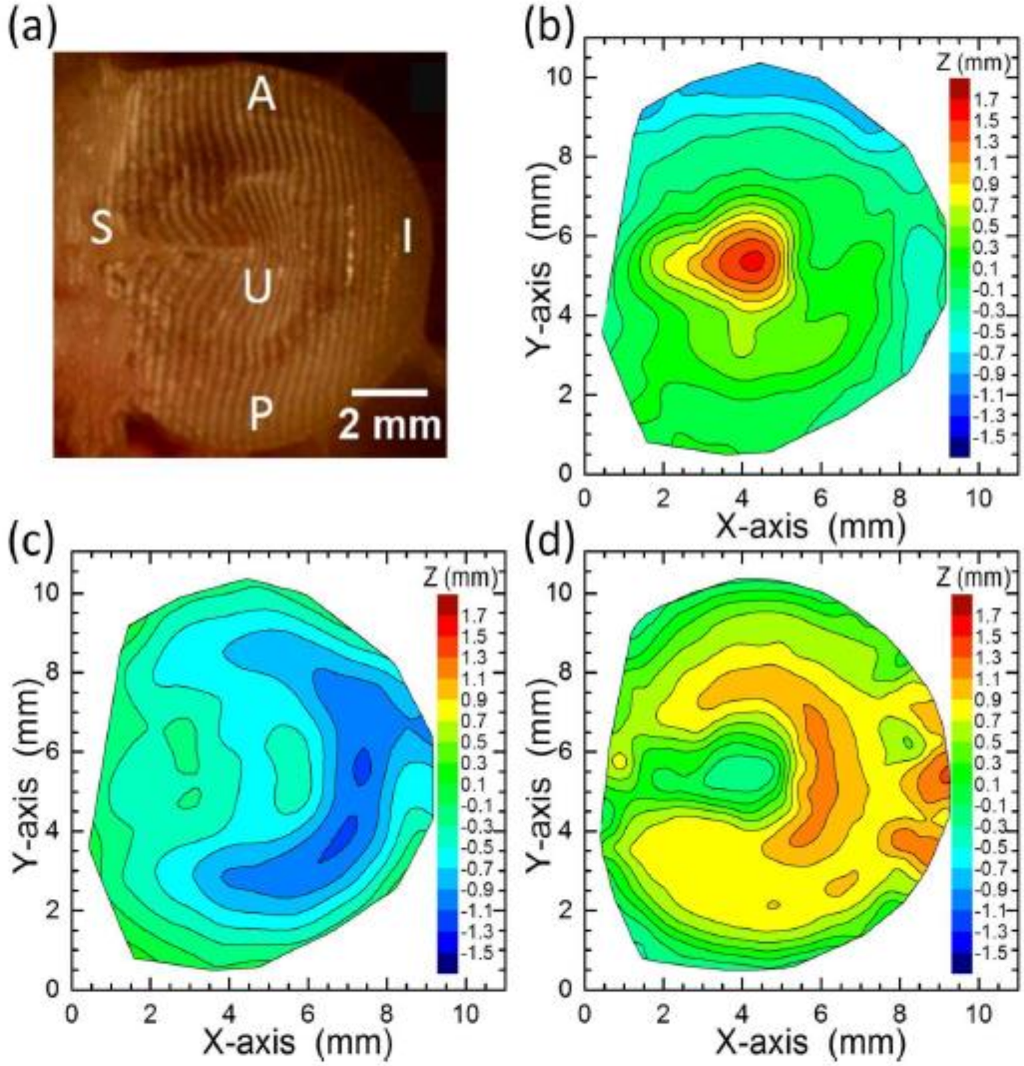

Figure 2 TM images under projected micro-fringes for surface topography. (a). Micro-projected fringes on a guinea pig TM; (b). Height profile $z(x,y)$ under zero pressure; (c). Z-displacement U_3 under 0.5 kPa pressure; (d). Z-displacement U_3 under 1.0 kPa pressure.

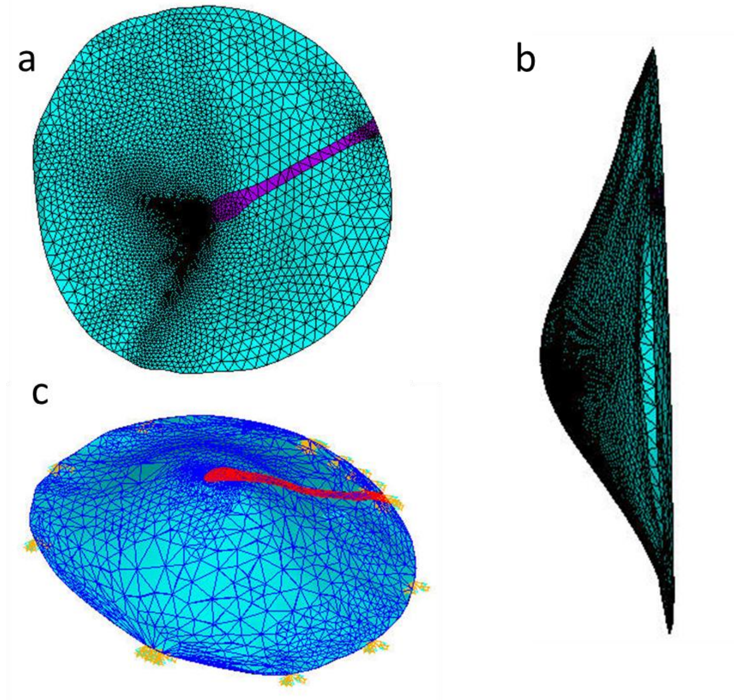

Figure 3 Finite element model of TM in different views. (a). Medial-view of meshed TM; (b). Posterior view of meshed TM; (c). Boundary conditions of TM, which is shown with yellow arrows.

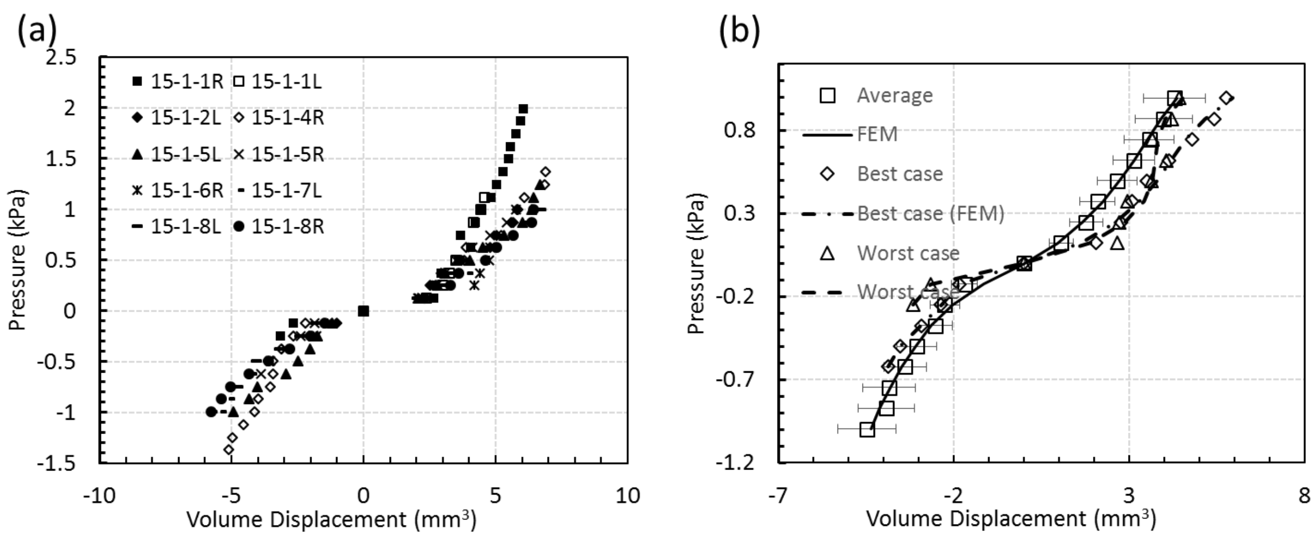

Figure 4 (a) Pressure-volume displacement relationships for ten chinchilla TMs under different pressures (b). A comparison of finite element simulation results with experimental data. The error bar represents the standard deviation from the tests.

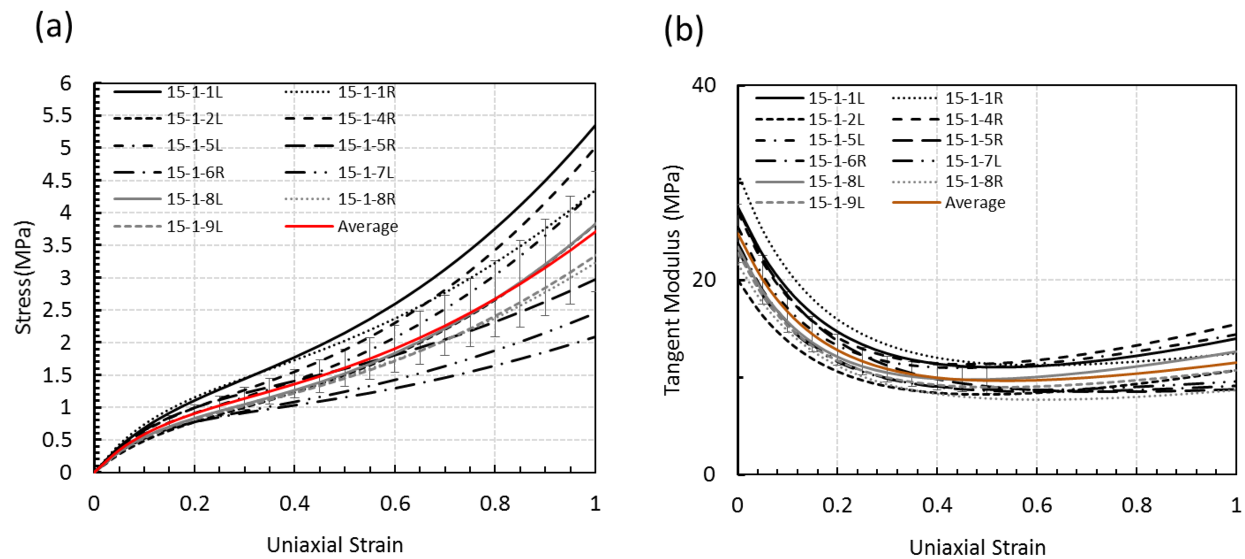

Figure 5 Mechanical response and mechanical properties of all 10 chinchilla TMs: (a) Tensile stress-strain curves; (b) Tangent modulus of guinea pig TM determined from the Ogden model**.**

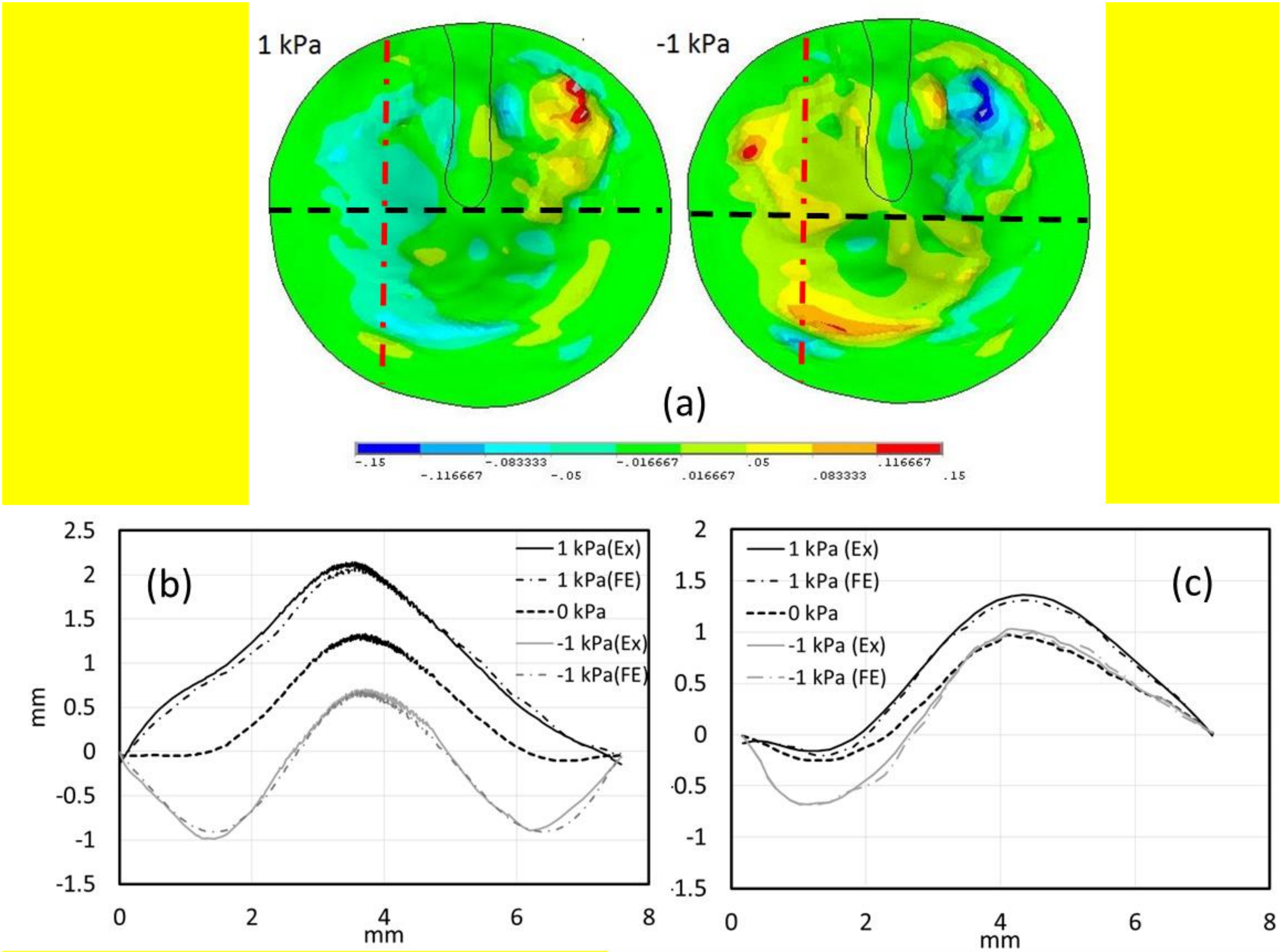

Figure 8 (a) Error map calculated as z coordination between measured pressurized shape and simulated pressurized shape. (b). A plot of a line crossing posterior- umbo and anterior shown as black dash line in figure 8(a). (c). A plot of a line crossing posterior shown as red dash line in figure 8(a).

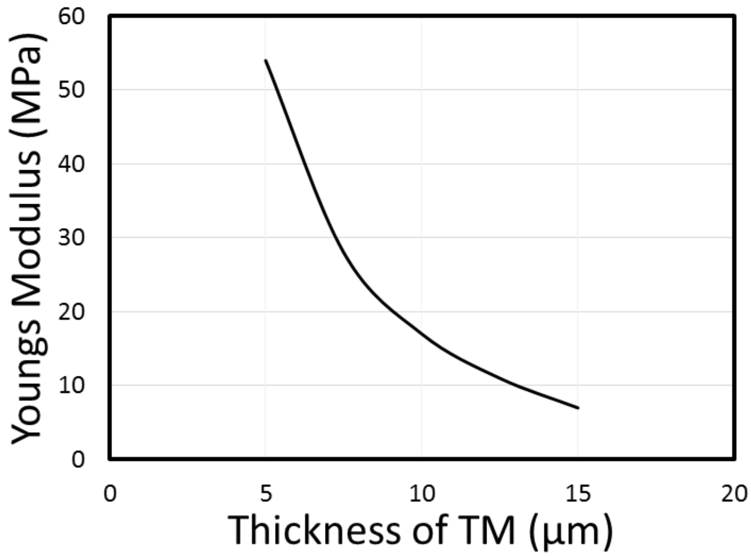

Figure 9 Relation between thickness assumed for TM in simulation and the final Young's Modulus evaluated for one typical specimen.

Appendix C

Mechanical Property of Human Eardrum at High Strain Rates after Exposure to Blast Wave

[a]Luo, H., [a]Liang, J., [b]Nakmali, D., [b]Gan, R. Z., and [a]Lu, H.
[a] Department of Mechanical Engineering, University of Texas at Dallas, Richardson, TX 75080, USA
[b] School of Aerospace and Mechanical Engineering, University of Oklahoma, Norman, OK 73019, USA

Abstract
Mechanical properties of tympanic membrane (TM) were characterized at high strain rate after the TM is subject to blast wave. A miniature split Hopkinson tension bar was used to investigate the mechanical behavior of human eardrum before and after exposure to blast wave. A human bulla with the intact TM is subjected to blast wave at first, after that TM strip specimens prepared along radial and circumferential directions are used in tension on a miniature split Hopkinson tension bar. The mechanical properties of human before and after experiencing blast wave was compared and discussed. Mechanical properties in the time-domain was converted to the corresponding properties in the frequency domain to investigate the effect of blast wave on the viscoelastic properties. The results contribute to the understanding of effect of blast wave on hearing loss.

C1. Experiments

C1.1 Preparation of Human TM Strip Specimens

The human bulla with entire TM and the bone chains inside and outside ear pinna were horizontally placed inside a blast chamber (Fig 1a, and 1b), and subjected to blast wave with less than 5 psi peak pressure for four times until rupture. Then the ruptured TM was harvested from the bulla, with the tympanic annulus and malleus attached, for dynamic tensile experiments using miniature split tension bar (Fig 1c).

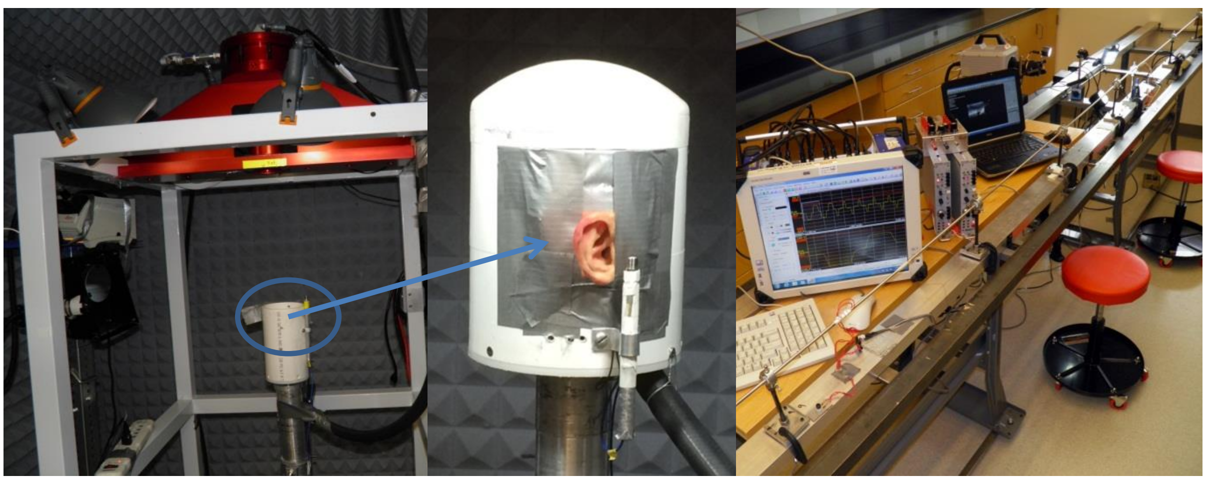

(a) (b) (c)

Figure 1. Blast wave setup. (a). A blast chamber to shock human TM bone under blast wave;
(b). A human TM bone embedded inside a dumpy head under blast wave;
(c). A miniature split Hopkinson pressure tension bar to test human TM bone after blast wave under high strain rate.

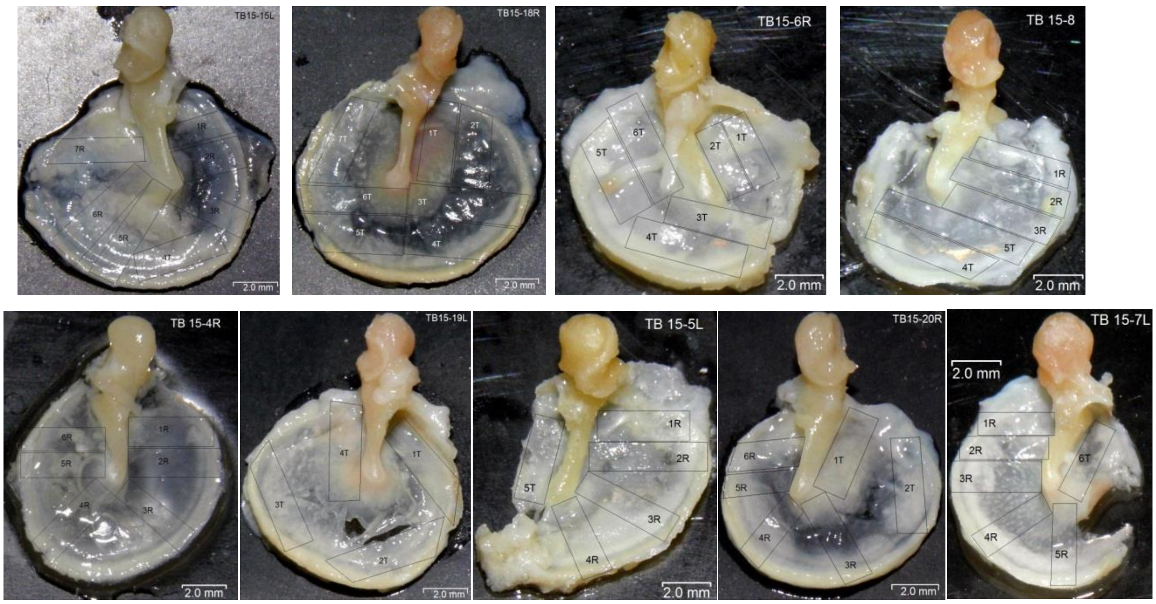

Figure 2. TM after blast wave cut into strips specimen. Note, broken TM strips were cut according to the broken shape, to cut more specimen either along radial direction or circumferential direction.

The TM samples were immersed in 0.9% saline solution. Each TM sample was cut into 1~1.5 mm wide and 4~5 mm long rectangular strip specimens along either the radial (Figure 1(a)) or circumferential (Figure 2) direction in the pars tensa part of the TM using surgical knifes. Along the crack of broken TM, more possible TM strips were cut either/both along radial or/and circumferential directions. The specimens for measurement of Young's modulus in the radial direction were cut along the radial fibers, and the specimens for measurement of circumferential direction were cut nearly along the local circular fiber direction. After cutting, each strip specimen was placed immediately in saline solution again, and was used in experiment within 5~10 minutes. Hybrid orientations of the TM strips cut from a TM sample are shown in Fig 2. In this investigation, 9 control TMs were blasted, then used for tensile at high strain rate. The list of normal/control TM specimens was given in reference by Luo et al. (2008a), prepared from 11 normal TM samples as comparison.

C1.2 SHTB Experiments

A miniature split Hopkinson tension bar (SHTB) was developed for tensile tests of TM strip specimen at high strain rates. A schematic diagram for the SHTB setup is shown in Figure 3. The incident bar is a 3.66 meter long aluminum 7075-T6 bar with 6.4 mm diameter. The transmission bar is a 2.74 meter long hollow 6061-T6 bar with 5 mm inner diameter (ID) and 6.4 mm outer diameter (OD). Two clamp fixtures were used to grip a TM strip specimen. The aluminum tubing striker bar, launched manually by hand, made impact with the flange thread-connected to the incident bar, to load the specimen. Two semiconductor strain gages with a gage factor 176 were mounted on opposite surfaces in the middle of the hollow transmission bar to measure the weak strain signal representing the transmitted wave. A HBM Genesis 5i digital oscilloscope was used to acquire all strain signals on bars through a Wheatstone bridge and Vishay 2310B signal conditioning amplifier. A plastic collar was used as a pulse shaper to assist to reach dynamic stress equilibrium and a constant strain rate condition.

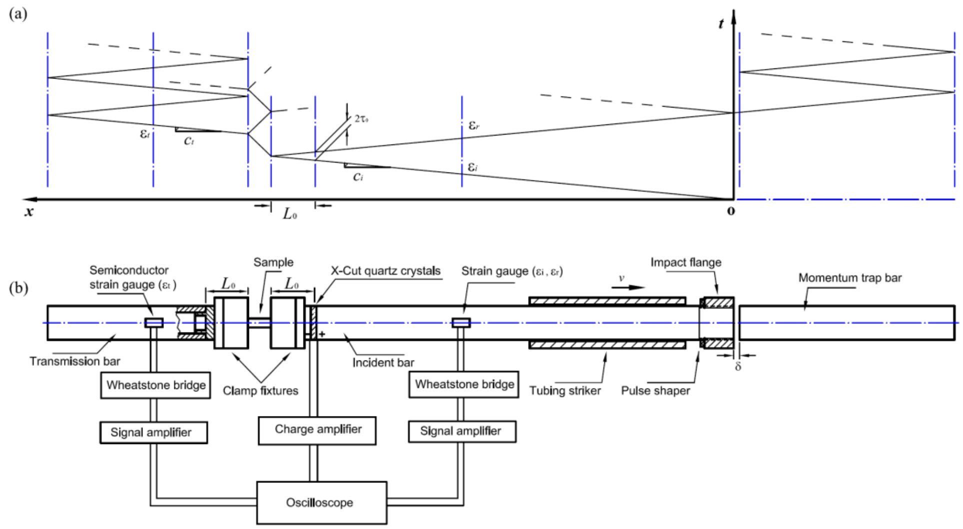

Figure 3. Schematic of the miniature split Hopkinson tension bar. (a). Analysis of stress wave propagation along Hopkinson bars; (b). schematic setup of a miniature SHTB. Note, (1). Semiconductor strain gage attached on hollow transmission bar (Kyowa, K =176); (2). X-Cut quartz crystals monitoring front force on incident bar; (3). Polymer thin collar pulse shaper employed;

With the use of a clamping fixture between the TM strip specimen and a bar end, under a valid SHTB experiment, formulas for the stress and strain rate in a specimen are modified as

$$\sigma_s(t) = \frac{A_t}{A_s} E_t \varepsilon_t(t) \tag{1}$$

$$\dot{\varepsilon}_s(t) = \frac{1}{L_s}[(c_i - c_t\beta)\varepsilon_i(t) - (c_i + c_t\beta)\varepsilon_r(t)] \tag{2}$$

where $\beta = E_i A_i/(E_t A_t)$; E, c, ε, σ, A and L are Young's modulus, bar wave speed, strain, stress, cross-sectional area, and length, respectively; the subscripts i, t, r represent the incident, transmitted, reflected signals, respectively. The subscript s indicates specimen. The strain history is obtained through the integration of strain rate with respect to time. The tensile tests were conducted at room temperature 23±2 °C under relative humidity 40±5%. Tensile tests for normal and diseased TM specimens were conducted within three ranges of strain rates, namely, 100~500 s^{-1}, 500~1000s^{-1} and 1000~2500 s^{-1}.

C3. Results

For TM strip specimens in the radial and circumferential directions, the Young's modulus values are summarized in Table 1. In order to compare the experimental data at different strain rates, the Young's modulus values are averaged within one of the three strain rate ranges, 100~500 s^{-1}, 500~1000 s^{-1} and 1000~2500 s^{-1}, respectively. The average Young's modulus values of normal TM within different strain rate ranges in this work are given in Table 1. Within each range of strain rate, the Young's modulus tends to be close, so that the results are averaged, and are representative of the data within that strain rate range.

From Table 1, the data shows about 20~30% variation in Young's modulus obtained from different TM specimens.

Table 1. Mechanical properties of control human eardrum

Eardrum	Samples	Strain rate (1/s)	Young's modulus (MPa)	Maximum stress (MPa)	Maximu m strain	Fiber Direction
Control intact	11	309±77	45.2±10.2	6.3±3.4	11±3	Y
	15	714±146	51.4±16.6	10.4±3.4	20±7%	Y
	7	1654±381	58.9±18.5	15.9±7.3	41±10%	Y
	21	333±68	34.1±11.2	4.3±1.8	11±2%	X
	6	772±176	40.6±7.6	7.7±2.5	14±8%	X
	7	1353±362	56.8±15.7	13.7±5.5	37±10%	X

From these results, the Young's modulus as a function of strain rate is plotted in Figures 4(a) and 4(b) for normal TMs in radial and circumferential directions, respectively. The *y*-axis error bars represent standard deviation of Young's modulus between the experimental data and the fitted curves.

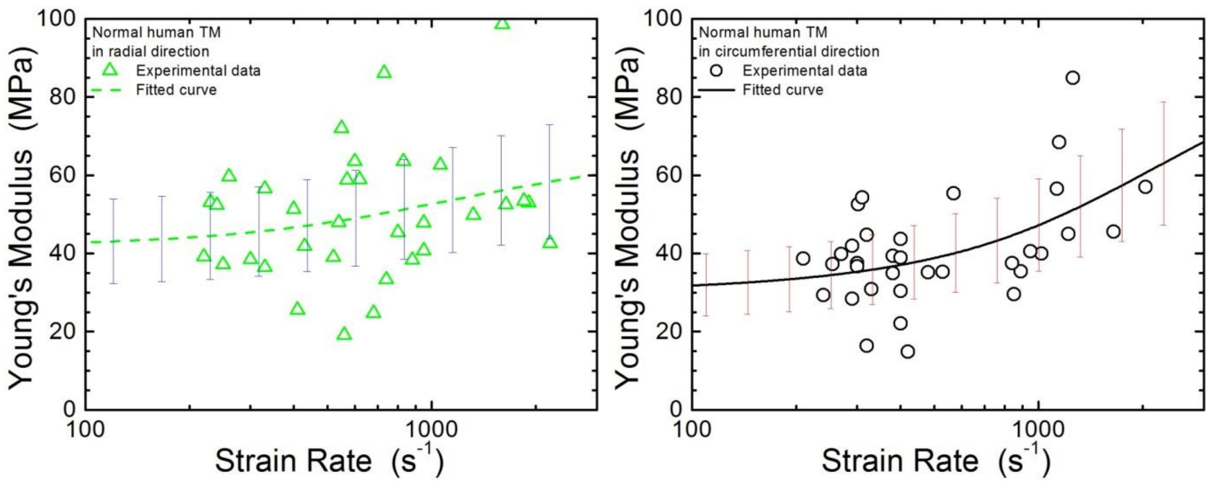

(a) (b)

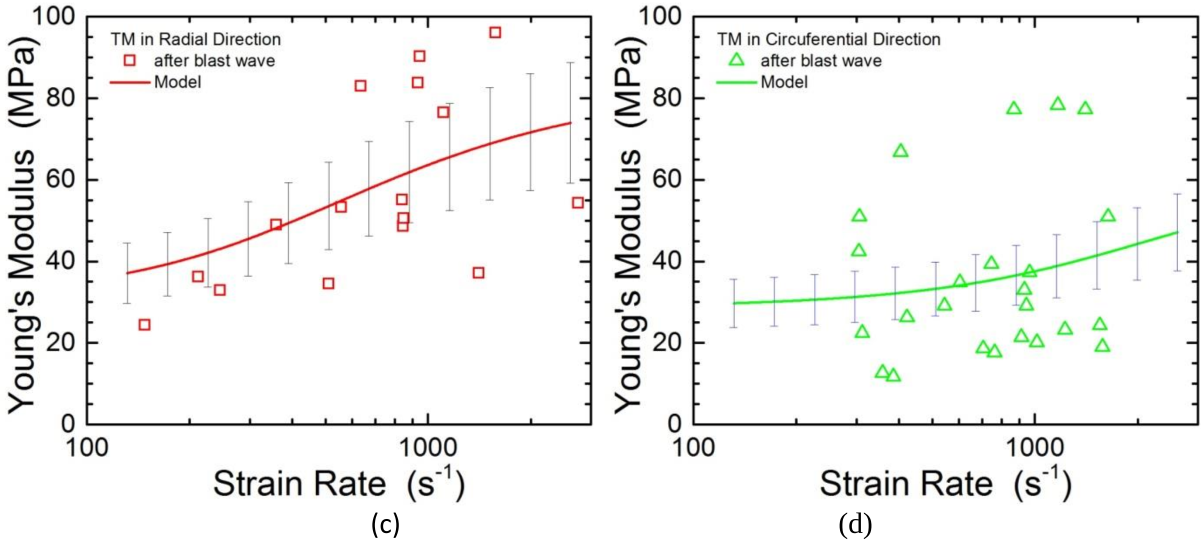

Figure 4. Comparison of Young's modulus of TMs at different strain rates. (a). Control TMs in radial direction; (b). Control TMs in circumferential direction; (c). Blasted TMs in radial direction; (d). Blasted TMs in circumferential direction.

The Young's modulus data of blasted TMs under high strain rates are summarized in Table 2. Two typical TM strip specimens after exposure to blast wave after tensile testing at strain rates higher than 500 s^{-1} are shown in Figure 5. From these results, the Young's modulus as a function of strain rate is plotted in Figs. 4c and 4d for blasted TMs in radial and circumferential directions, respectively.

Table 2. Mechanical properties of blasted human eardrum

Eardrum	Samples	Strain rate (1/s)	Young's modulus (MPa)	Maximum stress (MPa)	Maximum strain	Fiber direction
After blast wave	4	241±36	35.6±10.2	5.0±3.3	17±12%	Y
	8	765±171	62.4±20.4	9.3±8.1	15±10%	Y
	4	1714±721	66.0±25.7	10.9±5.3	21±15%	Y
	7	356±49	33.3±20.7	4.7±2.3	14±4%	X
	10	798±149	33.7±17.1	8.6±5.5	25±9%	X
	7	1368±237	41.9±26.8	11.9±9.3	28±13%	X

Notes: X - circumferential direction; Y - radial direction

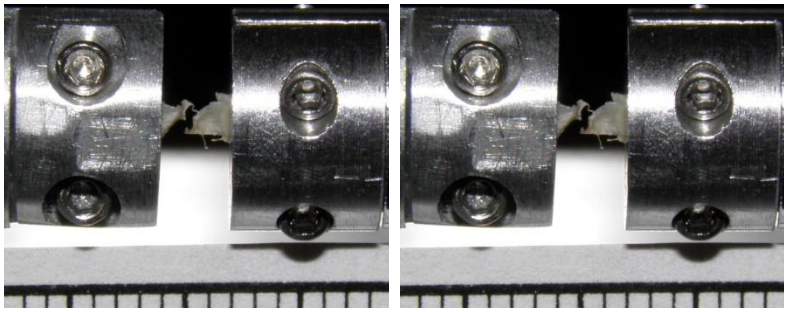

Figure 5. Typical Failed TM Specimens. (a). TM (TB15-18R-T7) in circumferential direction after blast wave; (b). TM (TB16-15L-R3) in radial direction after blast wave.

C4 Discussions

The above results indicate that the Young's modulus of TM depends on the strain rate within high strain rate range. Since data for the Young's modulus has been obtained within three ranges of high strain rates (300-2000 s^{-1}), we model the mechanical behavior of the TM as a standard linear solid with three undetermined parameters. Figure 6 shows the standard linear model consisting of two springs, with spring constants E_∞, E_1, and a dashpot with viscosity η.

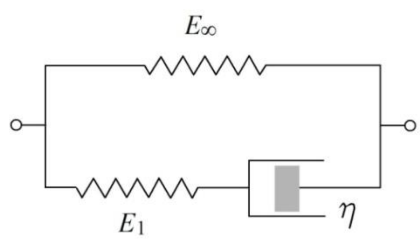

Figure 6. A standard linear solid model.

The relaxation time of the model is $\tau = \eta/E_1$. For the standard linear solid under the uniaxial tension, the Young's relaxation modulus $E(t)$ is given as

$$E(t) = E_\infty + E_1 e^{-t/\tau} \tag{3}$$

For a linear viscoelastic material at a constant strain rate $\dot{\varepsilon}_0$, the strain history is $\varepsilon(t) = \dot{\varepsilon}_0 t$. The average relaxation modulus $\overline{E}(t)$ is determined between initial time and the ending time of nearly linear stress-strain curve. From an experimental stress-strain curve, the Young's modulus is determined before the limit of linearity, ε_e. The time t is determined by $t = \varepsilon_e / \dot{\varepsilon}_0$. Considering the standard linear solid model in Equation (3), the average relaxation modulus $\overline{E}(t)$ as a function of time t (i.e., terminal time corresponding to ε_e) and the Young's modulus $\overline{E}(\dot{\varepsilon})$ as a function of strain rate $\dot{\varepsilon}_0$ are given as

$$\overline{E}(t) = E_\infty + E_1(1-e^{-t/\tau})\tau/t \quad \text{and} \quad \overline{E}(\dot{\varepsilon}) = E_\infty + E_1(1-e^{-\varepsilon_e/\dot{\varepsilon}\tau})\tau\dot{\varepsilon}/\varepsilon_e \tag{4}$$

All the individual Young's modulus data (as shown in Table 1) at the actual strain rates measured in SHTB tests are used as inputs to fit into one of the above equations, to search for the three best-fit parameters E_∞, E_1, and η. Table 3 summarizes the three best-fit parameters for both normal and diseased TMs in radial and circumferential directions. Hence the best-fit Young's modulus is plotted in Figure 6 as a function of strain rate (10^2~2×10^4 s^{-1}).

Table 3 Best-Fit Parameters for Young's Relaxation Modulus

Eardrum	*Modulus coefficient* E_∞ (*MPa*)	*Modulus coefficient* E_1 (*MPa*)	*Relaxation time* τ (10^{-5} *s*)	*Specimen orientation*
Control	41.5	25.4	5.07	R
Control	30.0	69.1	2.53	C
Blasted	30.1	52.6	10.3	R
Blasted	28.5	35.5	2.61	C

Notes: R: radial direction; C: circumferential direction.

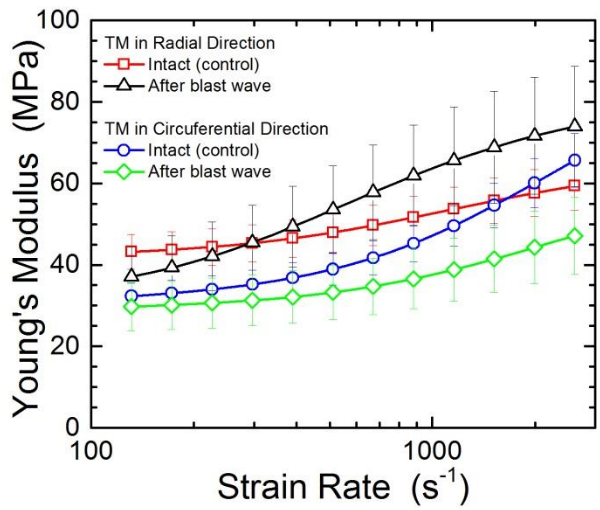

Figure 7. Summary of fitted curves for control and blasted TMs with relation of strain rates

It is seen that the mechanical property data points are scattered, a characteristic with bio-tissues. Nevertheless the curves still agree reasonably well with the experimental data. With these curves, the Young's modulus can be determined at other strain rates within 300-2000 s^{-1}.

With the parameters in Equation (4) determined, the Young's relaxation modulus $E(t)$ can be determined. The Young's relaxation modulus was obtained for TM in both radial and circumferential directions, as shown in Figure 8. From Figure 8, the relaxation modulus can be determined for other times.

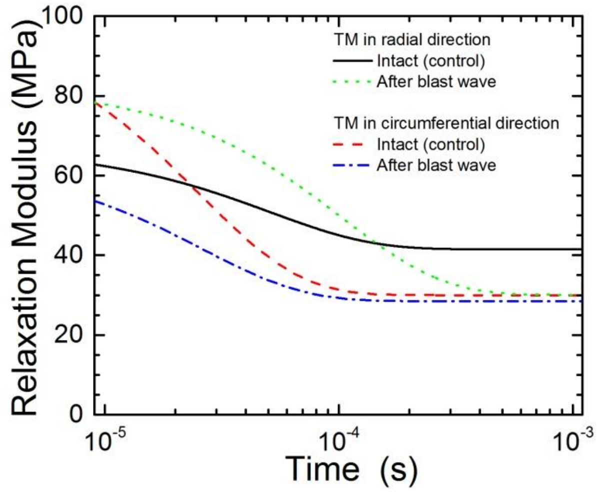

Figure 8. Comparison of Young's relaxation modulus between control and blasted TM in time domain.

We next convert the relaxation modulus in time domain to the complex modulus in frequency domain. The complex modulus is expressed as $\tilde{E}(\omega) = E'(\omega) + iE''(\omega)$, with $E'(\omega)$ being the storage modulus and loss modulus $E''(\omega)$ the loss modulus. The loss tangent is $\tan\theta = E''/E'$. For the standard linear solid in frequency domain, storage modulus $E'(\omega)$ and loss modulus $E''(\omega)$ are calculated as (Knauss et al., 2008)

$$E'(\omega) = E_\infty + E_1\tau^2\omega^2/(1+\tau^2\omega^2), \text{ and } E''(\omega) = E_1\tau\omega/(1+\tau^2\omega^2) \tag{5}$$

where ω is angular frequency, $\omega = 2\pi f$, f is the frequency. The frequency f corresponds approximately to the strain rate (Emri et al., 2005) in the calculation of viscoelastic properties. The storage and loss moduli of TM are shown in Figures 9(a) and 9(b) determined using Equation (5), respectively. The loss tangent values of TM in both radial and circumferential directions are shown Figure 9c.

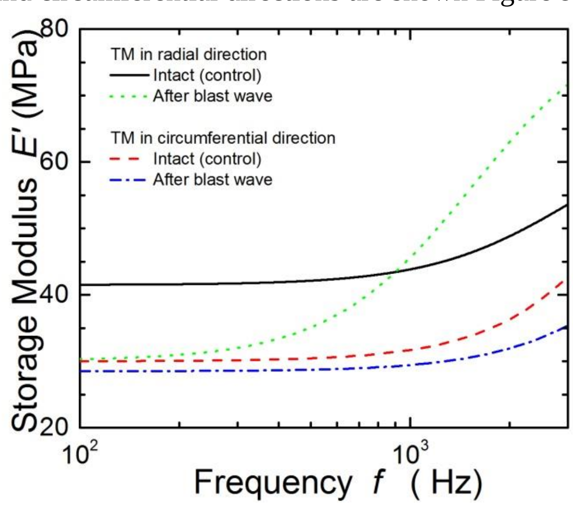

(a)

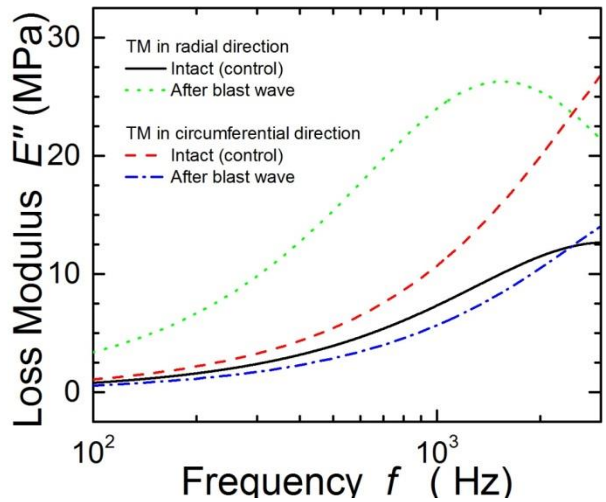

(b)

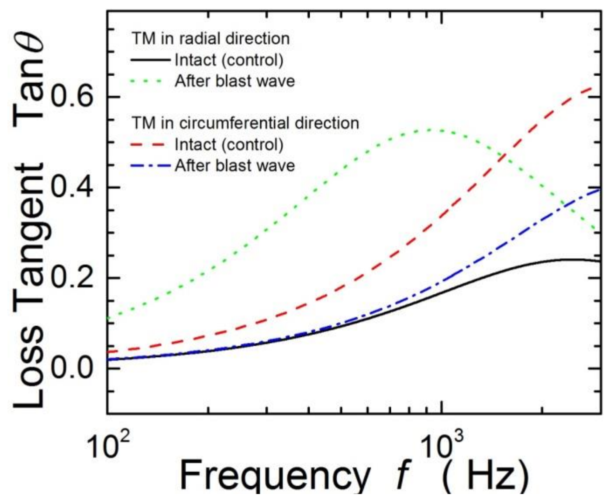

(c)

Figure 9. Comparison of Complex modulus between control and blasted TMs in frequency domain. (a). Storage modulus; (b). Loss modulus; (c). Loss tangent.

C5 Conclusion

A blast chamber was used to shock control TM broken under 5 psi pressure. A miniature SHTB was used to measure Young's modulus of both control (intact) TM and the TM after exposure to blast wave. Young's modulus values of normal TM are 45.2~58.9 MPa and 34.1~56.8 MPa in the radial and circumferential direction (300~2000 s^{-1}), respectively. TMs after exposure to blast wave have higher Young's modulus in radial direction (24.3~96 MPa) and lower modulus in circumferential direction (11.7~78.3 MPa) than the corresponding values of normal TMs, respectively. A standard linear solid viscoelastic model was used to convert Young's modulus in time domain into frequency domain. Blast wave is shown to induce significant mechanical property changes, mainly due to damage.

Pressure Distribution in a Simplified Human Ear Model for High Intensity Sound Transmission

Takumi Hawa[1]
School of Aerospace
and Mechanical Engineering,
The University of Oklahoma,
865 Asp Avenue,
Felgar Hall Room 218,
Norman, OK 73019
e-mail: hawa@ou.edu

Rong Z. Gan
School of Aerospace
and Mechanical Engineering
and OU Bioengineering Center,
The University of Oklahoma,
865 Asp Avenue,
Felgar Hall Room 218,
Norman, OK 73019
e-mail: rgan@ou.edu

High intensity noise/impulse transmission through a bench model consisting of the simplified ear canal, eardrum, and middle ear cavity was investigated using the CFX/ANSYS *software package with fluid-structure interactions. The nondimensional fluid-structure interaction parameter q and the dimensionless impulse were used to describe the interactions between the high intensity pressure impulse and eardrum or tympanic membrane (TM). We found that the pressure impulse was transmitted through the straight ear canal to the TM, and the reflected overpressure at the TM became slightly higher than double the incident pressure due to the dynamic pressure (shocks) effect. Deformation of the TM transmits the incident pressure impulse to the middle ear cavity. The pressure peak in the middle ear cavity is lower than the incident pressure. This pressure reduction through the TM was also observed in our experiments that have dimensions similar to the simulation bench model. We also found that the increase of the pressure ratio as a function of the incident pressure is slightly larger than the linear growth rate. The growth rate of the pressure ratio in this preliminary study suggests that the pressure increase in the middle ear cavity may become sufficiently high to induce auditory damage and injury depending on the intensity of the incident sound noise.* [DOI: 10.1115/1.4027141]

Introduction

The significant recent increase in terrorist activity and military involvement has resulted in a greater risk to human health from explosions and blast waves. Despite its protective technology, the military has experienced the development of traumatic brain injury (TBI), auditory damages, and the loss of lives due to insufficient blast protection capabilities. For example, TBI has been observed in Iraq and Afghanistan and is a primary injury that impairs brain function and structures temporarily or permanently due to the significant levels of external forces, such as pressure, volumetric tension, and shear stress [1]. TBI cannot be treated by conventional medical technologies. In order to improve personal protection devices against TBI, blast injury mechanics has been an active research topic. Examples of this research include the development of finite element (FE) models for the mechanical response of the head and brain to blast loading [2,3].

Another example is auditory damages to the military service personnel who are exposed to high intensity sound produced by explosions and jet engines. Hearing loss becomes the most common disability in veterans. Auditory damage and injury cause eardrum or tympanic membrane rupture, which requires greater pressure differentials due to high magnitude blast than damage to the inner ear [4]. Therefore, understanding high intensity pressure wave transduction through the ear and proposing advanced hearing protection mechanisms is one of the major challenges in auditory sciences and rehabilitation engineering.

The normal hearing level of a human being is below 130 dB sound pressure level, which results in linear acoustic transmission of sound pressure into the inner ear or cochlea. To understand the mechanisms of auditory function in relation to ear structure changes, creating a physical model of the cochlea has been extensively challenged by many researchers due to the complexity of the geometry and material properties [5–7]. A simplified mathematical model of a guinea pig cochlea, which consisted of a coiled geometry as a straight channel, showed that there is no significant difference in the calculations due to the geometric complexity [8,9]. Recently, various FE models of the human ear have been developed [10–13]. In all published FE models, the ear components are assumed as a linear system with small vibrations for acoustic-mechanical transmission from the TM to the middle and finally to the cochlea. The dominant process used in FE modeling has been harmonic analysis with the acoustic-structure-fluid coupling [12–15].

However, the high intensity noise transmission in the human ear with fluid-structure interaction for modeling elastic TM has not been studied based on the authors' knowledge. In spite of the significant governmental and military resources directed towards reducing the risk to human health from blast waves, it is widely accepted that the effects of blast waves on the human ear canal and middle ear are poorly understood. Therefore, investigation of high intensity sound transduction through the ear is one of the most important research areas in rehabilitation engineering.

The work reported in this paper is focused on understanding the high intensity impulse transmission mechanism from the ear canal to the middle ear cavity. We employ a commercial numerical simulation package, CFX/ANSYS, with fluid-structure interactions to model benchmark geometry of the ear canal, TM, and cavity structure and to simulate the pressure wave propagation through the ear. As a preliminary study to have a basic idea of how high intensity noise transmits through the bench model, the TM is assumed as a linear elastic material. The dimensionless impulse and the nondimensional parameter q derived by Taylor [16] are used to describe the fluid-structure interaction. The relationship between the pressure ratio (the incident pressure to the pressure in the middle ear cavity) and the material properties of the membrane associated with the duration time of the overpressure wave is clarified. The results provide insight into the relationship between q and the pressure ratio. Also, we compare the simulation results with the blast experiments and identify the mechanism of the pressure wave transmission through the TM to the cavity.

[1]Corresponding author.

Contributed by the Fluids Engineering Division of ASME for publication in the JOURNAL OF FLUIDS ENGINEERING. Manuscript received July 30, 2013; final manuscript received February 27, 2014; published online September 4, 2014. Assoc. Editor: John Abraham.

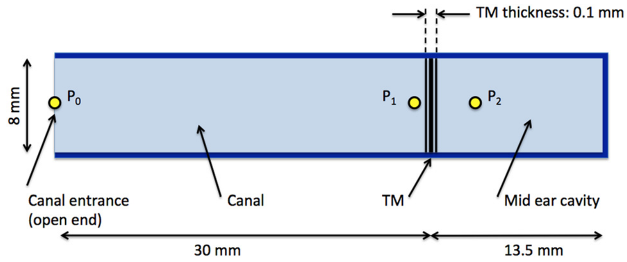

Fig. 1 Geometry of the model

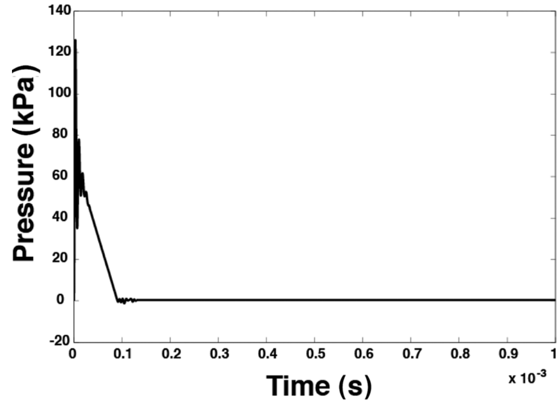

Fig. 2 A typical example of variation of the blast overpressure with time at the entrance of the ear canal model

Benchmark Model for the Ear and Simulation Conditions

A benchmark model for the ear consisting of simplified ear canal, TM, and middle ear cavity is presented in Fig. 1. The pipe is divided into two sections by an elastic thin plate, which models the TM. The ear canal and the cavity are sectioned between the open-end and TM, and between the TM and close-end, respectively. The lengths of the ear canal and cavity are 30 mm and 13.5 mm, respectively, based on published ear anatomic structure [11,17]. The thickness of the TM is 0.1 mm, and the diameter of the pipe is 8 mm according to the geometry of the human TM and ear canal [18].

For a simulation of continuous fluid domain, the continuity, momentums, and energy equations from physical principles of classical fluid mechanics have been used to predict the high intensity overpressure propagation in the domain. These equations are given by [19]

$$\frac{\partial \rho_f}{\partial t} + \nabla \cdot (\rho_f v) = 0$$

$$\frac{\partial \rho_f \boldsymbol{V}}{\partial t} + \nabla \cdot (\rho_f \boldsymbol{V}\boldsymbol{V}) = -\nabla p + \nabla \cdot \tau_f$$

$$\frac{\partial(\rho_f h_{\text{tot}})}{\partial t} - \frac{\partial p}{\partial t} + \nabla \cdot (\rho_f \boldsymbol{V} h_{\text{tot}}) = \nabla \cdot (\lambda \nabla T) + \nabla \cdot (\boldsymbol{V} \cdot \tau_f)$$

where t is the time, ρ_f is the fluid density, τ is the stress tensor of the fluid, $\boldsymbol{V}$ is the velocity vector, p is the pressure, T is the temperature, and λ is the thermal conductivity of the fluid. The stress tensor can be defined as

$$\tau_f = \mu\left(\nabla \boldsymbol{V} + (\nabla \boldsymbol{V})^T - \frac{2}{3}\delta \nabla \cdot \boldsymbol{V}\right)$$

where δ is the Kronecker δ, and μ is the viscosity of the fluid. The total enthalpy h_{tot} can be defined as

$$h_{\text{tot}} = h_{st} + V^2/2$$

where h_{st} is the static enthalpy. An arbitrary Lagrangian–Eulerian formulation is used to solve the above equations, allowing the deformation of the fluid domain to be found.

The governing equation for the solid domain can be described by using the second law of motion

$$\rho_s \ddot{\boldsymbol{d}}_s = \nabla \cdot (\boldsymbol{F} \cdot \boldsymbol{S}(\boldsymbol{d}_s)) + \boldsymbol{f}_s$$

where ρ_s is the solid density, $\boldsymbol{d}_s$ is the displacement vector of the structure, $\boldsymbol{f}_s$ is the externally applied body force vector on the structure, $\boldsymbol{S}$ represents the second Piola–Kirchhoff stress tensor, and $\boldsymbol{F}$ represents the deformation gradient tensor. On the fluid-structure interfaces along TM boundaries, the particle velocity is coupled to the flexible TM structure, such that both the displacement compatibility and the traction equilibrium are satisfied. Thus, the fluid and the structure do not overlap or detach during the motion, and no particle can cross the interface due to the kinematic requirement. The computations of fluid-structure interaction problems coupling computational fluid dynamics analysis with finite element stress analysis are performed using a commercial package, CFX with ANSYS. CFX solves the Navier–Stokes equations for the fluid flow using a finite element control volume formulation to construct the discrete equations. ANSYS is a finite element software package for linear and nonlinear stress analysis that will be used to compute the deformation of the elastic TM due to the overpressure loading. Details of the simulation package can be found in their manual [20].

The boundary conditions along the surfaces are the tangency and no-slip conditions. We consider a high-pressure wave traveling in the positive x direction through the ear canal section towards a thin elastic plate (TM). A typical example of a high-pressure incident wave pulse at the entrance of the ear canal due to the high intensity impulse/blast is presented in Fig. 2. For this particular example, we command that the input pressure is suddenly increased to 70 kPa at $t = 0^+$ and linearly decays with $t_0 = 90\mu$s, where t_0 is the duration time of the input blast overpressure. However, a large initial pressure fluctuation is observed in the figure due to the quick response to the input pressure peak in the CFX control function. Because of the quickly transient response in pressure, the high rate of increase of pressure could cause the pressure to overshoot the target pressure value and be forced by the CFX function to return the target value.

Explosions and Blast Waves

During the explosion, the release of a large amount of energy occurs in a very short period of time on the order of 10^{-6} to 10^{-3} s. Such a fast energy release induces an instantaneous increase in the pressure and temperature (approximately, 100 MPa and 3000 K, respectively) within the explosive materials. The extremely high pressure due to the explosion generates a strong blast wave propagating in the surrounding medium away from the explosion point.

In 1963, Taylor considered a blast wave as a one-dimensional exponentially decaying pressure wave pulse and investigated the interactions between blast waves and plates [16]. The momentum available in the incident pulse is given by $I_0 = \int_0^{t_0} p dt = p_0 t_0$, where p_0 is the incident pressure peak. When this incident pulse impinges on the thin plate, it induces the motion of the plate and is partly reflected. Taylor obtained a relation

$$I/I_0 = 2q^{q/(1-q)} \quad (1)$$

where I is the transmitted impulse and the q is the nondimensional parameter describing the fluid-structure interaction. This nondimensional parameter

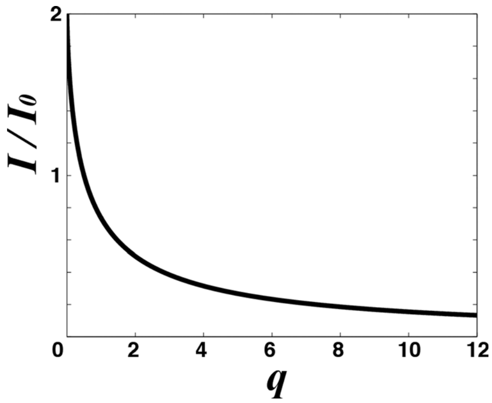

Fig. 3 Taylor's plot (momentum ratio, I/I_0 versus q) for considering fluid-structure interaction

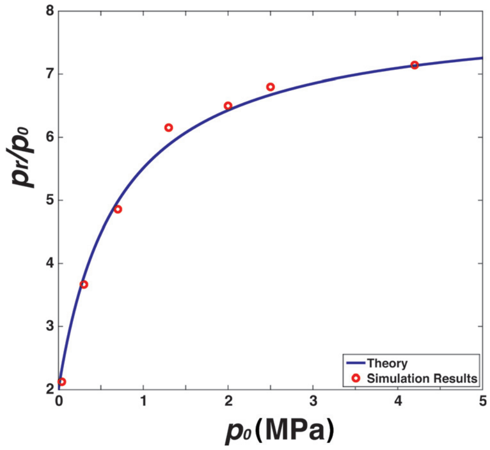

Fig. 4 Reflected pressure wave magnitudes against a solid wall with various inlet or incident pressures

$$q = t_0/t^* \tag{2}$$

compares the characteristic time of the fluid-structure interaction t^* and the incident wave duration time t_0. t^* is given by

$$t^* = \rho_s h/\rho_f c_f \tag{3}$$

where ρ_s, ρ_f, c_f, and h are the density of the TM (1200 kg/m^3) [21], density of the air (1.2 kg/m^3), sound speed of the air (343 m/s), and thickness of the TM (0.1 mm) [22], respectively. The momentum ratio of the transmitted impulse I/I_0 defined in Eq. (1) is a monotonically decreasing function of q, depending on the plate density. The above three equations (Eqs. (1)–(3)) imply that less impulse is transmitted to lighter plates because the lower plate density induces the higher value of q. For example, when the TM is relatively massive, it is hardly moving and the impulse of the pressure wave is reflected with nearly perfect. Thus, the reflected momentum is about $-I_0$, and the TM gains momentum nearly $2I_0$. The momentum ratio asymptotes to a constant value of 2 for small q and $2/q$ for large q (see Fig. 3). Based on the properties suggested by the literature, it is computed that the characteristic time of the fluid-structure interaction is 2.9×10^{-4} s, and our experiments suggest that t_0 is 3 ms (details of the discussions will appear in the Model Validation section). Thus, the time scale ratio q is approximately 10.3. However, since the round trip distance for the pressure pulse between the ear canal entrance and TM is 60 mm, it only takes 1.75×10^{-4} s, which is 1 order magnitude less than our experimental duration time t_0. When the reflected pressure wave comes back to the entrance of the ear canal, the numerical noise generated by the outer flow boundary condition propagates back to the TM and pollutes the simulation results. Thus, we run various cases of simulations for $t_0 < 3$ ms with smaller ρ_s such that the time scale ratio q can maintain its original value 10.3.

The simulation results also depend on the Young's modulus of the TM E_Y. The E_Y of the TM is 2×10^7 N/m^2 [23]. The dimensionless impulse in terms of the Young's modulus can be described as $I/\left(M\sqrt{E_Y/\rho_s}\right)$, where M is the mass per unit area of the TM. For example, when $q = 10.3$, $p_0 = 100$ kPa, $t_0 = 3$ ms, $\rho_s = 1200$ kg/m^3, $E_Y = 2 \times 10^7$ N/m^2, and the mass per unit area of the TM, $\rho_s \cdot h = 0.12$ kg/m^2, the dimensionless impulse is approximately 2.9. In order to maintain the values of the time scale ratio q and the dimensionless impulse for different values of p_0 and t_0, we must choose appropriate values of ρ_s and E_Y for each simulation case.

Model Validation

Sensitivity of Simulation. Before moving on to the fluid-structure interaction (FSI) problem, we have performed a benchmark test against known theoretical results for a wave propagation problem [24]. According to the theory of the blast wave striking a solid massive wall, the value of reflective pressure approaches eight times as high as the incident pressure for very large values of the incident pressure and dynamic pressure under strong shocks [24]. On the other hand, when the incident pressure is negligible compared with the atmospheric pressure, the value of the reflective pressure tends toward twice the incident pressure. The reflected pressure p_r for air is given by

$$p_r = 2p_0 \frac{7p_{\text{atm}} + 4p_0}{7p_{\text{atm}} + p_0}$$

where p_{atm} is the atmospheric pressure. In order to perform this benchmark test problem for the model validation, we have considered our computational domain shown in Fig. 1 with 69,216 nodes; however, the TM has been considered as a solid wall to simulate the benchmark test problem. This implies that the middle ear cavity domain does not contribute to the simulation results in this test. We have used the high-resolution scheme in the CFX options to compute the advection terms in discrete finite volume equations and the second-order backward Euler discretization scheme for transient calculation. The air density = 1.2 kg/m^3 and time step = 10 ns are used to ensure the stability of the scheme. Based on the average spatial step size = 0.3 mm and the speed of sound in the air at the room temperature = 343 m/s, the corresponding Courant-Friedrichs-Lewy number is approximated as 0.01. As for convergence criterion, we have chosen a root mean square option and 0.0001 for residual type and target value, respectively. Simulation results with various inlet pressure p_0 values (0.04, 0.3, 0.7, 1.3, 2, 2.5, and 4.2 MPa) are considered and compared with the theoretical prediction in Fig. 4. The simulation results show excellent agreement with the theoretical prediction, which implies that our model is suitable for the wave propagation analysis.

The sensitivity of the simulations to mesh refinement is investigated. The investigation focuses on $p_0 = 100$ kPa with time duration $t_0 = 10\,\mu$s, TM density $\rho_s = 4$ kg/m^3, and TM Young's modulus $E_Y = 2 \times 10^7$ N/m^2 to maintain values of q and dimensionless impulse parameter. Since the bending stiffness and nonlinear properties of the TM in response to high intensity impulse are currently not available in the literature to our knowledge, we have considered the TM as a linear isotropic elastic material for simplicity. The time step = 10 ns was chosen for all simulation studies to ensure the numerical stability for large mesh displacement.

For the model's grid refinement validation, the pressure ratio p_0/p_2 is measured with various fluid mesh sizes (5472, 13,152,

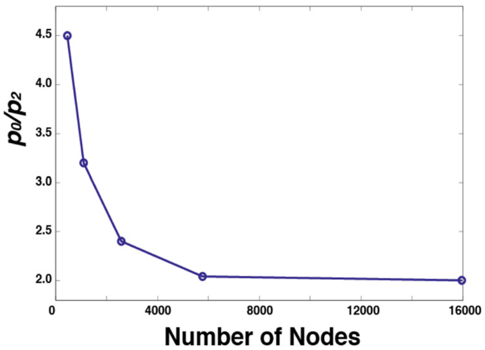

Fig. 5 Pressure ratio dependence of the number of nodes in the flow field

30,912, 69,216, and 191,472 nodes) while fixing the eight-node TM element with 12,792 nodes. Figure 5 summarizes the results obtained with various pressure ratios from simulations. It demonstrates the convergence of the computed pressure ratio results with mesh refinement. It is found that the meshes with 69,216 nodes provide a difference in computations of the pressure ratio within 1%. Moreover, the simulation time for 191,472 nodes requires more than four times longer than that for the mesh with 69,216 nodes. It should be pointed out that such a small variation in the pressure ratio might be due to the presence of a large pressure gradient at the blast wave front. This overpressure wave structural difference diminishes as the number of nodes increases with a refinement of the mesh. We have also studied mesh sensitivity of the solid (TM) domain on the simulation with the eight-node element with reduced order integration method and nonlinear option in ANSYS that are capable to consider geometric nonlinearity and to alleviate locking behavior. The deflection of the TM in the axial direction is measured with various mesh sizes (5184, 12,792, and 26,376 nodes). Figure 6 shows the meshes with 12,792 nodes provide a difference in computations of the TM deflection within 0.2%. Thus, in order to obtain sufficient accuracy for computations within reasonable simulation time, we chose to use 69,216 and 12,792 nodes in the fluid and structure domains for the simulations, respectively.

Experimental Measurement on Bench Model. To validate the FE model for simulating high intensity sound transduction through the ear and to have a better understanding of the overpressure distribution from the ear canal to the middle ear, a simple bench (physical) model with dimensions similar to the FE model of Fig. 1 was created. The bench model was made from hard plastics (i.e., polymethacrylate) with the design of the ear canal and middle ear cavity chambers as shown in Fig. 7(*a*). These two chambers were separated by a membrane of thin latex material (Saf-Care^{TM}) to simulate the TM. The diameter, length, and volume of the ear canal and middle ear cavity components were similar to that of a human ear [12,25,26]. Data of the Young's modulus and density of the latex material are not available; however, an analysis of a few other kinds of gloves estimated E_Y ranging from 0.3 to 3 MPa in the literature [27], which agreed with values obtained from our experimental measurements. Two pressure sensors (Models 102B16 and 105C02, PCB Piezotronics, NY) were inserted in the bench model at the entrance of the canal chamber and inside of the cavity chamber to measure p_0 and p_2, respectively. As shown in Fig. 7(*b*), the bench model with the inserted pressure sensors was placed in a specially designed holder and exposed to blast overpressure in the high intensity sound chamber in Gan's biomedical engineering lab at the University of Oklahoma. The compressed air (nitrogen)-driven blast apparatus is capable of generating an overpressure or impulse of at least 30 psi or 207 kPa inside an anechoic chamber.

Five exposure tests were performed on the bench model, and Fig. 8 illustrates the recorded pressure waveforms of p_0 and p_2.

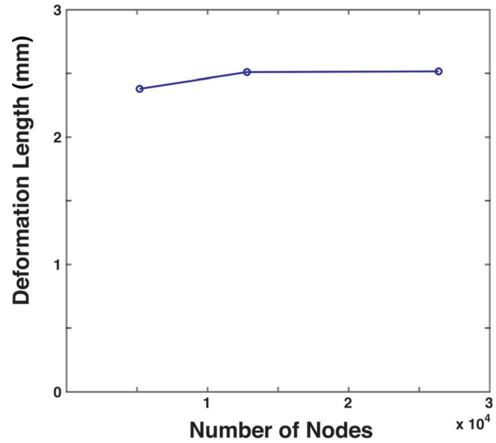

Fig. 6 TM deflection dependence of the number of nodes of the TM structure

Figure 8(*a*) shows the typical overpressure waveform of p_0 measured at the ear canal entrance within the time duration of 3 ms to reach the peak pressure. The waveform of p_2 displayed in Fig. 8(*b*) demonstrates that the impulse pressure transmitted into the middle ear cavity became somewhat similar to an acoustic waveform. The mean peak pressure of p_0 from five tests was 5.29 psi (36.5 kPa) with standard deviation ± 0.71 psi or ± 4.93 kPa. The mean peak-to-peak pressure of p_2 was 1.91 ± 0.47 psi (or 13.17 ± 3.28 kPa). The ratio of p_0 to p_2 ranged from 2.55 to 3.46 with an average of 2.77 ± 0.43. The statistical results for p_0 and p_2 (student t-test, p-value < 0.01 with 95% confidence interval) indicates that the peak pressure measured at the ear canal entrance (p_0) was significantly different from the pressure inside the middle ear cavity (p_2). These pressure results obtained from the bench model tests will be compared with simulation results in the Simulation Results and Discussions section.

Simulation Results and Discussions

Several high intensity noise loadings (between 17 and 135 kPa) induced deformation of the TM, and the changes of the pressure inside the middle ear cavity have been derived with various TM densities (between 1.2 and 36 kg/m^3) and TM Young's moduli (between 2×10^4 and 6×10^5 N/m^2). A typical example of time-history plots of the pressure propagation is shown in Fig. 8. This example is simulated with $p_0 = 49$ kPa, $E_Y = 6 \times 10^5$ N/m^2, and $\rho_s = 36$ kg/m^3. Note that the initial location of the TM is at $x = 30$ mm, and the input target pressure at the inlet of the ear canal is presented in Fig. 2. The peak target pressure was 70 kPa; however, a large initial pressure fluctuation is presented in that figure. The input pressure is damped, and the peak pressure decays to 49 kPa (see Fig. 9). The pressure wave is stabilized at $t = 0.04$ ms and propagates toward the TM with $t_0 = 90\,\mu$s (see Fig. 2). The slight sharp increase of the pressure observed at the location $x = 30$ mm at $t = 0.08$ ms in Fig. 8 indicates the initial contact with the TM. This pressure wave moves the TM front as we see the movement of the sharp increase of the pressure to the middle ear cavity side at $t = 0.10$ ms. At $t = 0.12$ ms, a large pressure discontinuity is observed at the location $x = 32.5$ mm. This indicates that the maximum deformation of the TM is reached at this time. The maximum deformation and the associated pressure are approximately 2.5 mm and 111 kPa, respectively.

At $p_{atm} = 101$ kPa and $p_0 = 49$ kPa, p_r is approximately 117 kPa. However, the maximum pressure obtained from the simulations is $p_r = 111$ kPa, which is slightly less than the predicted value because there is an energy loss at the TM due to its lighter density and elasticity. Also, the pressure value near the TM is slightly higher than twice the incident pressure p_0. The increase of the reflected pressure above the expected value of twice the incident

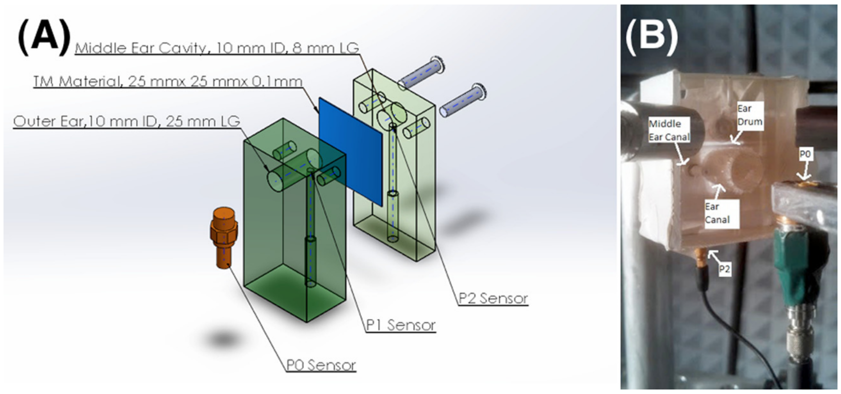

Fig. 7 (*a*) Illustration of the design of the bench model and (*b*) picture of the bench model with inserted pressure sensors placed inside of the blast or high intensity sound test chamber

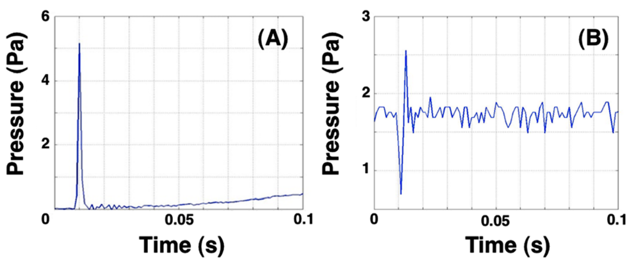

Fig. 8 (*a*) Typical waveform of p_0 (pressure amplitude-time curve) measured in bench model and (*b*) waveform of p_2 measured in bench model

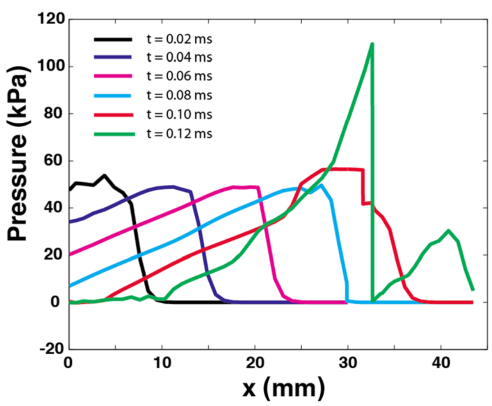

Fig. 9 A simulation of pressure propagation through the ear canal, TM, and cavity at six different times, $t = 0.02$, 0.04, 0.06, 0.08, 0.10, and 0.12 ms when $t_0 = 90\,\mu s$, $\rho_s = 36\,kg/m^3$, and $E_Y = 6 \times 10^5\,N/m^2$

value is due to the dynamic (or shock) pressure. In addition, the deformation of the TM generates another wave propagating downstream inside of the middle ear cavity. The amplitude of the pressure in the cavity (p_2) is approximately 30.5 kPa, which provides the pressure ratio p_0/p_2 approximately 1.63. Due to the presence of the TM, the pressure reduction in the middle ear cavity was observed; however, since the TM is elastic, the pressure reduction is not significantly high but dependent on the intensity of the noise. The pressure increase in the middle ear cavity could be sufficiently high to induce auditory damage and injury. After reaching the maximum deformation of the TM, the incident pressure wave is reflected in the ear canal, and the pressure peak quickly decays to slightly less than the original incident pressure value due to the loss of the energy at the TM.

Table 1 Pressure ratio p_0/p_2 from simulations

t_0 (μs)	ρ_s (kg/m^3)	E_Y (N/m^2)	p_0 (kPa)	p_1 (kPa)	p_2 (kPa)	p_0/p_2
3	1.2	2×10^4	107	142	51	2.098
5	2	3.3×10^4	98	133	50	1.960
10	4	6.7×10^5	102	140	50	2.040
30	12	2×10^5	105	165	51	2.059
60	24	4×10^5	100	170	50	2.000

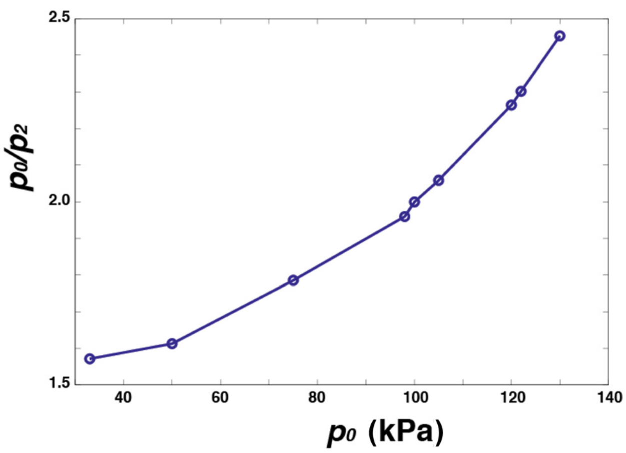

Fig. 10 Pressure ratio p_0/p_2 dependence of input pressure p_0

A summary of the pressure ratios for various duration (t_0), E_Y, and ρ_s values is presented in Table 1. Note that the values of t_0, E_Y, and ρ_s are chosen to maintain the time scale ratio q and the dimensionless impulse. q is set to be 10.3 as described in previous section, which is the value calculated based on t_0 obtained from the experiments and ρ_s of the human TM. It can be seen from the table that in the simulations with the incident pressure value p_0 being approximately the same, the pressure ratio does not change as long as the q value and the dimensionless impulse are maintained at the same values.

The dependence of pressure ratio p_0/p_2 on the incident peak pressure p_0 is shown in Fig. 10. The pressure ratio increases as the incident peak pressure increases with a slightly larger growth rate than the linear growth. This indicates that the p_2 does not increase as much as the p_0 increase. Although the growth rate of the pressure ratio is not significant, the pressure increase in the middle ear cavity could be sufficiently high to induce auditory damage and injury depending on the intensity of the incident pressure noise. Note that the pressure ratio at $p_0 = 36.5$ kPa is approximately 1.6

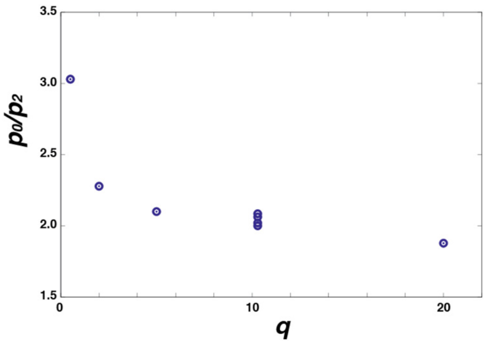

Fig. 11 Pressure ratio p_0/p_2 dependence on q

according to the figure, which indicates the pressure reduction through the TM. This pressure reduction has been seen in our experiments. The pressure ratio of the experimental data ranges from 2.55 to 3.46, which are higher than the simulation results. The difference between the simulation and experimental results is probably caused by neglecting the nonlinearity of the material properties of the TM. Moreover, the pressure ratio might depend on the material properties of the TM, and the use of the latex material may cause the difference in simulation and experimental values of the pressure ratio.

Figure 11 shows the dependence of pressure ratio p_0/p_2 on the time scale ratio q computed by simulations. It can be seen that the pressure ratio increases with a decrease in q exponentially. The trend of the curve is similar to the relationship between the momentum ratio and q (Fig. 3). When the TM is relatively massive, it hardly moves and the amplitude of the pressure wave generated in the cavity becomes smaller. Thus, the pressure ratio becomes larger. On the other hand, when the TM is relatively light, it moves easily and the amplitude of the pressure wave generated in the cavity becomes larger. Thus, the pressure ratio becomes smaller as the q decreases. These simulation results clarify the physical mechanisms of the pressure generation in the cavity.

Conclusion

We have investigated high intensity noise/impulse transmission through a bench model consisting of a simplified ear canal, TM, and middle ear cavity using the CFX/ANSYS software package with fluid-structure interactions. The nondimensional fluid-structure interaction parameter q and the dimensionless impulse are applied to describe the interactions between high intensity pressure impulse and TM. The simulations demonstrate that the pressure impulse is transmitted through the ear canal to the TM, and the reflected overpressure becomes slightly higher than twice the incident pressure. The incident pressure impulse has high enough intensity, which induces the dynamic pressure (shocks) effect. The reflected overpressure deforms the TM, and the deformation transmits the incident pressure impulse into the middle ear cavity. The incident pressure peak is much higher than that of the pressure in the middle ear cavity.

To validate the simulation results, we have conducted experiments on a physical bench model, which has dimensions similar to the simulation bench model. The experimental results show a good agreement with the simulations. It is also found that the increase of the pressure ratio as a function of the incident pressure is slightly larger than the linear growth rate. The growth rate of the pressure ratio in this preliminary study suggests that the pressure increase in the middle ear cavity may become sufficiently high to induce auditory damage and injury if the intensity of the incident sound noise reaches really high levels.

The model and simulation reported in this paper is our first step to investigate the overpressure distribution from the ear canal to the middle ear cavity. In order to understand the details of the high intensity noise transmission through the ear, it is important to consider the nonlinear mechanical properties of ear tissues and the actual geometry of the ear components in the future simulation models.

Acknowledgment

We thank Don Nakmali, M.S. and Zach Yokell, B.S. from the biomedical engineering lab at the University of Oklahoma Bioengineering Center for their expert technical assistance on the bench model test.

Nomenclature

c = sound speed
$\boldsymbol{d}$ = displacement
E_Y = Young's modulus
$\boldsymbol{f}$ = externally applied body force vector
h = static enthalpy
h_{tot} = total enthalpy
I = transmitted impulse
I_0 = momentum available in the incident pulse
M = mass per unit area of the TM
$\mathbf{n}$ = unit normal vector
p = pressure
$p_{\rm atm}$ = atmospheric pressure
p_r = reflected pressure
p_0 = incident pressure peak
P_0 = pressure at inlet
P_1 = pressure at TM
P_2 = pressure in the mid ear cavity
q = nondimensional fluid-structure interaction parameter
t = time
T = temperature
t_0 = duration time of the input blast overpressure
t^* = characteristic time of the fluid-structure interaction
V = velocity magnitude
$\boldsymbol{V}$ = velocity vector
x = Cartesian coordinates in x-direction
δ = Kronecker δ
λ = thermal conductivity
μ = viscosity
ρ = density
$\boldsymbol{\sigma}$ = Cauchy stress tensor
τ = stress tensor

Subscripts

f = fluid
s = solid

References

[1] Taylor, P. A., and Ford, C. C., 2009, "Simulation of Blast-Induced Early-Time Intracranial Wave Physics Leading to Traumatic Brain Injury," ASME J. Biomech. Eng., **131**(6), p. 061007.
[2] Bass, C. R., Panzer, M. B., Rafaels, K. A., Wood, G., Shridharani, J., and Capehart, B., 2012, "Brain Injuries From Blast," Ann. Biomed. Eng., **40**(1), pp. 185–202.
[3] Panzer, M. B., Myers, B. S., Capehart, B. P., and Bass, C. R., 2012, "Development of a Finite Element Model for Blast Brain Injury and the Effects of CSF Cavitation," Ann. Biomed. Eng., **40**(7), pp. 1530–1544.
[4] Mrena, R., Paakkonen, R., Back, L., Pirvola, U., and Ylikoski, J., 2004, "Otologic Consequences of Blast Exposure: A Finnish Case Study of a Shopping Mall Bomb Explosion," Acta Otolaryngol., **124**(8), pp. 946–952.
[5] Steele, C. R., and Taber, L. A., 1979, "Comparison of WKB Calculations and Experimental Results for 3-Dimensional Cochlear Models," J. Acoust. Soc. Am., **65**(4), pp. 1007–1018.
[6] Cancelli, C., Dangelo, S., Masili, M., and Malvano, R., 1985, "Experimental Results in a Physical Model of the Cochlea," J. Fluid Mech., **153**, pp. 361–388.
[7] Lechner, T. P., 1993, "A Hydromechanical Model of the Cochlea With Nonlinear Feedback Using PVF(2) Bending Transducers," Hear. Res., **66**(2), pp. 202–212.

[8] Steele, C. R., and Zais, J. G., 1985, "Effect of Coiling in a Cochlear Model," J. Acoust. Soc. Am., **77**(5), pp. 1849–1852.
[9] Loh, C. H., 1983, "Multiple Scale Analysis of the Spirally Coiled Cochlea," J. Acoust. Soc. Am., **74**, pp. 94–103.
[10] Koike, T., Wada, H., and Kobayashi, T., 2002, "Modeling of the Human Middle Ear Using the Finite-Element Method," J. Acoust. Soc. Am., **111**(3), pp. 1306–1317.
[11] Sun, Q., Gan, R. Z., Chang, K. H., and Dormer, K. J., 2002, "Computer-Integrated Finite Element Modeling of Human Middle Ear," Biomech. Model. Mechanobiol., **1**(2), pp. 109–122.
[12] Gan, R. Z., Feng, B., and Sun, Q., 2004, "Three-Dimensional Finite Element Modeling of Human Ear for Sound Transmission," Ann. Biomed. Eng., **32**(6), pp. 847–859.
[13] Zhang, X. M., and Gan, R. Z., 2011, "A Comprehensive Model of Human Ear for Analysis of Implantable Hearing Devices," IEEE Trans. Biomed. Eng., **58**(10), pp. 3024–3027.
[14] Gan, R. Z., Reeves, B. P., and Wang, X. L., 2007, "Modeling of Sound Transmission From Ear Canal to Cochlea," Ann. Biomed. Eng., **35**(12), pp. 2180–2195.
[15] Gan, R. Z., Cheng, T., Dai, C. K., Yang, F., and Wood, M. W., 2009, "Finite Element Modeling of Sound Transmission With Perforations of Tympanic Membrane," J. Acoust. Soc. Am., **126**(1), pp. 243–253.
[16] Taylor, G. I., 1963, *The Pressure and Impulse of Submarine Explosion Waves on Plates*, Cambridge University, Cambridge, UK.
[17] Gan, R. Z., and Wang, X. L., 2007, "Multifield Coupled Finite Element Analysis for Sound Transmission in Otitis Media With Effusion," J. Acoust. Soc. Am., **122**(6), pp. 3527–3538.
[18] Wever, E. G., and Lawrence, M., 1982, *Physiological Acoustics*, Princeton University, Princeton, NJ.
[19] Batchelor, G. K., 1967, *An Introduction to Fluid Dynamics*, Cambridge University Press, Cambridge, UK.
[20] ANSYS, 2010, "ANSYS CFX-PRE User's Guide," Canonsburg, PA.
[21] Wada, H., Metoki, T., and Kobayashi, T., 1992, "Analysis of Dynamic Behavior of Human Middle-Ear Using a Finite-Element Method," J. Acoust. Soc. Am., **92**(6), pp. 3157–3168.
[22] Kirikae, I., 1960, *The Structure and Function of the Middle Ear*, University of Tokyo, Tokyo, Japan.
[23] Von Bekesy, G., 1960, *Experiments in Hearing*, McGraw-Hill, New York.
[24] Mays, G. C., and Smith, P. D., 1995, *Blast Effects on Buildings*, Thomas Telford Publications, London.
[25] Cheng, T., Dai, C. K., and Gan, R. Z., 2007, "Viscoelastic Properties of Human Tympanic Membrane," Ann. Biomed. Eng., **35**(2), pp. 305–314.
[26] Luo, H. Y., Dai, C. K., Gan, R. Z., and Lu, H. B., 2009, "Measurement of Young's Modulus of Human Tympanic Membrane at High Strain Rates," ASME J. Biomech. Eng., **131**(6), p. 064501.
[27] Krutzer, B., Ros, M., Smit, J., and de Jong, W., 2011, "A Review of Synthetic Latices in Surgical Glove Use," http://www.kraton.com/products/cariflex/synthetic_latices.pdf